Martin Stermitz, BSc

Free Standing Quasi-1D Resonators for Sensing Applications

MASTER THESIS

For obtaining the academic degree
Diplom-Ingenieur

Master Programme of
Technical Physics

Graz University of Technology

Supervisor:
Ao.-Univ.-Prof. Dipl.-Ing. Dr. techn. Werner Grogger
Institute of Electron Microscopy and Nanoanalysis
Co-Supervisor:
Dipl.-Ing. Dr. techn. Harald Plank

Graz, March 2014

Abstract

This master thesis focuses on freestanding Pt-C nanopillars (quasi-1D) and nanopads (quasi-2D) prepared via focused electron beam induced deposition (FEBID). In more detail, the nanostructures were excited at their mechanical resonance frequencies via alternating electric fields in close proximity. The background idea was to develop the basis for a gas sensing concept in which the intrinsic resonance frequencies of the nanostructures are changed due to gas adsorption and the entailed mass change of the nanoresonator.

As starting point, the FEBID structures were exposed to constant electric fields leading to static and reversible morphological deflections. The results were used as input data for finite element simulations revealing good agreement with theoretical consideration of their scaling behavior. In a second step, the structures were exposed to alternating electric fields which led to mechanical excitation according to their intrinsic resonance frequencies. Complementary simulations allowed estimation of the overall Young's modulus for the investigated structures which again has been found in very good agreement with theoretical considerations. In a third step, the FEBID structures have been subjected to post-growth treatments via the electron beam which allow fine tuning to higher resonance frequencies by a factor larger than 3, while outer diameters and chemical composition did not change. To explain this behavior a closer look was given to the internal structure of the pillars consisting of a nanogranular metal-matrix system by small Pt grains (~ 2 nm) embedded in a carbon matrix. Direct comparisons between as-prepared and long time treated pillars revealed the same overall grain distributions which explain the constant diameters and stable chemical compositions. Together with previous findings of a slight Pt grain growth during electron beam post-growth treatments it became obvious that the mechanical properties are increasingly governed by neighboring Pt grains which increasingly get in physical contact. Beside the resonance frequency, the resonance curves did also improve their sharpness which is a key issue toward sensitive sensor applications.

In a final step, the entire concept has successfully been tested via external electronics clearly showing the resonance behavior without electron microscopy based observations. By that, it can be stated that this master thesis represents the basis for a new sensor concept based on the 3D structuring capabilities on the nanoscale and the unique internal metal-matrix structure of FEBID based deposits.

Kurzfassung

Die vorliegende Masterarbeit konzentriert sich auf freistehende Pt-C Nanostäbchen (quasi-1D) und Nanoplättchen (quasi-2D) welche mittels fokussierter Elektronenstrahlabscheidung (focused electron beam induced deposition – FEBID) hergestellt wurden. Im Detail wurden diese Nanostrukturen bei ihren mechanischen Resonanzfrequenzen mittels elektrischer Wechselfelder in unmittelbarer Nähe angeregt. Die Hintergrundidee war die Entwicklung eines Gas Sensor Konzepts, welche auf einer Änderung der intrinsischen Resonanzfrequenzen basiert, hervorgerufen durch die Adsorption von Gasmolekülen und der darauffolgenden Massenänderung der Nanoresonatoren.

Als Startpunkt wurden die FEBID Strukturen in konstante elektrische Felder gebracht was zu einer statischen und reversiblen morphologischen Auslenkung führte. Die Ergebnisse wurden als Inputparameter für Finite Elemente Simulationen herangezogen welche sehr gute Übereinstimmung mit theoretischen Betrachtungen hinsichtlich Skalierungsverhalten zeigten. In einem zweiten Schritt wurden die Strukturen in alternierende elektrische Felder gebracht was zu einer mechanischen Anregung gemäß den intrinsischen Resonanzfrequenzen führte. Komplementäre Simulationen ermöglichten die Abschätzung eines globalen Young's Moduls der untersuchten Strukturen, welcher wiederum eine sehr gute Übereinstimmung mit theoretischen Betrachtungen zeigte. In einem dritten Schritt wurden die FEBID Strukturen einem Nachbehandlungsschritt mittels Elektronenstrahlen unterzogen, was ein Verstimmen der Resonanzfrequenz hin zu höheren Werten (bis zu einem Faktor größer 3 der Ausgangsfrequenz) ermöglichte, während Außendurchmesser und chemische Zusammensetzung nicht variierten. Um diese Beobachtungen zu erklären wurden genauere Untersuchungen durchgeführt, welche sich auf die innere Struktur der Stäbchen bezog. Diese besteht aus einem Metall-Matrix System, in dem Pt Körner (~ 2nm) in einer Kohlenstoffmatrix eingebettet sind. Direkte Vergleiche zwischen unbestrahlten und langzeitbestrahlten Stäbchen zeigten, dass die Verteilung der Pt Körner konstant blieb, was gleichbleibenden Außendurchmesser und chemische Zusammensetzung erklären konnte. Zusammen mit vorhergehenden Ergebnissen - welche zeigten, dass die Pt Körner während der Elektronenstrahlnachbehandlung leicht wachsen - wurde ersichtlich, dass die mechanischen Eigenschaften zunehmend von benachbarten Pt Körnern bestimmt werden, welche sich stärker zu berühren beginnen. Neben der Resonanzfrequenz zeigten die Resonanzkurven eine schmälere Verteilung was ein Schlüsselelement hinsichtlich sensibler Sensorcharakteristik darstellt.

In einem letzten Schritt wurde das gesamte Konzept erfolgreich mittels externer Elektronik getestet, welche auch ohne elektronenmikroskopische Untersuchungen das Resonanzverhalten eindeutig nachweisen konnte. Damit lässt sich belegen, dass diese Master Thesis die Grundlage für ein neuartiges Sensorkonzept liefert, welches auf den 3D Strukturierungsmöglichkeiten im Nanometerbereich sowie auf der einzigartigen inneren Metall-Matrix Struktur von FEBID basierten Strukturen beruht.

Acknowledgements

First of all I would like to thank Professor Ferdinant Hofer who is the head of the institute for giving me the opportunity to write this thesis at this high sophisticated institute.

Also I want to thank Professor Werner Grogger for being my supervisor and for his cooperation.

Especially I want to thank my co-supervisor Harald Plank for his lasting support during the whole work and also for giving me the opportunity to bring in my own ideas and for his trust which makes the work to a joyful experience.

I want to thank the whole FELMI and ZFE team for giving me helpful support especially Martina Dienstleder for her good advices and her patience, Sebastian Rauch for the production of the test samples and Professor Gerald Kothleitner for the TEM investigations.

Furthermore I want to express my thanks to the S^3 workgroup for the great and friendly atmosphere, especially Robert Winkler and Roland Schmied for the cooperation and their support on the FIB and Angelina Orthacker for taking the time for additional TEM investigation despite the fact that she was very busy.

I also want to thank our partners at the NTC Weiz, Prof. E.J.W. List, DI S. Nau, Dr. S. Sax for the electrical readout measurements, Prof. Dr. Philip D. Rack, Dr. J.H. Noh (The University of Tennessee, Oak Ridge National Laboratories, USA) for providing the test electrode structures and Dr. Ivo Utke (EMPA, Thun, Switzerland) for the support.

Mostly I want to thank my parents who believed in me for my whole life and who supported me in all situations and thus made it possible for me to study at all.

Table of Contents

List of Abbreviations

BSE	…	*back scattered electrons*	PE	…	*primary electrons*
MTL	…	*mass transport limited*	PoP	…	*point pitch*
AFM	…	*atomic force microscope*	RRL	…	*reaction rate limited*
FWHM	…	*full width at half maximum*	RT	…	*refresh time*
FEBID	…	*focused electron beam induced deposition*	SDR	…	*Surface diffusion replenishment*
DBM	…	*dual beam microscope*	SE	…	*secondary electrons*
DT	…	*dwell time*	SEM	…	*scanning electron microscopy*
FIB	…	*focused ion beam*	TEM	…	*transmission electron microscopy*
ETD	…	*Everhardt Thornley detector*	TET	…	*total exposure time*
FEG	…	*field emission gun*	TLD	…	*through the lens detector*
GIS	…	*gas injection system*	UHV	…	*ultra high vacuum*
FSE	…	*forward scattered electrons*			

1 Introduction and Motivation

In the recent decades there exists a trend towards miniaturization, especially for electronic devices. The driving force is an increasing demand of computing power and performance, as well as a reduction of the energy consumption and a decrease of the mass. Therefore an ever-increasing integration depth is aimed. To make this possible new technologies have to be developed.

One of these technologies is the focused electron beam induced deposition (F**EBID**), which is a direct writing technique that makes it possible to "write" structures on a substrate's surface. Thereby gaseous precursor molecules are cracked by the electrons where the non-volatile parts are deposited on the surface near the point of interaction. Since this is a direct writing technique no expensive production of masks is needed. Another great advantage is that with FEBID even the deposition on not flat surfaces is possible. Furthermore it is not limited to the deposition of flat structures, also complex 3-dimensional structures can be produced which enables a large field of possibilities especially for sensing applications. There is already a number of precursors with different properties available (conducting, isolating, magnetic etc.) that can be chosen depending on the area of application.

Beneath the advantages the FEBID technique also has some disadvantages. The deposition process is quite slow yet and cannot compete with other industrial methods. Also the purity of the deposits is still very low due to problems of fully decomposing the precursor molecules during deposition which leads to unwanted side products in the pillars. At the FELMI currently attention is paid on post-growth purification of the deposits, on the investigation of new FEBID materials and also on the development of new sensing devices.

A number of FEBID based sensors has already been explored like bending sensors or hall sensors. In a previous work at our institute a flat gas sensing device was presented by Florian Kolb which makes use of the nano-granular metal matrix of the deposits.

The aim of this work is to build 3 dimensional Pt-C FEBID nano resonators. They can be excited via electrical fields which enables a further range of sensing applications. A method is presented which can be used to extract material parameters like the Young's modulus or the density of such three dimensional deposits, which are normally quite difficult to access by other methods. Also the nano-granular metal-matrix structure and there influence on the Young's modulus is observed. Furthermore a method is presented which enables the modification of the grain sizes and thus also of the intrinsic material parameters of the material which also can be used to trim the resonance frequency of our resonators in a wide range.

2 Materials

2.1 FEBID

Due to the development of new fabrication methods and industrial applications there exists an ongoing trend to manufacture smaller and smaller structures. One of the newer, non-planar technique which is increasingly used, is focused electron beam induced deposition (**FEBID**). FEBID is a direct writing technique for nanostructures via an electron beam in a scanning electron microscope (**SEM**). Flat and three dimensional structures can be produced on the nanoscale on almost each sample material without and pre- and / or post-processing steps. A typical FEBID setup is shown in Figure 2-1. A precursor gas which is supplied by a gas injection system is adsorbed on the substrate surface. At the same time an electron beam is systematically rastered over the samples surface following the intended shape of the final deposit. When it interacts with the precursor molecules they are dissociated into volatile parts which are pumped away by the vacuum system and into non-volatile parts which are locally immobilized and form the functional deposit depending on the precursor chemistry [1].

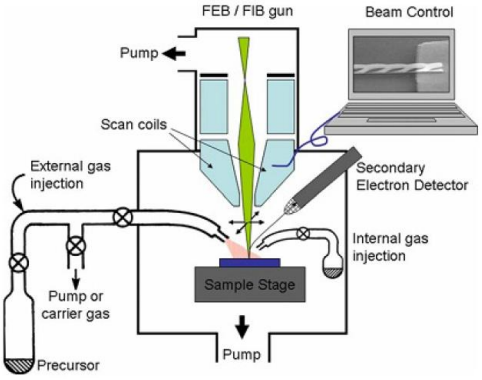

Figure 2-1: Technical FEBID setup [1].

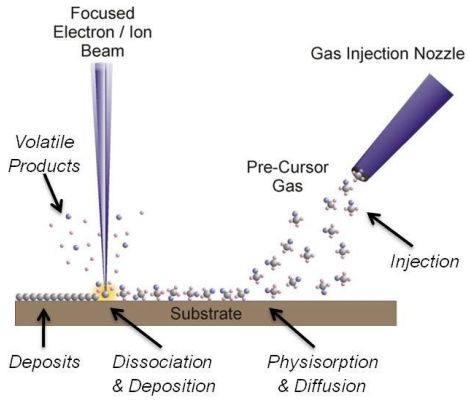

Figure 2-2: FEBID working principle [2].

The electron beam is generated in the electron column of the SEM, which is described in more detail in chapter 3.1.1. The precursor material is located in a reservoir which is heated above the melting point to vaporize the precursor. In a next step the gas is injected through a fine needle (~ 500 µm inner diameter) into the vacuum chamber. To provide a high gas flux and gas pressure in the desired area the needle is placed near the focus of the electron beam (~ 100 µm radial distance) about 200 µm above the sample surface. The entire system is called gas injection system or shortly GIS throughout this thesis. Beside a controlled gas flux and appropriate precursor vapor pressure a good vacuum is essential, because impurities originating from the background pressure will influence the chemistry and by that the functionality of the final deposit.

2.1.1 Precursors

FEBID precursor have to fulfill several, partly strict requirements. The gas molecules should be adsorbed and diffuse on the specimen surface. After some time, they should leave the sample again, ideally without any chemical interactions. To ensure this behavior the precursor molecules have to be uncharged. However, a small dipole moment or polarizability is needed for the sticking probabilities.

After the interaction with electrons the precursor molecules have to dissociate, the desired part should remain on the surface without any further movement while the unwanted fragments should be entirely split off and desorb immediately to prevent any chemical alternations. Furthermore, the volatile fragments should not be reactive and be able to be pumped away easily. A complete survey of available precursors and related issues can be found in [3].

In reality most of the precursors fulfil many but not all requirements. In most cases, some carbon fragments are not entirely split of the main complex leading to increasing carbon contents [4]. Recent work at the FELMI demonstrated how the unwanted carbon can entirely be removed within seconds without losing their intended shapes [5].

In this study the widely used Pt precursor $MePtCpMe_3$ has been used due to the high experience at the FELMI on the one hand and its tunable conductivity on the other hand [6,7] which is essential for this study. Further details can be found in section 2.2.

2.1.2 Deposition process

Like mentioned above the precursor molecules are dissociated by the impinging electrons. The volatile fragments leave the surface and are pumped away by the vacuum system while the non-volatile precursor parts stay on the surface and forms the deposit. The rate of dissociation is dependent on two factors, the precursor molecule density and the number of impinging electrons. Simplified the adsorption can be described by [1]:

$$\frac{\partial n}{\partial t} = \underbrace{sJ\left(1-\frac{n}{n_0}\right)}_{\text{adsorption}} + \underbrace{D\left(\frac{\partial^2 n}{\partial r^2}+\frac{1}{r}\frac{\partial n}{\partial r}\right)}_{\text{diffusion}} - \underbrace{\frac{n}{\tau}}_{\text{desorption}} - \underbrace{\sigma f(r,E)n}_{\text{decomposition}} \qquad (2.1)$$

with the number of adsorbed molecules per surface unit ***n***, the coverage $\boldsymbol{n/n_0}$, the sticking probability ***s***, the gas flux ***J***, the diffusion coefficient ***D***, the time constant for thermal desorption ***τ***, the dissociation cross section ***σ*** and the spatially varying and energy dependent electron flux ***f(r,E)***. The equation can be split in four terms as indicated that describe following processes:

1) adsorption from gas phase

2) diffusion on the surface, dependent of the concentration gradient

3) thermally stimulated desorption

4) molecule dissociation by the electron beam

The deposition rate can be described for rotational symmetry by the equation

$$R(r) = Vn(r)\int_0^{E_0}\sigma(E)f(r,E)dE \qquad (2.2)$$

with ***V*** the volume of decomposed molecules, ***n*** the number of adsorbed molecules per surface unit, ***E*** the energy of primary electrons, σ the dissociation cross section and the electron flux distribution ***f(r,E)*** [[1]]. Please note, although complex enough, this is just a first approximation only considering direct interactions. In reality also reemitted electrons can essentially participate at the deposition process like back- and forward-scattered electrons (BSE and FSE, respectively) as well its entailed secondary electrons type II (SE_{II}) and type III (SE_{III}), respectively, which can have strong influences on chemistry and morphology (see chapter 3.1.1.3).

2.1.3 Growth rates

As described before, two major parameters for the growth process are the electron density (***f(r,E)***) and the time dependent precursor density in the relevant areas. The electron density can be controlled quite easily by changing the beam current during deposition. The precursor density on the specimen surface can be varied by changing the geometry of the gas injection needle [1,8,9], by changing the distance between tip and surface or by changing the gas pressure.

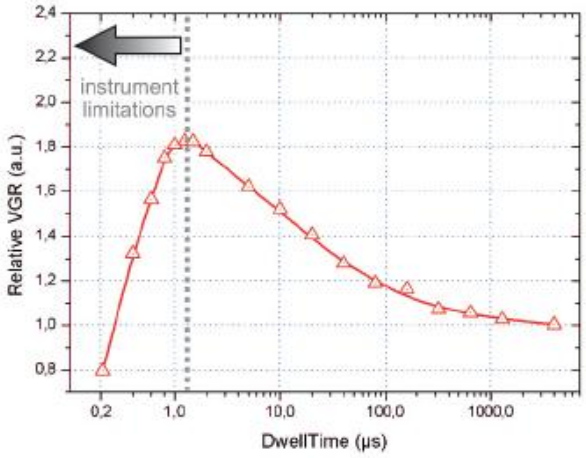

Figure 2-3: Volume growth rate dependency of the dwell time [2]

When the electron beam stays on a single spot for some time, precursor depletion follows in this area, because the initial molecules have been converted to the deposit and the area has to be replenished again by surface diffusion. Basically, we can distinguish between the so called Mass Transport Limited (**MTL**) regime where the deposition rate is limited by a lack of precursor molecules and the Reaction Rate Limited (**RRL**) regime where enough precursor molecules are available, but the deposition rate is limited by the number of available electrons for dissociation. Beside morphological issues also varying deposit chemistries can be the consequence. This indicates the importance of two parameters which are highly relevant for the growth process: ***1)*** the *dwell time*, which describes the single point pulse duration; and ***2)*** the *refresh time*, which declares the time in which one point is free of illumination, so that precursor replenishment can take place via surface diffusion and gas flux adsorption [1,9]. 2- or 3-dimensional geometries can be produced by rasterizing the electron beam over the substrate surface several times (patterning loops) or via varying dwell times in a predefined pattern. The main parameters that influence the growth, shape and composition of the structures are the primary electron beam energy, electron current, dwell time, point pitch and refresh time. There is a number of further parameters that influence the writing process like the precursor flux,

the shape and geometry of the substrate, the material of the substrate, the position and type of the GIS, and others [1,9,10,11].

2.2 Pt precursor

As precursor trimethyl-mehylcyclopentadienyl-platinum ($MePtCpMe_3$) was used which is widespread used due to its non-reactive character, chemical stability and the conductive properties. The molecule is shown in Figure 2-4 while a fully dissociated precursor cracks in at least 5 fragments as shown in Figure 2-5 .

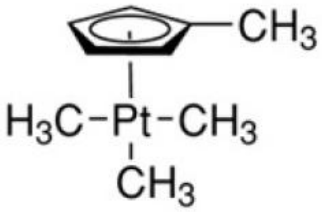

Figure 2-4: Chemical structure of $MePtCpMe_3$.

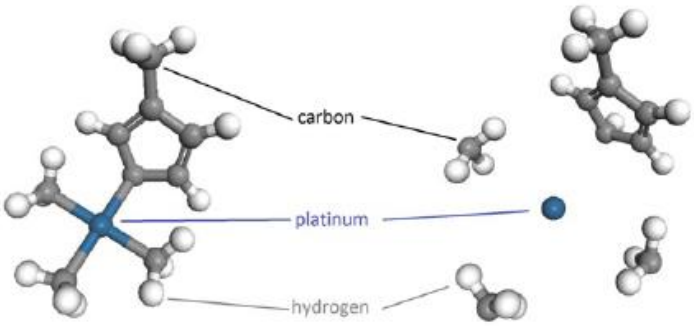

Figure 2-5: Precursor and fragments after ideal dissociation

For full dissociation several electron interactions are needed which complicates the achievement of defined chemistry. After deposition, the final structure consists never of pure platinum but of small Pt-crystals (~ 2 nm) embedded in a carbon-hydrogen matrix with a typical Pt content of 15 at.% [1,4]. This results in conductivities about 5 to 6 orders lower than that for pure Pt. The carbon matrix also influences the final density and by that the stiffness of the deposit in case of free standing structures as used for this thesis. It is possible to manipulate the material properties by changing the chemical composition of the matrix as described later in this thesis or by post growth purification.

2.3 Mechanical studies of FEBID deposits

Static and dynamic experiments are well suited for finding mechanical material properties like stiffness, density, strength, toughness, adhesion [1,8]. Up to now there exist only very few data for FEBID fabricated deposits and in particular no studies for the used Pt precursor.

In this thesis emphasis is put on the determination of the Young's modulus and overall densities of Pt based deposits. Bending and vibration experiments are well suited which has been basically done by

Ivo Utke et-al. [8,12]. In particular, that group produced high aspect-ratio, quasi 1D single-pillars with uniform cross-section by using $Cu(C_5HF_6O_2)_2$ precursor. To find the Young's modulus they performed bending tests with a calibrated reference cantilever made of SiO_2 with known force constants with. The tips of the single- pillar and the cantilever was brought together and moved against each other by a piezo stage until bending occurred like shown in Figure 2-6.

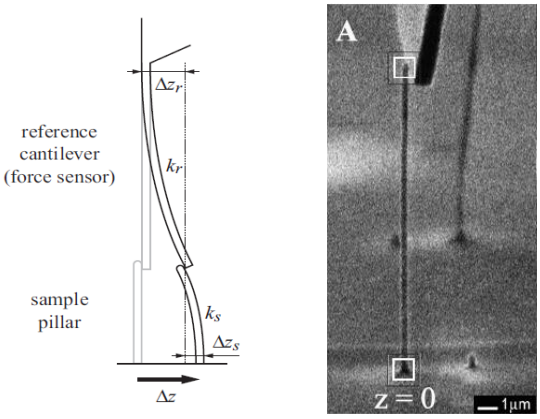

Figure 2-6: Experimental setup of bending experiment to access the Young modulus [8,12].

By measuring the deflection of the sample and / or the reference cantilever, the force can be calculated by

$$F = k_r \Delta z_r = k_s \Delta z_s \tag{2.3}$$

Where ***F*** is the force perpendicular to the pillar main axis, $\boldsymbol{k_s}$ and $\boldsymbol{k_r}$ the force constants and $\boldsymbol{\Delta z_s}$ and $\boldsymbol{\Delta z_r}$ are the deflections for the sample pillar and the reference, respectively. The Young's modulus ***E*** of a cylindrical pillar can be then obtained from

$$E = \frac{64}{3\pi}\frac{l^3}{d^4}k_s \tag{2.4}$$

where ***l*** and ***d*** is the pillar length and diameter, respectively. To find the density of the pillars Utke et-al performed additional mechanical vibration tests like shown in Figure 2-7 to find the resonance frequencies of the single pillars.

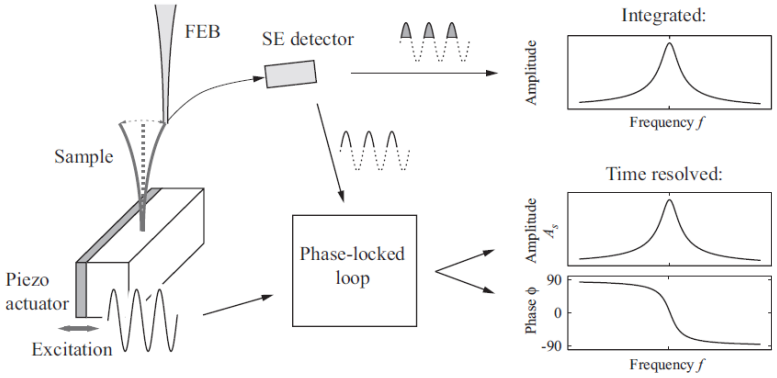

Figure 2-7: Piezo-driven vibration experiment for determination of the resonance frequency [8,12].

The pillars were then mechanically excited by a piezo driven actuator. The exciting frequency was varied until the pillars resonance frequency was found which manifests itself in an overshooting of the pillar deflection. Since the electron beam is stationary and the substrate is moved with the excitation frequency, the pillar deflection signal from the SE detector is overlaid the moving background signal. A lock-in amplifier has been used to separate between excitation and pillar frequency, allowing the determination of deflection-amplitude and -phase. By sweeping the frequency and detecting the position of the peak maximum the resonance frequency can be determined.

The resonance frequency for arbitrary geometries can be mathematically described by

$$f_n = \frac{(\beta_n h)^2}{2\pi h^2}\sqrt{\frac{I}{A}\frac{E}{\rho}} \tag{2.5}$$

where ***h*** is the height, ***A*** is the cross-sectional area, ***I*** the area moment of inertia, ***E*** the Young's modulus determined from the bending experiments and ***ρ*** the density of the pillar. The resonance frequency for pillars can be derived by using the area moment of inertia for cyclic areas which is given by the equation

$$I_{zPillar} = \frac{w^4\pi}{4} \tag{2.6}$$

were ***w*** is the width of the pillar. This leads to the equation for the fundamental resonance frequency for cylindrical pillar deposits as one of the key equations for this thesis:

$$f_{1Pillar} = 0{,}1399\sqrt{\frac{E}{\rho}\frac{w}{h^2}} \tag{2.7}$$

By rearranging the formula ***ρ*** can be obtained since all the other parameters are known. For comparison the derived parameters for a $Cu(C_5HF_6O_2)_2$ deposited with 5 keV and 20 keV primary electron voltage and a beam current of 100 pA are summarized in Table 2-1 [8,12].

Table 2-1: Derived parameters for $Cu(C_5HF_6O_2)_2$

	5keV	**20keV**
Young's modulus E	17 ± 6 GPa	25 ± 8 GPa
average density ρ_A	2,2 ± 0,2 g/cm³	2,8 ± 0,2 g/cm³
matrix density ρ_M	1,2 ± 0,3 g/cm³	2,2 ± 0,5 g/cm³
Quality Factor Q	145-550	194-316

2.4 Electrostatic resonance concept

Another method to perform the bending and vibrational tests was developed in this thesis. The idea was to produce the deflecting forces electrostatically for first tests and then via AC voltages at the mechanical resonance frequencies. Starting point for the theoretical considerations was the force acting on the stationary electrodes of a plate capacitor which can be described by

$$F = \frac{1}{2}\varepsilon_0 A \left(\frac{U}{2d}\right)^2. \tag{2.8}$$

where ***A*** is the area of the plates, ***U*** is the voltage and ***d*** is the distance between. It can be seen that the force can be tuned easily by changing the voltage or the distance between the electrodes. When one capacitor plate is replaced by a FEBID deposit structure with suitable geometry, it acts as second electrode. It is important to note that the deposit has to be at least weakly conductive which is the reason for using the Pt based precursor. The force acting on it leads to a bending of the structure.

The calculation of the force is quite complex as we consider a dynamical system. During the bending process the force acting on the deposit changes because of the varying distance between deposit structure and electrode. Furthermore, the geometry of the deposit and also the electrode can be quite complex. Even physic simulation programs like COMSOL or ANSYS that use finite element methods to solve the differential equations can have trouble with finding a solution.

In chapter 3.4 a concept is presented which allows calculating the force acting along the structure which is necessary to determine the Young's modulus. The electrostatic method has some advantageous in comparison with the previously described one. For the mechanical bending experiments cantilevers are needed that have force constants similar to the force constants of the investigated deposits, so that the deflection of both is comparable. Different cantilevers have to be produced or adjusted to match this requirement. When using the electrostatically setup, the force and thus the bending, can easily be varied by changing the excitation voltage. In comparison to the mechanical vibration excitation via a piezo stage, used by Utke and Friedli et-al, both the electron beam and the bulk are stationary, whereby the lock in amplifier can be omitted. Therefore, the SE signal is overlaid by noise that comes from the interaction from the SE electrons with the alternating exciting field. By choosing appropriate primary electron energies and suitable detector settings this effect can be minimized like shown later. The disadvantage of the electrostatic concept is, like mentioned above, that only conductive deposits can be examined.

2.5 Gas sensing concept

One of the main motivation for this thesis was to provide fundament for the development of nano-resonator based gas sensor. It is based on FEBIDs 3D capabilities, which allows fabrication of free-standing nanostructures with diameters below 50 nm while enormous lengths such as 15000 nm can be realized. Such narrow structures are furthermore known to be flexible and conductive both based on the unique nano-granularity of FEBID materials. With that in mind the application as resonating system had high potential which was the starting point of this thesis. As can be seen from equation (2.5) the resonance frequency of a resonator structure is strongly dependent on its mass. Although the following considerations are basically valid for every shape, they are explained for cylindrical structures (pillars) leading to the proportionality between resonance frequency and pillar mass:

$$f_{cylinder} \propto \frac{1}{\sqrt{m}}$$

This means that an increase in mass leads to a down shift in the resonance frequency. The gas sensing concept is therefore based on the change in mass when the pillar is ***i)*** brought form vacuum into a gas atmosphere due to physisorbtion of the gas molecules on the surface or ***ii)*** selective gas adsorption leads to an increase of mass due to physisorbtion. Both processes can be reversible, which would be a big advantage in comparison to reaction based chemical sensors. The working principle is shown schematically in Figure 2-8.

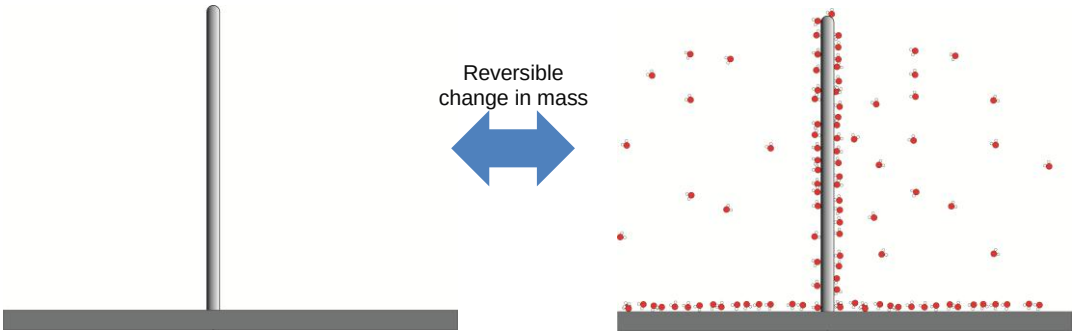

Figure 2-8: Schematic working principle of the gas sensor

Because the physisorbtion of gases only lead to a very small mass change also the pillar dimension have to be very small in order to make the frequency shift detectable. With the FEBID process pillar deposit widths of 50 - 70 nm and heights of more than 10 µm are possible. In order to estimate if this dimensions are sufficient to determine a large enough frequency shift calculations were performed. Since the values for ***E*** and ***ρ*** were not known initially for Pt-deposits the calculations were done for Cu deposits which were examined by Ivo Utke before [12]. They have a E/ρ ratio of 2.2 which were inserted into equation (2.7). The corresponding calculated resonance frequencies in a width range between 50nm and 80nm and a height range between 2µm and 10µm are shown in Figure 2-9 (left). One can see that the resonance frequency is mainly dependent on the height and only little on the width except for very short pillars. To estimate a value for the frequency shift it was assumed that one H_2O molecule adhere on the surface per nm². The increase in mass due to the H_2O molecules cause the frequency shifts shown in Figure 2-9 (right) for the heights and widths of interests. The frequency shift is highly dependent of the pillar height and independent of the pillar width. Small pillars cause a larger shift than higher ones (up to 350 Hz for 2 µm height) but all in all one can conclude that the shift seem to be large enough to make a detection possible. It also should be kept in mind that in reality much higher surface coverage is possible.

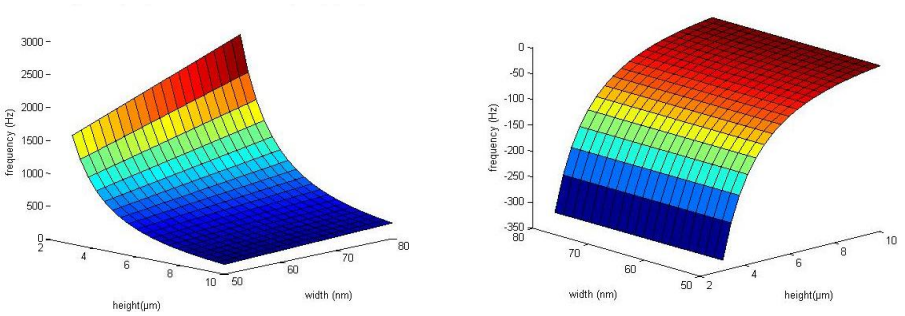

Figure 2-9: Resonance frequency dependency of the pillar height and width for Cu-deposits (left) and resonance shifts for Cu-deposits in dependence of the pillar height and width.

3 Experimentals

3.1 Dual beam microscope

The dual beam microscope (**DBM**) that was used for this thesis is the NOVA200 from FEI as shown in Figure 3-1. A DBM system consists of a scanning electron microscope (**SEM**) and a focused ion beam (**FIB**) microscope. The combination of these systems has several advantages. Specific areas can be investigated either with the electron beam, the ion beam or both beams simultaneously. Not only the surface of a sample, but also deeper lying regions can be examined by performing ion milling and simultaneously observation with electrons, ions or subsequent process like energy dispersive X-ray (**EDX**) spectroscopy to access chemical information and its lateral distribution. In this way also 3 dimensional images can be obtained. Other important fields of applications are the preparation of ultrathin lamellas for further TEM investigations or failure analysis and manipulation of integrated circuits. Beside the subtractive structuring via the FIB, a diverse range of GIS's is used to deposit materials via the ion beam or – as done for this thesis – via the much more gentle electron beam.

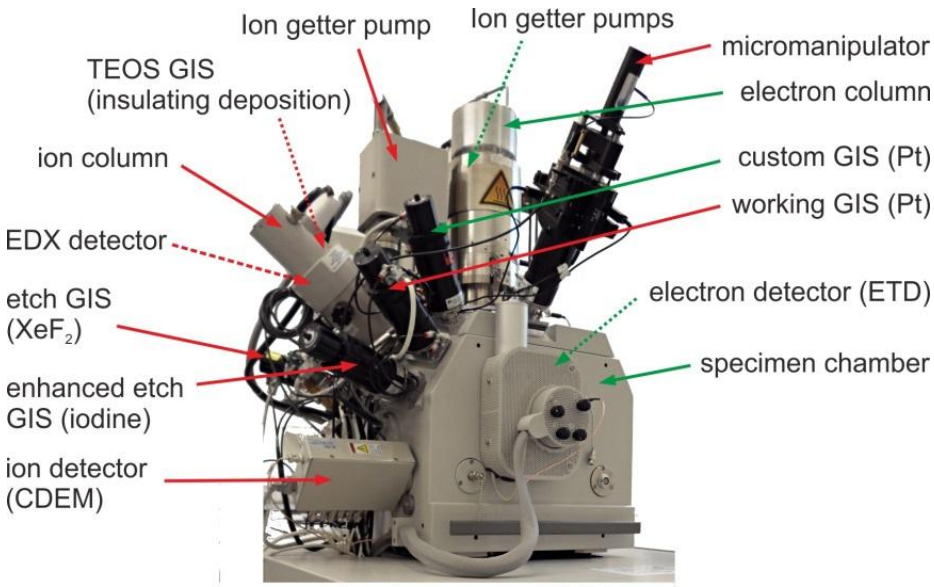

Figure 3-1: Used dual beam microscope (FEI Nova200)

3.1.1 SEM

In a SEM a finely focused electron beam is rasterized over the surface of a specific specimen. The electrons interact with the atoms and produce a variety of signals, which can be detected. By combining the actual electron position with the detected signal intensity, this can be used to analyse the topology and composition of the surface. To avoid charging effects it is very important that the specimen surface is conductive or at least conductively covered. Please note, only the most important issues are discussed in the following as excellent and very complete literature is available [13].

3.1.1.1 Components

The electron beam is generated by an electron gun that is placed on top of the column. The extracted electrons which are emitted from a very small region of an electrode are focused after the electron gun by a so called Wehnelt cylinder in a small spot called crossover as schematically shown in Figure 3-2.

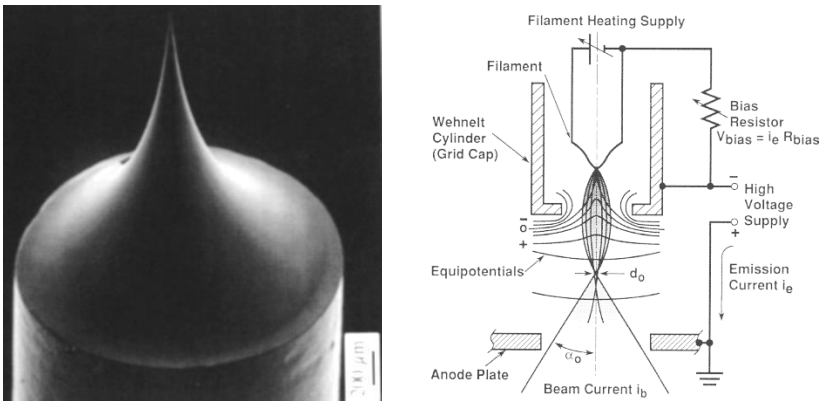

Figure 3-2: Field emission gun (left) together with a schematic figure of a field emission gun (right) [13].

There are several types of electron guns, like thermionic tungsten guns, LaB_6 and field emission guns (**FEG**) and Schottky emitters which differ in there working principle. Tungsten and LaB_6 guns are heated so that the electrons can overcome the working function and leave the surface. In FEG's a sharply pointed tip is held at a high negative potential, so that the potential gradient at the emitter surface is big enough to cause electron emission. A Schottky emitter is a combination of the other two. The described types differ strongly in brightness and lifetime. A field emission gun provides the largest current with smallest beam diameters. The NOVA 200 uses a field emission gun in Shottky configuration. The Wehenelt cylinder is used to condense the cloud of electrons produced by the filament. It consists of a negatively biased Wehnelt cap which produces a repulsive electrostatic field and an aperture. The electric field focuses the beam in a spot which is called crossover. The electrons that leave the Wehnelt originate from a small area of the tip located above the aperture (see Figure 3-2).

The electrons leave the gun as a divergent beam bundle and are accelerated by a high voltage potential through the column to the specimen surface. A system of magnetic lenses and apertures re-converge and focus the beam. The lenses consist of coils which produce a rotationally symmetrical magnetic field which is concentrated to a small area by a pole piece like shown in Figure 3-4. The magnetic field acts on the moving electrons like an optical lens. The electron path for the used SEM can be seen in Figure 3-3. The condenser system is used to control the beam current that passes down the column. The condenser lenses change the point of focus with respect to the typically used 30 µm condenser aperture. The more the focus point is distanced from the aperture plane the more electrons are blocked. The diameter of the aperture also affects the convergence angle of the beam, which has effects on the depth of focus.

Next in the ray path there are the scanning coils and stigmators. The scanning coils consist of four electromagnetic lenses that make it possible to move (raster) the electron beam perpendicular to the optical axis. The beam can be rastered over the sample by changing the current through the magnets in any desired fashion. The stigmator coils correct the asymmetric shape of the electron beam (also see chapter 0). Finally, the objective lens is located just above the sample. It has the function to focus

the electron beam on the sample surface enabling morphological / chemical investigations on the nanoscale.

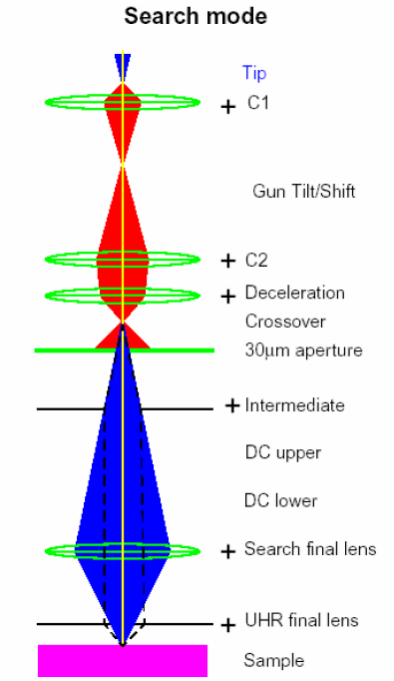

Figure 3-3: Lens system of the used SEM.

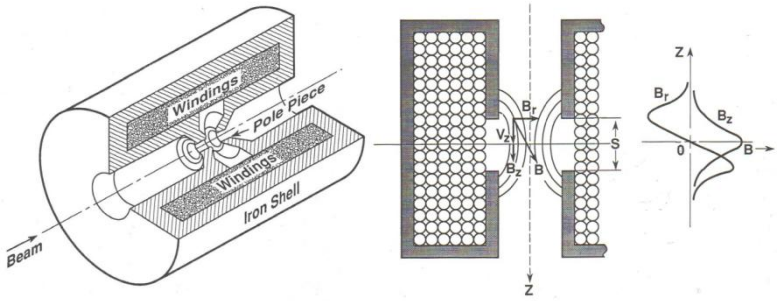

Figure 3-4: Interior of an electromagnetic lens used in a SEM (left); Schematic cross-section of the electromagnetic with the magnetic flux B_r and B_z in the lens including the plot of the magnetic components along the optical axis (right) [13].

3.1.1.2 Lens errors and compensation

All electromagnetic lenses have lens errors. This causes that not all electrons that are emanated from a point on the object plane reach the same focal point in the image plane. The most important lens aberrations, namely *spherical aberration*, *chromatic aberration* and *axial astigmatism* are briefly discussed below. A detailed description can be found in reference [13].

Spherical aberration

The magnetic field further off the optical main axis is stronger because it's closer to the magnetic poles. This means that electrons that pass close to the center of the lens are weaker deflected than those closer to the lens pieces. This results in the fact that the point source is imaged as a disk. To

reduce this effect, apertures are used which block electrons that pass the lens too far away from the optical axes. The problem is that this also leads to a decrease in electron current and for very small holes also diffraction effects occur. The aperture diameter is chosen in a way, that there is a compromise between the increase of diffraction and the decrease of spherical aberration. Alternatively, a so called C_S corrector can be applied which corrects this lens error. However, this is connected to a high financial investment and was not available on the microscope used.

Chromatic aberration

The electrons are leaving the gun with slightly different energy. This leads to different forces acting on them when they pass the lens system. Due to Lorentz law slower electrons are deflected more strongly than faster ones. The chromatic aberration can be reduced by using electron guns with a very little energy spread like FEGs and / or in combination with a so called monochromator. Again, this means a massive financial investment and is only available for instruments of latest generation.

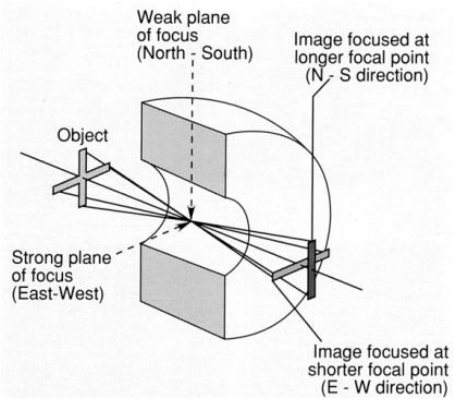

Figure 3-5: Image distortion due to astigmatism [13].

Axial astigmatism

Astigmatism is caused by asymmetries in the lenses due to production limitations. A circle in the objective plane becomes to an ellipse in the image plane as schematically shown in Figure 3-5. This also leads to a disk of minimum confusion instead of a well-defined point. The astigmatism can be compensated by inserting special lens system with at least four different poles that produce a correcting magnetic field. The lens system consists of alternating coils connected in series but wound in opposite direction to achieve different polarities. In this way it is possible to change the strength and angle of the magnetic field which controls the final beam shape. Astigmatism also plays an important role in electron beam induced deposition. It leads to elliptical shapes especially for pillar deposits and to a weaker growth rate because not the optimal focus can be achieved in all directions.

3.1.1.3 Beam Specimen Interactions

When the primary electron beam interacts with the sample, the electrons lose energy by scattering and absorption. The electron beam can either interact with the coulomb field of the specimen atoms, or with the nucleus. We distinguish between *elastic* and *inelastic* scattering. Inelastic scattering occurs, when the beam electrons interact with the electric field of the specimen atoms which leads to an energy transfer from the beam electrons to the specimen. Secondary electrons, phonons, X-rays and Auger electrons are produced. Elastic scattering occurs, when the beam electrons interact

with the nucleus of the specimen. Because of the huge mass difference nearly no energy is transferred. An elastic scattering process leads to a change in direction of the impinging electron.

Secondary electrons

Secondary electrons (**SE**) are defined as electrons that have energies below 50 eV (see Figure 3-6). They originate from inelastic scattering events. There are three types of SE electrons: ***SE(I)*** electrons are generated when energy is transferred directly from the impinging beam electron to a shell electron, which leaves the shell as SE electron. SE(I) electrons dominate in light element since less backscattering occur there. ***SE(II)*** electrons are produced from high energy backscattered electrons, that interact with specimen atoms. The SE(II) signal has a lower resolution because the depth and lateral distribution of the BSE electrons can be found in this signal. ***SE(III)*** electrons arise from forward scattered electrons (FSE) which leave the deposit and / or the sample geometry in forward direction.

Backscattered electrons

Elastically scattered electrons that are deflected back out from the substrate are termed as backscattered electrons (**BSE**). BSE electrons have energies higher than 50 eV (see Figure 3-6). As mentioned above the number of BSE electrons increase with the mass of the sample atoms, because of their larger nuclei interaction volume.

X-rays and Auger electrons

When a core electron is removed by an impinging electron a vacancy occurs. An electron from a higher energy level may fall into this vacancy which results in a release of energy. The released energy can either be transferred radiation-less to an electron of an outer shell, which leaves the atom as auger electron, or it can be released as X-ray photon.

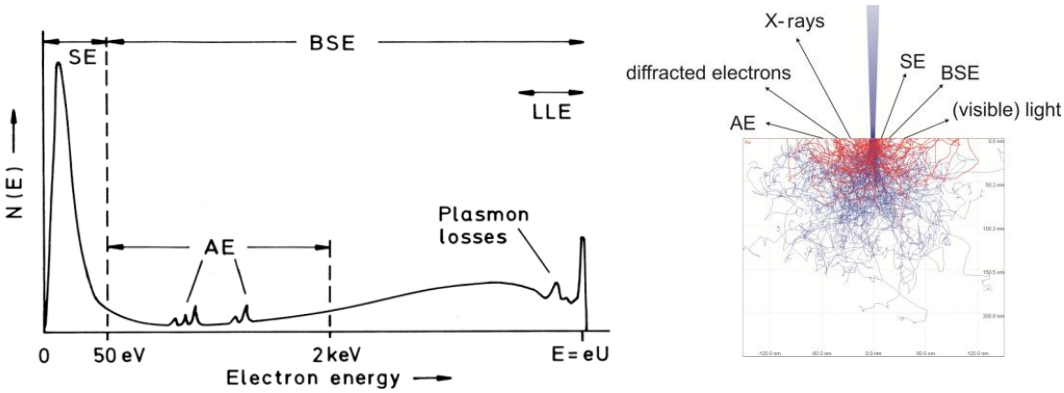

Figure 3-6: Energies of the emitted electron signals (left); Monte Carlo simulation of the interaction volume for the different particles (right).

The interactions described above occur in a specific area, the so called interaction volume. The size and shape of the interaction volume depends on several parameters, the primary beam diameter, the primary beam energy, the atomic number and the density of the specimen and the tilt of the surface. The interaction particles have a different escape length and can be used for further investigations of the material composition or for imaging the surface of the specimen. SE's originate from areas close to the surface up to 50 nm depth which means that they give a good spatial resolution. So they are well suited for surface imaging. BSE's can originate from a hundred times

deeper regions due there higher kinetic energy. Since the BSE yield depends on the atomic number of the specimen they give a good mass contrast.

X-rays have the largest escape length and a relatively bad spatial resolution. In SEMs mostly characteristic X-rays are used, because their spectra show material specific lines that can be used for composition analysis.

Figure 3-6 illustrates the trajectories of different electrons inside a SiO_2 bulk material determined by a Monte Carlo simulation with impinging electron energy of 30keV. The red curves belong to electrons that leave the surface again after several scattering events. They show the trajectories for BSE's and show their maximum escape length. The blue trajectories show electrons that lose all their energy inside the bulk material. It can be seen that the maximum penetration depth is much larger than the escape length of the BSE's. The maximum penetration depth corresponds also to the deepest regions where X-rays can originate.

3.1.1.4 Detectors

SE and BSE electrons are typically detected with an Everhart-Thornley detector (**ETD**). An ETD consists of a scintillator that is located behind a grid (see Figure 3-7). For secondary electron imaging a low positive voltage is applied to the grid, which attracts just the low energy SE's. Higher energy electrons are not attracted and will only reach the detector if they leave the surface randomly in the detector's direction. They only make a small contribution to the overall-signal. BSE can be detected when a negative bias higher than 50 V is applied to the ETD grid. This allows qualitative imaging of the material contrast. The incoming electrons are accelerated on the photocathode of a scintillator by a high positive voltage and are converted to light there. Then the signal is amplified by a photomultiplier, which is read out electronically (see also Figure 3-7). The ETD detector is located beside the specimen. The tilt angle of the ETD and the low energy of the secondary electrons cause a "shadowing effect", which means that areas that are facing the detector look brighter than areas that are on the averted side. This produces a 3D impression of the surface. The shadowing effect can be avoided by using another detector, the so called Through-the-Lens detector (**TLD**). The working principle is comparable with the ETD, but it is installed in the electron column, hence giving a top view of re-emitted electron species.

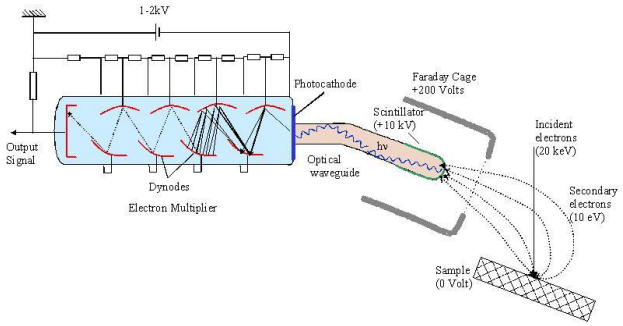

Figure 3-7: Schematic view of the Everhart Thornley detector [13].

3.1.1.5 Image Formation

A SEM image is created by rastering the focused electron beam over the specimen surface. This is done in discrete steps, typically from left to right and top to bottom. So the chosen resolution affects the number of pixels in every row and also the number of rows. The beam stays on each point for a predefined time called the ***dwell time***. In this time the primary beam interacts with the particular point and produces the signals that can be detected. Their intensity is converted into a grayscale value of the corresponding pixel on the monitor. A long dwell time improve the image quality because of the higher signal intensities, but can cause local charge leading to lateral drift and also to sample interactions due to the high electron dose. This plays a big role especially for the Pt-C deposits examined in this thesis. There is also another possibility to improve the image quality by making several images of the same area with short dwell times and sub sequent integration or mean value formation. To change the magnification the size of the rasterized area has to be changed while the resolution stays the same. This is simply done by reducing the distance in between neighbored pixels (***point pitch***). The maximal resolution is limited by the minimal beam diameter which is dependent on lens errors (see chapter 3.1.1.2) and can be improved by using corrector lenses. Also the emission properties of the investigated material can influence the finally achievable resolution. Main factor, however, is the primary energy as higher energies gives a finer spot but also lead to higher penetration depths which widens the radius of re-emitted electrons leading therefore to reduced lateral resolution. Hence, strong efforts have been put on generating a very small beam diameter even at very low primary energies such as 1 keV and less.

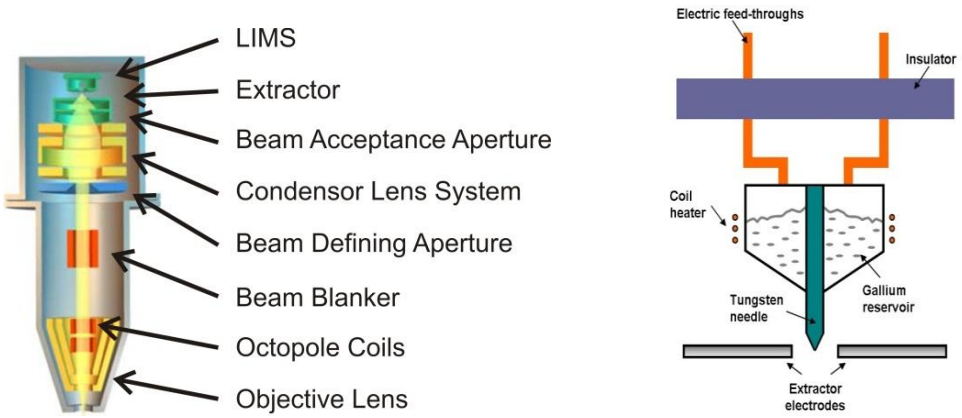

Figure 3-8: Schematic structure of the ion column (left) and schematic structure of the liquid ion metal source.

3.1.2 Ion Beam

The ion column of the FEI Nova 200 works like most other FIB microscope with Ga^+ ions. The schematic setup of the column is shown in Figure 3-8. The ions are produced in the liquid ion metal source (**LIMS**), which consist of a reservoir filled with gallium that is heated over the melting point. Due to gravity and wetting tendencies the liquid gallium creeps down a tungsten hairpin that is connected to the reservoir and forms a drop at the tip. In the electrical field of a so called extractor the drop is deformed to a Taylor cone with an end radius of just a view nm. Because of the large curvature and the high electric field intensity there atoms in a small area on the tip of the Taylor cone are evaporated and ionized and then extracted by the extractor potential. The beam is directed

through a beam acceptance aperture and subsequently to the condenser lens system, which has the function to collimate the beam und to accelerate the ions to the desired energy between 5 keV and 30 keV. The beam current can be adjusted by using different beam defining apertures. The function of the beam blanker is as the name tells to blank the beam within sub-µs by redirecting it sideward. The scanning and astigmatism correction is done in the lower part of the ion column via octopole coils. The object lens focuses the ion beam onto the substrate surface.

Due to their high mass and physical size the Ga^+ ions they cannot penetrate deep into material. Their energy is absorbed in a relatively small interaction volume in comparison to that of electrons. The penetration depth lies between 5 and 100 nm dependent on typical the primary ion energy and the substrate material. The ions collide with surface near atoms and transfer part of their momentum which leads to the removal of surface material called sputtering: This can be used for ion milling. The penetrating ions also generate lattice defects by knocking out atoms from their positions until they are stopped. After ions have lost their energy they get stuck and are implemented in the substrate. The atoms that are knocked out from their position cause follow up processes. A large amount of SE's is released that can be detected. Also plasmons and molecule vibrations are excited which leads to large temperature increases in the region of the ion beam. An important effect is the re-deposition, where sputtered material accumulates again in regions close to the ion beam. This is especially a problem when deep and narrow structures should be produced by ion milling when the sputtered material is attached to the walls again. Again there exists complete FIB literature and only the most relevant issues are discussed in the following. Much more details can be found in references [1,14,15,16].

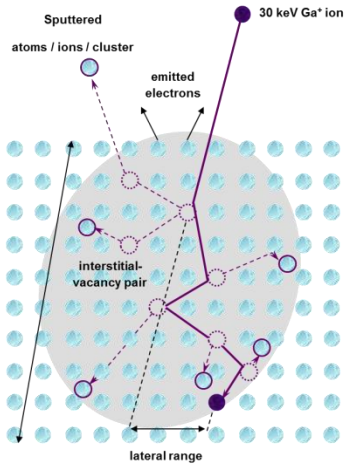

Figure 3-9: Direct and indirect effects due to ion bombardment.

3.1.3 Omniprobe

The used DBM is equipped with an 3-axes Omniprobe micromanipulator consisting of a fine tungsten tip with about 10 µm end radius in standard configuration. It is used to physically interact with the sample in the microscope where a high level of precision in the movement is necessary. It can be used for several manipulation processes like nanowire manipulation or FIB lamella extraction. However in our case it was mostly used for conducting very small electrodes. As mentioned above, the manipulator consists of a very fine tungsten tip which can be replaced if it is damaged or worn out and of a positioning system which is independent of the stage. The tip is retraced by default and

can be inserted pneumatically via the microscopes user interface. As we have the FIB available it is also possible to shape the micromanipulator accordingly to the requirements. This has been done throughout this thesis as it will be discussed whenever needed.

3.2 Used software packages

3.2.1 COMSOL Multiphysics

COMSOL is a software package available at the Graz University of Technology which is used to perform physical or engineering simulations. It uses the finite Element Method (**FEM**) to find solutions for a diverse range of problems. One of the main advantages of COMSOL is that coupled physical systems also can be studied. The software has a modular structure. The base package comes with the *Multiphysics* module. There are several add-ons available that are used in different physical fields. For our simulations we used 2 add-ons, namely "*AC/DC*" and "*Structural Mechanics*". The "*AC/DC*" module is used for electrical problems like the simulation of capacitors, inductors, power cables, electrical motors, electrical generators, sensors etc. The "*Structural Mechanics Module*" is used to perform classical stress and strain analysis. The COMSOL package also offers a "Matlab Live-Link" interface that allows a script control for COMSOL using Matlab language and extending the functionality by giving the possibility of pre- and post-processing the data with Matlab [R2012b].

3.2.2 Labview

Labview is a graphical programming interface developed by *National Instruments* [v12.0 (32bit)]. It uses a graphical programming language called ***G***, which is a data flow programming language. The software consists of two components, the front panel, which is the interface to the user, and the block diagram which contains the graphical programming code. To build Labview programs and function blocks (also referred to as virtual interface or VI), the user connects pre-defined function-nodes by drawing wires. Every VI is executable autonomous and can be used as sub routine in every other VI, by linking the VI's in and outputs together or to other function-nodes in a correct way. In this thesis Labview was mainly used to control the Picoscope PC oscilloscope hardware, because the provided software was not well suitable for the experiments.

3.2.3 Tracker

The analysis of the resonance curves was done with the program "*Tracker*" [v4.80] which is an open-source video analysis software. It is used to analyze the motion of objects in videos. The software allows manual object tracking and also auto tracking of the position, velocity or acceleration of objects. Also the determination of angles, angular velocities and angular accelerations with respect to a predefined coordinate system is possible. The typical workflow is to import the video file, calibrating the scale by a known distance in the video, defining the position and angle of the coordinate axis and then start the tracking process. There are two possibilities to track objects, either manually or by defining force expressions and initial conditions and bringing them to consensus.

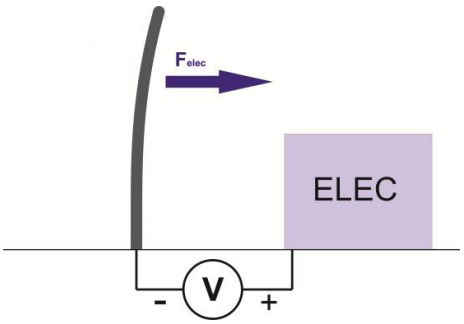

Figure 3-10: Schematic setup for electrostatic bending measurements

3.3 Electrostatic measurement

3.3.1 Patterning and Milling

The DBM can be used to structure the sample surface by ion milling, deposition via the focused electron / ion beam (**FEBID / FIBID**) or focused electron / ion beam induced etching (**FEBIE** / **FIBIE**). Patterns are used to define the geometric shape and other process parameters. Either the electron beam or the ion beam can be used for patterning whereas the electron beam does not show sputtering effects, unwanted material implantation or partly enormous local temperatures as it is the case for FIB assisted processes. During patterning the beam is unblanked and directed across the surface like defined before. When performing FEBID or FEBIE the GIS valve has to be opened to provide the precursor molecules at the area of interest. In principle there are three possibilities for defining a pattern: the internal FEI patterning generator, bitmap import or – most sophisticated - streamfiles which allow an enormously flexible beam control.

3.3.1.1 Patterning tools

A number of patterning tools is available to create patterns directly in the image window of the user interface of the microscope. Pattern shapes like rectangles, circles or polygons can be drawn which compose the overall pattern. The milling or deposition can be done parallel for all defined shapes or in a serial sequence in defined order. The patterning properties can be defined for each shape individually. Important properties that were varied during the experiments are:

- *Gas Type*: Defines the gas that should be used for the patterning process
- *Pitch X / Y*: The distance between two points
- *Scan direction*: Defines the final edge the pattern will scan towards
- *Refresh Time*: The time between two loops
- *Scan Type*: The scanning strategy, can be set either to serpentine or to raster
- *Fill Style*: Defines if just the edge or the whole area of the drawn shapes should be milled
- *Passes*: The number of passes the beam scans over the pattern
- *Defocus*: The defocus of the beam influences the beam diameter and area
- *Blur*: Similar to defocus, defines the diameter of the blurred spot explicitly

The magnification should be set in a way, that the defined pattern fills about 30 % - 50 % of the screen. If it is too low, the edges become round, if it is too high, the pattern doesn't fit on the screen. The background of these effects is the available number of pixel points via the patterning engine. The current value has to be set before the patterning process is started.

3.3.1.2 Bitmap Pattern

Instead of drawing the patterns in the image window, bitmaps can be imported which define the shape of the pattern. Each pixel in the *.bmp*-file consists of the colors red, green and blue. The red component is not used for patterning. The green component is responsible for the beam blanking. If it is zero the beam is blanked, otherwise it is unblanked. The blue component represents the dwell time for each pixel. A zero value corresponds to a dwell time of 100 ns and a value of 255 corresponds to the maximum dwell time defined in the user interface. Values in between are linearly interpolated.

3.3.1.3 Streamfiles

Streamfiles are ASCII files with code to produce custom patterns. The used patterning engine supports a 16 bit resolution. This means that the field of view is divided into 65535 points in X and Y direction. Every streamfile must start with the letter "s" in the first line. The second line defines the number of iterations and in the third line defines the total number of X and Y coordinates. All the following lines describe the pattern points. The first value is the dwell time, the second the X-coordinate, the third the y-coordinate and the fourth one describes if the beam is blanked (0) or unblanked (1). The structure of an example streamfile is shown in the example below:

```
s
200
4
1000    1000    1000    1
1000    1000    1500    1
1000    1000    2000    1
3000    1000    1000    0
```

This example shows a streamfile for FEBID and produces three separate pillars with a distance of 500 pixels between them. The real distance depends on the magnification and can be calculated by

$$d = \frac{167600000 * w * \mathrm{dpx}}{mag * n} \tag{3.1}$$

where ***d*** is the distance in nm, ***w*** describes the window size and is 1 for a small image window and 2 for a large image window, ***dpx*** is the distance in ***px***, ***mag*** is the magnification and ***n*** is the number of pixels in x direction of the field of view. The pattern in this example is looped 200 times. It is

important to mention that the fourth point (last row) is blanked and does not contribute to the deposition process directly. Rather, it adds an additional refresh time to the loop.

3.3.2 Measurement setup

The basic setup for the electrostatic deflection measurements is shown in Figure 3-10. To provide the direct input voltage a *Keithley 230* programmable voltage source is used which has a range from -100 V to +100 V. The source can either be connected to the Omniprobe micromanipulator or to the active stage holder which both are used to apply an electric contact to the deflecting counter electrode of the FEBID structure (details about the active sample stage holder can be found in the Master Thesis of Florian Kolb [17]).

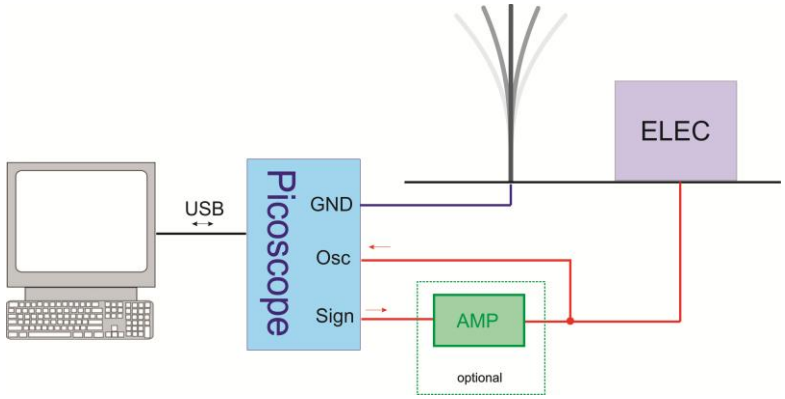

Figure 3-11: Measurement setup for resonance experiments

For the resonance frequency measurements the voltage source was replaced by a signal generator. In our experiments a Picoscope 3204A computer oscilloscope with build in signal generator was used for this purpose. The measurement setup can be seen in Figure 3-11. The signal generator is able to produce sinus, square, triangle and AC signals with a maximum frequency of 1MHz and maximum amplitude of ±2 V. Because this amplitude was too low for some experiments, an external optional amplifier circuit was developed which was used to boost the signal. The amplifier circuit and the corresponding schematic are shown in Figure 3-12.

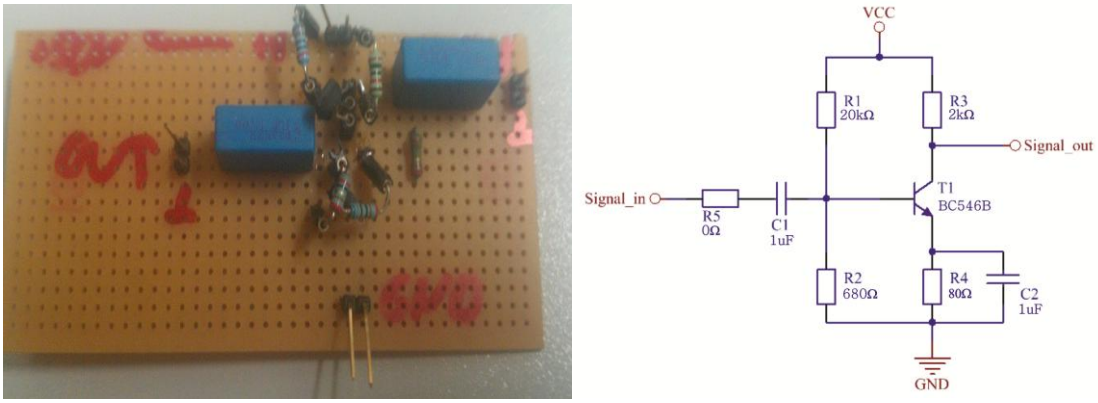

Figure 3-12: Signal amplifier circuit (left) and schematic of the circuit (right)

This circuit acts as a low pass filter, so low frequencies are amplified more than high frequencies. To prevent that the signal amplitude changes during a frequency sweep the amplified signal is looped back to the oscilloscope input. The amplitude is detected continuously by the Labview VI which readjusts it accordingly (see chapter 3.3.3.2).

3.3.3 Measurement and data analysis

3.3.3.1 Electrostatic deflection measurement

The precise measurement of the electrostatic deflection is necessary for closer material investigations, especially to determine the Young's modulus or the density. The measurement of the electrostatic deflection of the FEBID structures can be done in two steps. At first the desired voltage has to be applied to the deflecting electrode. Then the deflection can be determined by making an SEM image of the FEBID structure in bend state. This can be done from top view and also from side view, with tilted stage. However, it has been found that the first variant is much better because the radiation dose, which leads to material damage and additional bending effects can be minimized in this way due to the decreased illuminated deposit area. To further minimize the exposure damage the observation voltage should be set to the maximum of 30 keV since the high energy electrons don't interact with matter as strong as lower energy electrons. For optimal results of the measurements the structures should not be irradiated permanently. Instead it's better to take just one image after each change of the applied voltage and to use the lowest possible electron current.

3.3.3.2 Electrodynamic resonance measurements

The resonance experiments are a bit more complicated. To find the resonance frequency a frequency sweep has to be performed while keeping an eye on the SEM live image and watching if the deposit goes into resonance. A Labview program was developed that directly accesses the computer oscilloscope and makes it easier to observe the resonance frequencies. It has functions to locate the resonance frequency and to observe the resonance behavior in detail which are described below. The user interface is shown in Figure 3-13. In the following the individual functions are described:

Wave Type: Here the wave type can be set. It can be chosen between a sine, a triangle and a square waveform

Generator on/off: With this button the signal generator output can be switched on or off

Voltage settings: This block is used to regulate the output voltage of the signal generator. One opportunity to do this is to set it directly via the voltage scrollbar in the range between 0 and V_{PP}. Care has to be taken when the optional amplifier circuit is used, since it boosts the output voltage which means that it is much higher than the set value. The second opportunity is to enable the "U Auto Adjustment" button and to set the desired value in the box beneath. The looped back output voltage is directly measured via the build in oscilloscope and compared to the desired value. This is especially important when using the optional amplifying circuit since the auto adjusting feature makes it possible to permanently regulate the input voltage of the amplifier so that the output voltage corresponds to the chosen one.

Frequency settings: In this block the output frequency of the signal generator can be set. It is important that the "Mode" setting (5) is adjusted to "normal" when working in this block. The "Frequency" scroll bar is coarse frequency settings between 1kHz and 1MHz. The "Fine Tuning" scroll bar can be used to make fine adjustments of the above set frequency. The set overall frequency can be seen in the "actual frequency" field (7).

Very useful are also the "+" and "-" buttons on the right which can be used to increase or decrease the frequency by the value specified in the box.

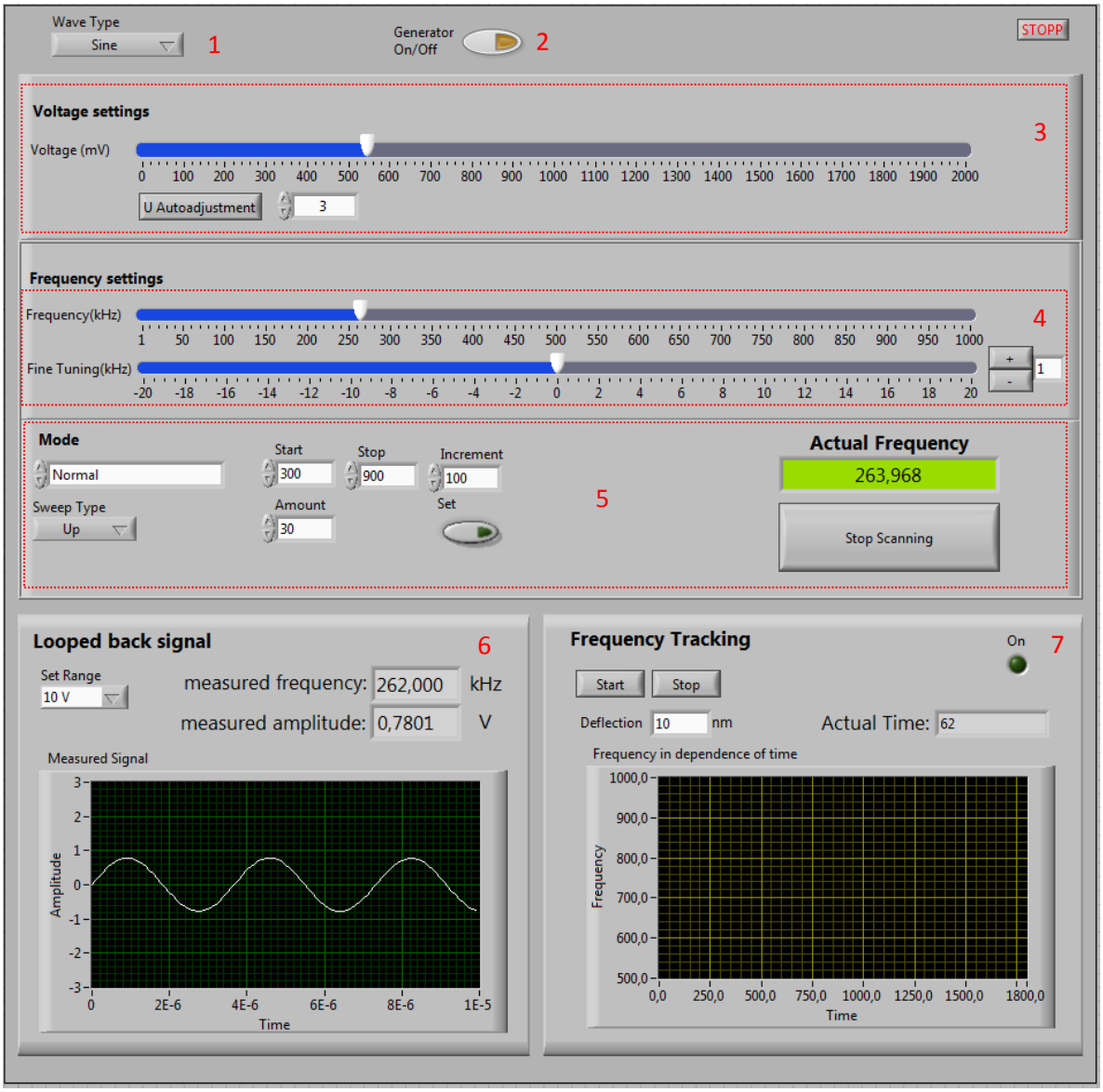

Figure 3-13: GUI of the developed software.

Operation Mode: There are different operation modes that can be used. They are explained in detail below:

- *Normal:* This mode is used to manually choose the output frequency with the frequency settings instruments (4)

- *Search Frequency:* This mode allows searching for the resonance by performing a frequency sweep. The search interval can be set by adjusting the value for the start and end frequency in the corresponding fields. The sweep speed can be set in the field "Increase". It is given in Hz/s.
- When the resonance frequency is reached the "stop scanning" button can be pressed. This causes a stop of the frequency sweep and the actual frequency is maintained which is displayed in the "Actual Frequency" field. Also the mode is automatically switched back to the "normal mode" were fine adjustments can be done. The "stop scanning" button can also be activated by pressing the "Enter" key. This is helpful, since the SEM live image where the resonance case is observed is running on another computer than the Labview software.
- *Sweep Around Frequency:* This mode should be chosen when observing resonance curves. A sweep around a middle frequency is performed, that can be set in the block "frequency settings "(4). The bandwidth of the sweep can be set in the field "Amount" in kHz. The direction of the sweep (up, down, up and down) can be set under "Sweep Type".
- *Set button:* has to be pressed to make the changes in the "Mode" section become active.

Looped back signal: In this block the waveform, amplitude and frequency of the looped back output signal is shown which can be used to check it. Under "set range" the maximum amplitude range for the output signal can be changed, so that the measured waveform optimally fits in the "Measured Signal" graph.

Frequency Tracking: This feature can be used to track the changes in frequency with time. The value of the set frequency is stored every second. Also a corresponding deflection value can be stored simultaneously. By hitting the "Start" button the tracking can be started, by hitting the "Stop" button it stopped and the data is stored to a desired file.

3.3.3.3 Measurement and evaluation of resonance curves

The resonance curves of the FEBID structures were observed by performing a frequency sweep. The "*Sweep Around Frequency*" mode of the Labview program described in 3.3.3.2 was used for this. While performing the frequency sweep a video of the deflections was recorded for each structure. The videos were further examined in the program "Tracker" like shown in Figure 3-14. With this program the points of maximum deflection were tracked for each frame (red and blue points in the image). This had to be done manually cause of the relatively large noise in the records. The zero point of the coordinate system was placed at the center of the FEBID structure. This makes it possible to track the deflection angle simultaneously to the maximum deflection in dependence of the frame time. **Please note, the mentioned angle means the directional orientation and not the phase angle between voltage and current as used for the electrical characterization.** Since the start and end frequency of the sweep (f_{start}=f_{mid}-amount/2, f_{end}=f_{mid}+amount/2) and also the sweep duration (given by the video time) is known, the time dependence can be converted to a frequency dependence by:

$$f = \frac{(f_{end} - f_{start}) * t}{t_{max}} \tag{3.2}$$

where f_{start} and f_{end} are the start and end frequencies of the sweep, t_{max} is the sweep duration, t is the time and f is the corresponding excitation frequency.

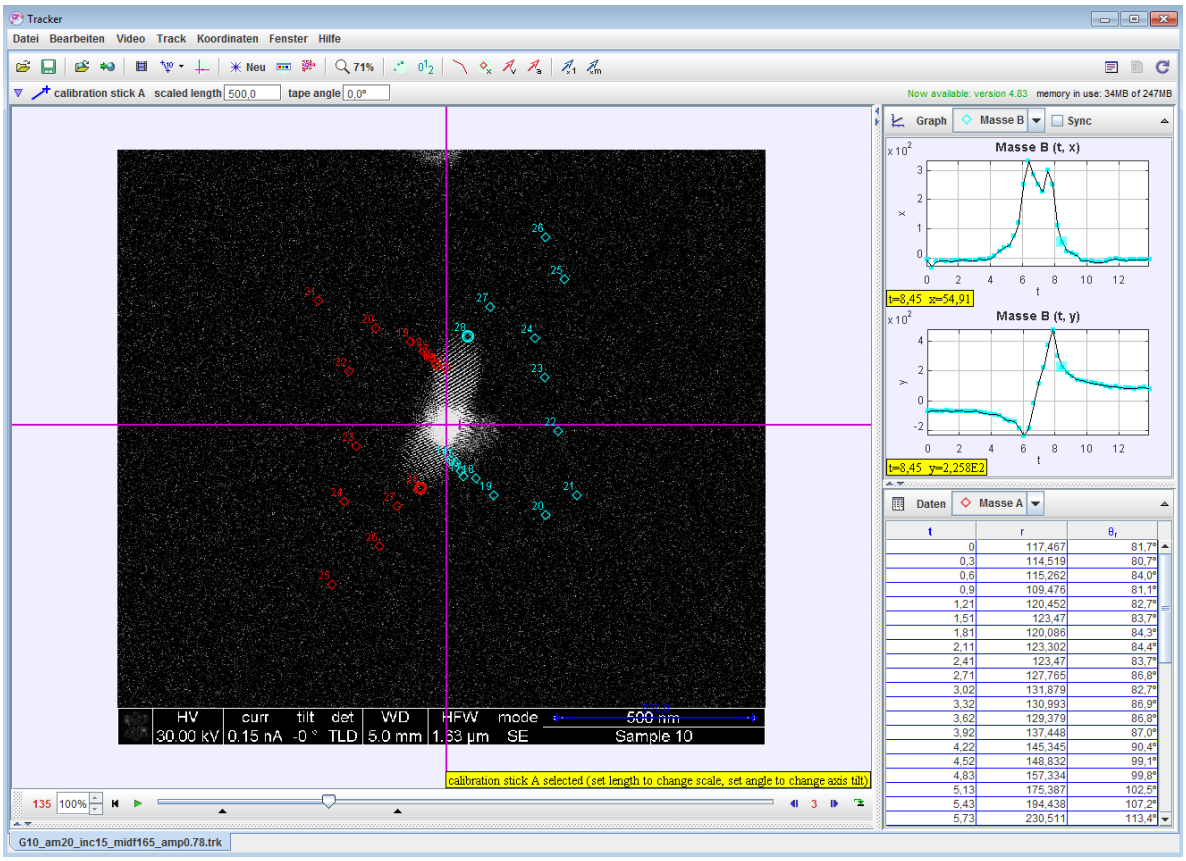

Figure 3-14: Tracker software for determining resonance frequencies and resonance curve acquisition.

3.4 Simulations to derive the Young's modulus E

The idea was to determine the Young's modulus from the electrostatic deflection experiments. Therefore, the force acting on the pillar has to be determined. Like already explained the calculation of the problem cannot be done analytically. Therefore, the finite element method based software *Comsol* in combination with *Matlab* was used.

When a direct voltage is applied between pillar and a deflecting electrode a force acts on the pillar that leads to a bending in the direction of the electrode. On the other hand, there acts a counteracting force on the pillar that is determined by the spring constant which is related to the Young's modulus. This is schematically shown in Figure 3-15.

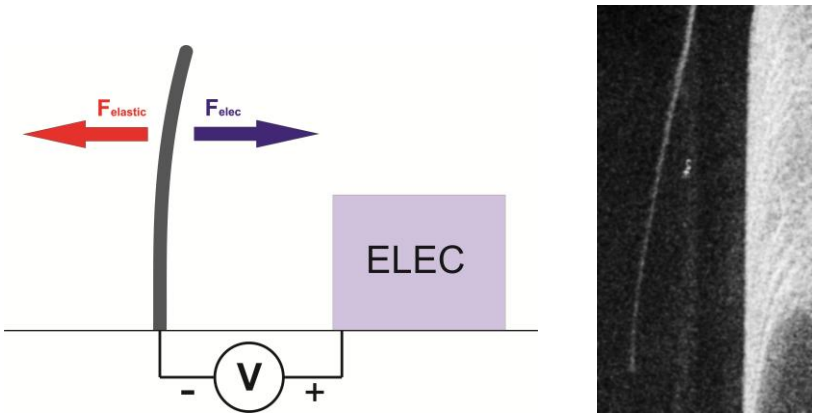

Figure 3-15: Forces acting on a pillar when a static electric field is applied between pillar and deflecting electrode. The SEM image at the right shows the nanopillar (Ø ~60 nm) which is bended towards the electrode on the right side.

Hence, the amount of maximum deflection is given by equilibrium of the two forces. So if vice versa the voltage difference and the deflection of the pillar is given, which can be accessed by the experiment, the electric force acting on the pillar can be calculated and thus also the restoring elastic force which is proportional to the Young's modulus. The actual simulation is done in four steps:

1. Creation of the geometry for the deflecting electrode
2. Creation of the geometry for the deformed pillar in equilibrium
3. Calculation of the force that acts on the deformed pillar along the Z-axis when a voltage is applied between pillar and electrode
4. Calculation of the Young's modulus which leads to the observed deflection under the calculated force

To combine these steps and also for easier handling, a graphical user interface was created in Matlab which is shown in Figure 3-16. In the following the GUI functions and also the detailed calculation steps are described more closely. The default values for the mesh sizes which correspond to the number of data points that are used for the simulation give good results. Care has to be taken when they are changed for different sets of experiments and simulations.

3.4.1 Creation of the electrode geometry

COMSOL is optimized for electrodes shown in Figure 3-17 (left). The fabrication of such electrodes is discussed in chapter 4.2.2.2. The pad at the back side of the electrode is used as contact for the Omniprobe micromanipulator. Since the dimensions of the electrode structures can vary they can be adjusted in the section (3) of the GUI (see Figure 3-16). In Figure 3-17 (right) a schematic view of the electrode structure is given. The designations of all the necessary dimensions used in the GUI can be seen here, which can be determined from SEM images of the electrode structure. When all values are set correct, the electrode geometry is automatically generated prior to the force calculations. An example for the generated geometry is shown in Figure 3-18.

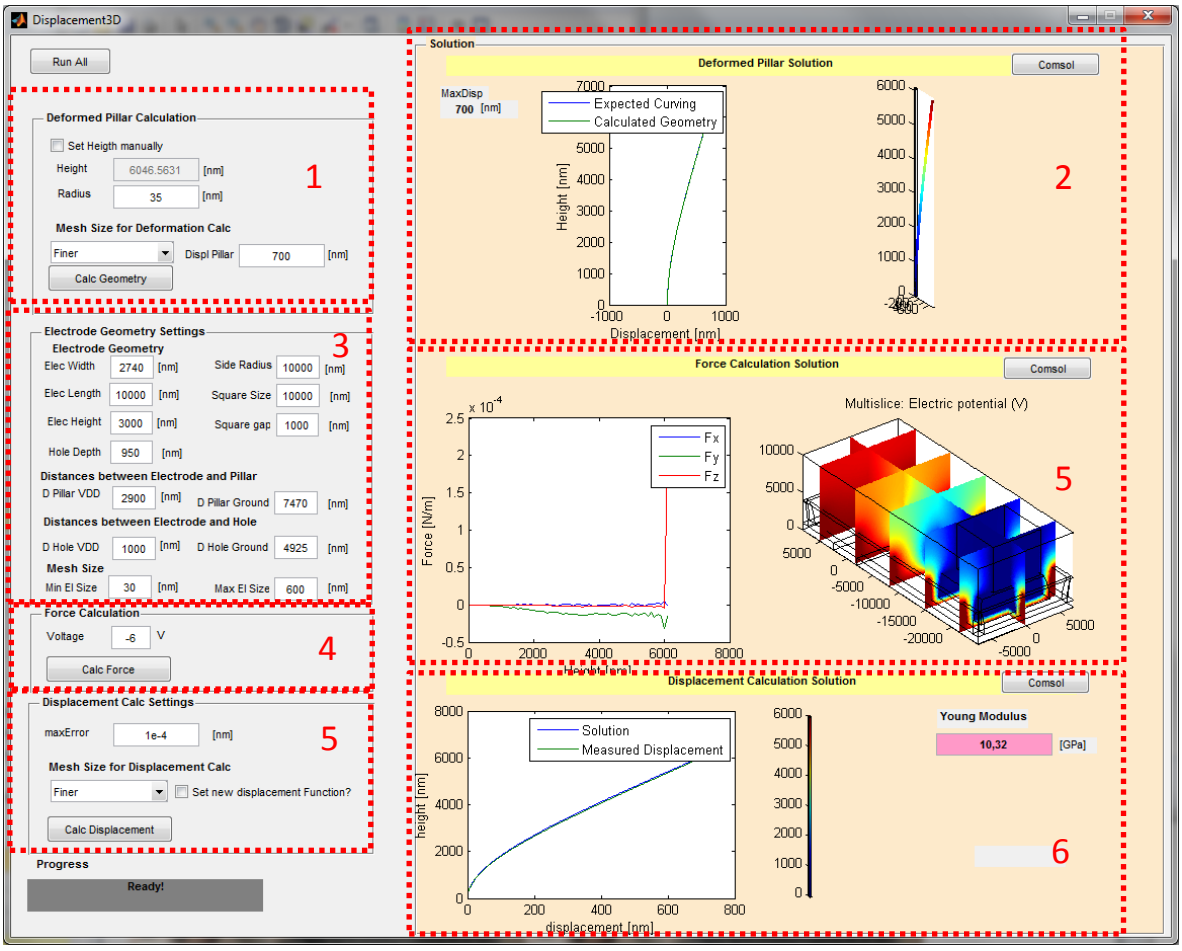

Figure 3-16: GUI for Young's modulus calculation

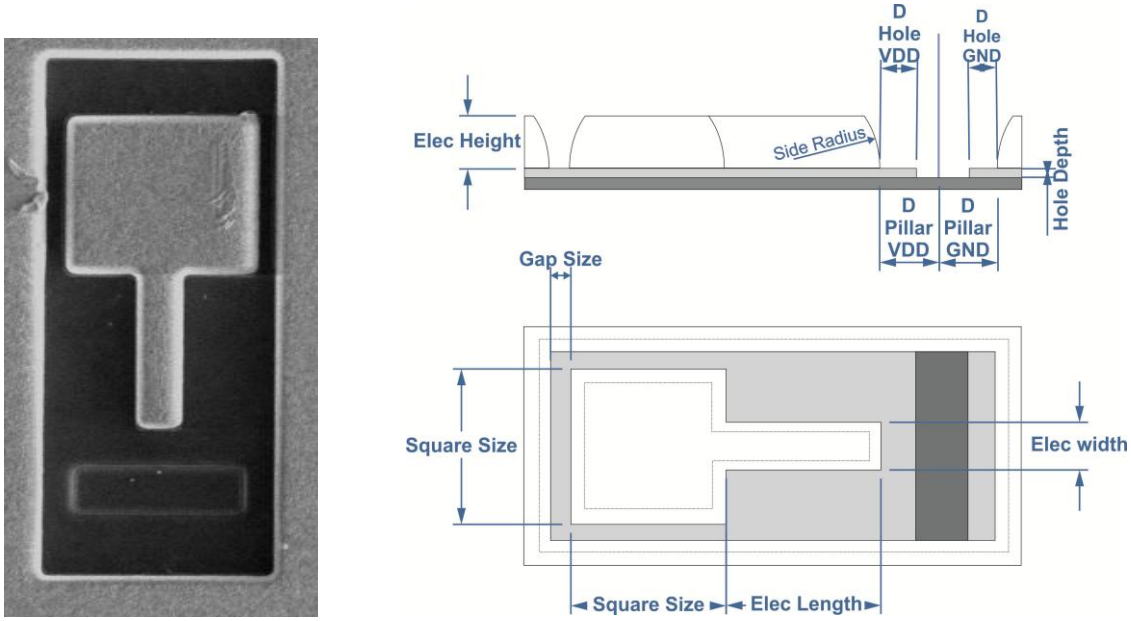

Figure 3-17: SEM image of the test structures used for the calculation of the Young's modulus in top-view(left); schematic representation of the test structures in side and top view with designations of the dimensions used in the GUI (right).

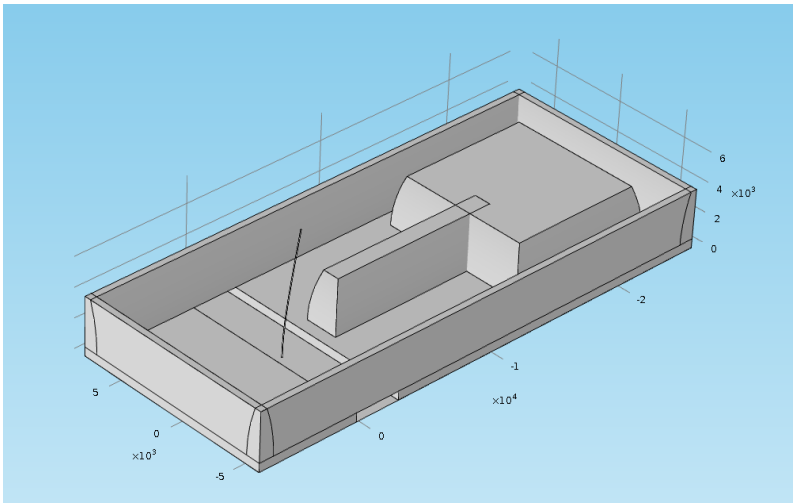

Figure 3-18: Electrode geometry generated in COMSOL

3.4.2 Creation of the deformed pillar geometry

To determine the deflection of the pillars along the z axis (***d(z)***), SEM images in side view were made during electrostatic deflection like shown in Figure 3-15 at the right where the bending of the pillar towards the deflecting electrode caused by an applied electric field is shown. ***d(z)*** can be derived from the image for a fixed deflection voltage. If other voltages and / or distances of the pillar from the deflecting electrode are used the deflection curve also changes. This is a problem as normally just the maximum deflections are measured from top view. One opportunity to approximate the new curve is by up scaling the above defined deflection-function by an appropriate constant factor so that the calculated maximal deflection corresponds to the measured one. This is done automatically by the program. The deflection function can be changed by copying a table of data points that determine a new displacement curve to the file "*DisplacementFunction.txt*" which is located in the same folder than the program file. In the GUI the settings for the creation of the deformed mesh are located in section (1) (see Figure 3-16). The value for the pillar height can be either be set automatically where the maximum height defined in the "DisplacementFunction.txt" file is used or it can be set manually by checking the "*Set Height manually*" box and adjusting the corresponding value. In the field below the radius of the pillar can be set (=width/2!). The value for the maximum deflection (deflection of the pillar tip) can be set under "*Displ Pillar*". When the "*Calc Geometry*" button is pressed, the data is passed to COMSOL, where vertices, edges and faces for the deformed geometry are calculated. In section (2) the result is shown. In the left graph the pre-defined deflection curve ***d(z)*** (blue) is compared to the curvature of the simulated deformed pillar. The right graph shows a 3D plot of the deformed geometry.

3.4.3 Force Calculation

Before the force acting on the pillar can be calculated the voltage applied to the deflecting electrode has to be set in the field "*Voltage*" in section (4) (see Figure 3-16). All the other parts of the geometry, including the bulk and the counter electrode are grounded by default. After pressing the button "*Calc Force*" all the parameters are taken over to COMSOL the geometry for the electrode structure is generated and put together with the deformed pillar geometry. Afterwards, the electrical

force acting on the pillar along the Z-axis is calculated for all three room directions (***$F_x(z)$, $F_y(z)$, $F_z(z)$***). An example for the voltage potential behavior in the Y/Z - plane and the three force curves derived from the simulations are shown in Figure 3-19. These two results also can be seen in section (5) of the GUI (see Figure 3-16). As can be seen, the force in X-direction is nearly 0 for all Z-values. This is expected since the forces parallel to the electrode should cancel out each other. The noise comes from inaccuracies in the simulation. Also the Z component is zero except at the tip of the pillar. Thus mainly the y component of the force is responsible for the deflection.

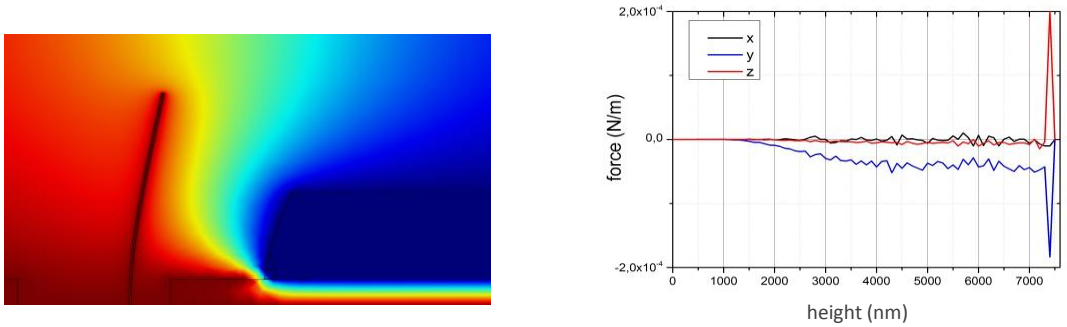

Figure 3-19: Potential course in the Y/Z plane (right); Electric forces acting on the pillar in dependence of the z-axis

3.4.4 Determination of the Young's modulus

By combining equations (2.3) and (2.4) following equation for the Young's Modulus can be derived for pillars:

$$E = \frac{64}{3\pi}\frac{h^3}{w^4}\frac{F}{d_{max}} \tag{3.3}$$

h and ***w*** are the geometrical parameters that describe the height and diameter of the pillar, ***F*** describes the force acting on the pillar and d_{max} is the maximum displacement in equilibrium. The equation clarifies that all the needed parameters for the calculation of ***E*** are given, but it is only valid if the whole force acts on the tip of the pillar. Since in our case the deflecting force is a function of the Z-axis also this problem is solved numerically in COMSOL.

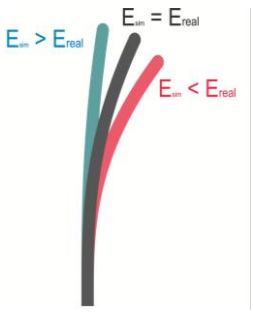

Figure 3-20: Different possibilities of finding the E-modulus.

As starting point an arbitrary value for ***E*** is chosen as material parameter of the pillar. Then the calculated force is applied to the undeformed pillar and the displacement for the chosen ***E*** is simulated. If the calculated displacement is too small ***E*** has to be increased, if it is too high ***E*** has to be decreased. The correct value for E is reached when the simulated deflection corresponds to the calculated one as schematically shown in Figure 3-20. The settings for the Young's modulus calculation can be adjusted in section (5) of the COMSOL GUI. In the field "*max Error*" the maximal deviation of the simulated and the measured value for the maximal deflection can be set. When the check box "*Set new Displacement Function*" is ticked the calculated displacement curve is taken as new displacement function which is used for the creation of the deformed pillar geometry. This can be useful to improve the accuracy of the calculated Young's modulus by performing several iterations. In the graph in section (6) (see Figure 3-16) the deformation of the pillar given by the simulated ***E*** compared to the expected deformation defined in the "*DeformationFunction.txt*" file. In the field "*Young's Modulus*" the value of the calculated Young's modulus can be found.

4 Measurement

4.1 Growth experiments

As described in chapter 2.1 the growth rate for FEBID deposits depends on a number of parameters, like the primary electron energy, beam current, GIS arrangement, molecular gas flux, focus conditions, dwell times, refresh times, substrate properties and deposit geometry. Actually, everything depends on the precursor regime describing the local coverage degree compared to available electron species. One way to keep precursor regimes in similar conditions is to either choose MTL conditions (strongly depleted) or RRL conditions (lack of dissociating electrons). As the first regime is complicated for high aspect ratios due to directional gas flux effects [9] we chose RRL like conditions by using very low beam currents to establish at least similar conditions during deposition.

As a key fact for electrostatic measurements described later, it is essential to fabricate structures with well-defined and comparable heights. For a growth rate estimation a set of experiments was performed as will be described in the following.

4.1.1 Focus and stigmator settings

If the spot of the electron beam is slightly defocused or stigmatic, significant volume growth rate (VGR) variations and pillar broadening can be the consequence. Thus, good focus and stigmator settings are essential for reproducibility of the deposits. To demonstrate the height dependency of the deposits on the focus settings several pillars were deposited via on-spot mode (stationary beam) with a total exposure time of 25 seconds while the defocus was systematically varied via the beam blur setting of the pattern.

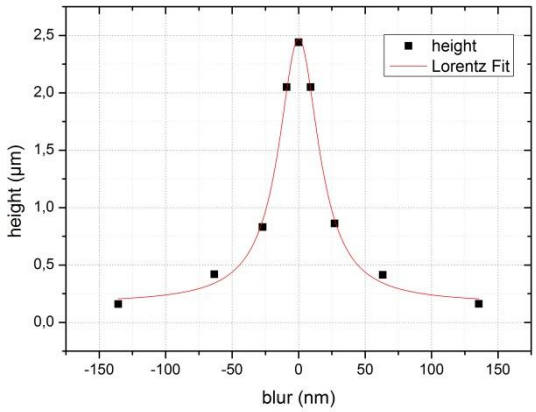

Figure 4-1: Height dependency on the beam defocus

As can be seen in Figure 4-1 the defocus (beam blur) dependency of the height follows a Lorentz function and shows massive variations even for small defocus values. Stigmatic beam conditions on the other hand can considerably deform the pillar cross section from round to strongly elliptic which can be seen in Figure 4-2 where three test points (very short pillars) were deposited with different stigmator settings.

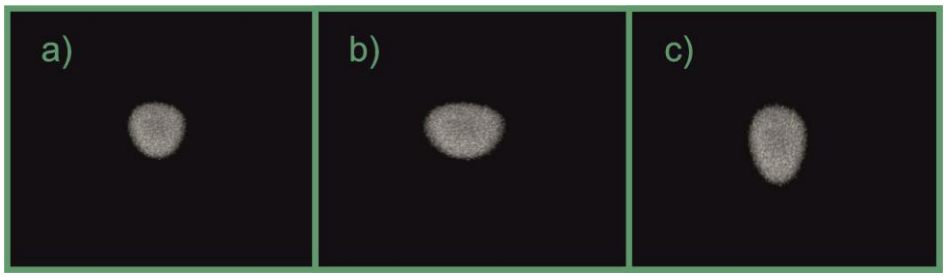

Figure 4-2: SEM images of test points deposited with sitgmatic beam settings (a) and astigmatic beam settings in horizontal direction (b) and vertical direction (c). The astigmatic beam settings lead to an elliptical shape of the test points and thus also of the pillar

It can clearly be seen that astigmatic beam settings lead to an elliptic pillar shape.

As lowest beam currents have been used, it is partly complicated to achieve comparable focus settings due the very low intensities during focusing. A good focus manifests itself in good image resolution, which is subjective and varies a little bit from user to user and from session to session. To achieve comparable focus conditions a strategy was developed which is described below.

4.1.2 Focusing strategy

It turned out that ETD and TLD detector signals doesn't give the same focus point which is caused by the additional voltage in the column pole piece when using the TLD. Nevertheless, best result are achieved for using the TLD detector during focusing. At first the settings for crossover, lens alignment, focus and stigmator has to be adjusted as usual until a good resolution is achieved. In the next step, a small Pt single point is deposited. This test point can be used for a verification of the actual quality of the focus settings and also as reference points for a further fine alignment process. A not perfectly round test point comes from an astigmatic electron beam. Furthermore the diameter

of the test point can be measured and conclusions about the quality of the focus can be drawn. Best focus and stigmator settings are archived when the diameter of the point is minimized. It is also possible to play around with the stigmator settings to build slightly stigmatic pillars with intent to define the resonance directions like explained later. A minimal diameter depends on the electron beam current and also on the substrate. Typical values lie between 60 nm and 70 nm but can go down to 50 nm for perfect settings and high gas fluxes.

4.1.3 Quasi - 1D pillars

Although the deposit is about 60 nm in diameter, we denote the pillars as quasi-1D structures as the pillar heights are typically in the 3 – 8 µm range. In the following we describe reproducibility and parameter dependency as main information towards reproducible quasi-1D pillars.

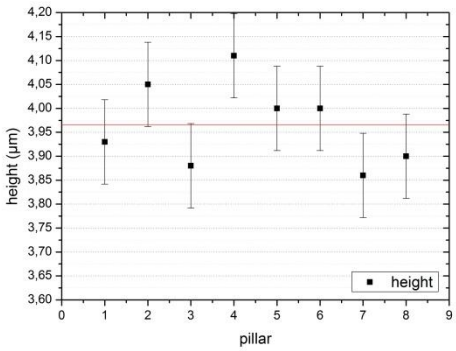

Figure 4-3: Height reproducibility experiments

4.1.3.1 Reproducibility

In a first experiment a height reproducibility test was tested. 8 pillars were deposited in the on-spot mode by readjusting the focus for each pillars via the test-point method described above. The same total exposure time (**TET**) of 147s was used for each pillar. Electron energy and beam current were set to 5 keV and 25 pA, respectively. As shown in Figure 4-3, despite good focus settings height variations occurred. A value of 88 nm was calculated for the standard derivation for a mean height of 3.97 µm which corresponds to a variation of 2.2 % of the pillar height. Additional tests revealed that the mentioned variations of about 2 % cannot be further minimized which is explained by fluctuations of the precursor density at the point of electron interaction and also by small focus variations beyond recognition during the focusing procedure.

Furthermore, the observation with the electron beam can lead to a slightly bending of the structure and thus to an apparent shortening of the pillar which an essential detail. To minimize height variations it also is important that the sample surface is located exactly at the eucentric height during deposition to omit distance variations between surface and GIS needle. For the experiments only structures deposited with 5pA and 25pA electron current were used. The use of higher currents leads to unpredictable outgrowth along the pillar, especially in the bottom region and also to large height variations which can be seen in Figure 4-4 where a pillar deposited with 98pA e-beam current is shown.

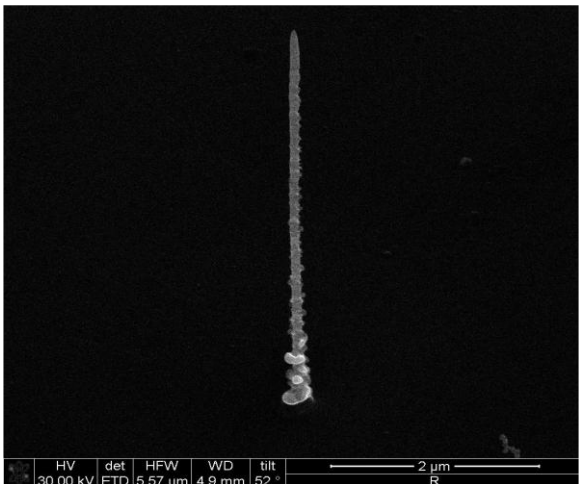

Figure 4-4: Pillar deposited with 98pA electron current and 5kV acceleration voltage which demonstrates the non-optimal shape at higher electron currents

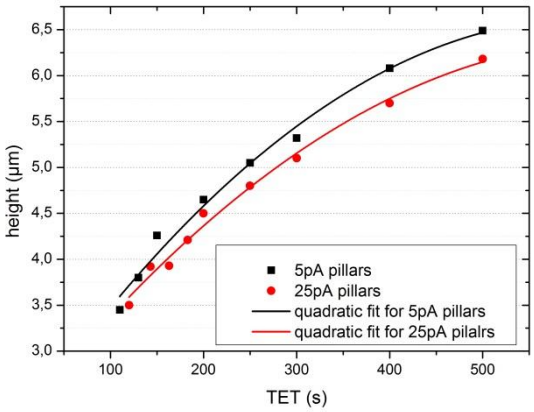

Figure 4-5: Pillar height fabricated at 5 keV and 5 pA (black) and 25 pA (right) as a function of the total exposure time using spot mode deposition.

The height as a function of the total exposure time for pillars deposited in the on-spot mode with 5 pA and 25 pA electron current shown in Figure 4-5. It can be approximated by a second order polynomial fit. Like shown in the figure the pillars deposited with 5 pA beam current are slightly higher than the pillars deposited with 25 pA beam current. The nonlinear behavior reflects the decreasing molecule coverage at the end of the tip where new deposition takes place triggered by an increasingly complicated situation for surface diffusion due to the narrow pathway for random molecule motion. It has to be mentioned that the height dependency of the TET, and hence also the growth rate, differs for every GIS system. It depends on the used precursor, the gas pressure and gas flux, the input angle of the GIS needle, on the geometry of the needle the specimen etc. The shown curves were determined for the “Working GIS” of the used dual beam system. They have to be determined for every GIS system separately and also may vary slightly with time when the gas pressure falls because the reservoir gets empty. Keeping this in mind it can be necessary to make little adjustments to the calculated total exposure time to derive the desired pillar height.

4.1.3.2 Refresh time

In the next step a refresh time was additionally introduced to enhance the surface coverage at the pillar tip. This was done by blanking the beam after the defined dwell time, which allows a replenishment of the precursor molecules. A refresh time of 0 corresponds to the on-spot mode. In an experiment several pillars were produced with an e-beam current of 25 pA a constant dwell time of 100 µs and a total exposure time of 52 s. The refresh time was varied. The height dependency of the refresh time and of the total pillar production time (refresh time + dwell time) is shown in Figure 4-6. The data points are interpolated by cubic splines. These curves were only valid for the used "Working GIS" system and only for a DT of 100µs. Nevertheless, it can be seen that the growth rate can be improved by choosing the correct RT values. Together with the fact that higher currents lead to lower vertical growth rates (see Figure 4-5) we can state that although working in a more RRL like regime we are still far away from real RRL conditions which should result in totally constant heights in Figure 4-6. However, due to drift issues for extremely high refresh times it is not practicable to use such conditions why we decided to do all investigations at lowest beam currents of 5 pA (at 5 keV) to establish RRL like conditions with comparable pillar properties for different experiments (only about 2 % standard deviation).

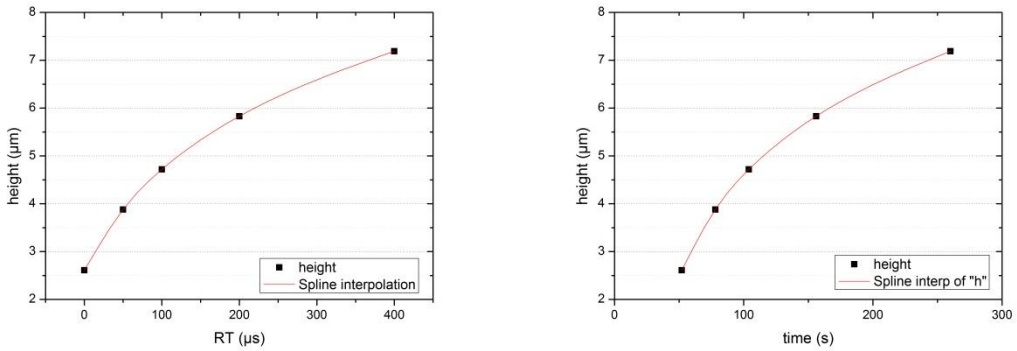

Figure 4-6: Height dependency of the refresh time (right), height dependency of the total production time (left)

4.1.4 Quasi 2D

As done for the quasi-1D pillars we denote a sidewise stack of pillars as quasi-2D structures (referring to a top view) as we wanted to introduce another dimension and compare the results with quasi-1D structures but more importantly to theoretical considerations as described in detail later.

4.1.4.1 Point Pitch

In a series of experiments the optimal point pitch was determined. The optimal point pitch was found with 60 nm for beam currents of 5 pA at a primary energy of 5 keV (see Figure 4-7b). If the value for the point pitch is too high, this leads to the deposition of separated pillars instead of a homogeneous pad (Figure 4-7a), if it is very low, this leads to a smooth surface but the production of the pads takes a too long time (Figure 4-7c).

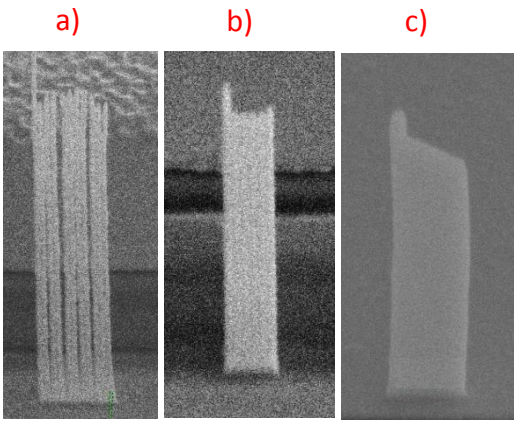

Figure 4-7: Pad structures; a) point pitch to large, b) optimal point pitch, c) very small point pitch

4.1.4.2 Total exposure time, dwell time and refresh time

In the case of quasi-2D pads the total exposure time specifies the exposure time for every point of the pattern. Thus the total production time for a pattern is given by the number of pattern points times the TET. To study the influence of the dwell time, test pads with different dwell times were produced. The beam current was set to 25 pA, the PoP to 60 nm and the length to 480 nm for all pads.

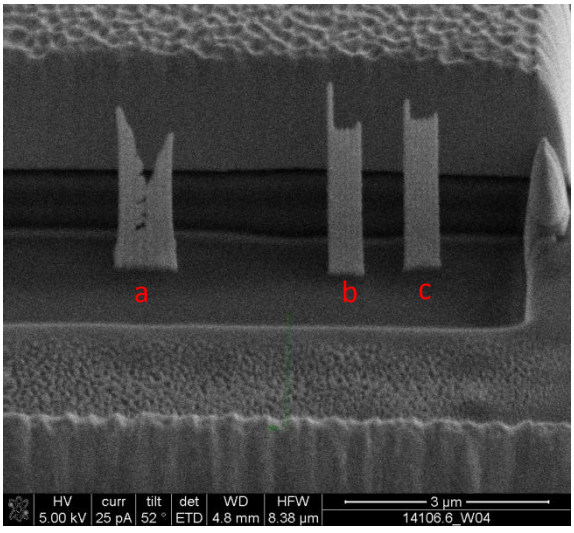

Figure 4-8: Pads deposited with a dwell time of a)10µs, b) 50µs, c) 100µs

In Figure 4-8 it can be seen that the 10 µs pad has no well-defined shape. This happens because the electron beam cannot be directed across the substrate surface in the desired speed. DT's of 50 µs (b) and 100 µs (c) seem to be large enough.

The minimum refresh time (**RT**) for the pads is given by:

$$RT = (n - 1) * DT \tag{4.1}$$

One can see that ***RT*** and dwell time ***DT*** are dependent variables and cannot be treated separately. The height dependency of the TET for pads produced with DT values of 50 µs and 100 µs which lead to RT's of 350 µs and 700 µs is shown in Figure 4-9. The data points were fitted with linear regression curves, crossing the zero point. From the slopes it can be calculated that the growth rate for the 100 µs pads is 1.4 times larger than the growth rate of 50 µs pads. This relation is only valid for 480nm long pads. Although expected differently, as higher dwell times should actually lead to lower growth rates due to stronger depletion, the results can easily be explained by the higher refresh time for the 100 µs DT experiments as the influence is very strong, demonstrated by the RT experiments for quasi-1D single pillars.

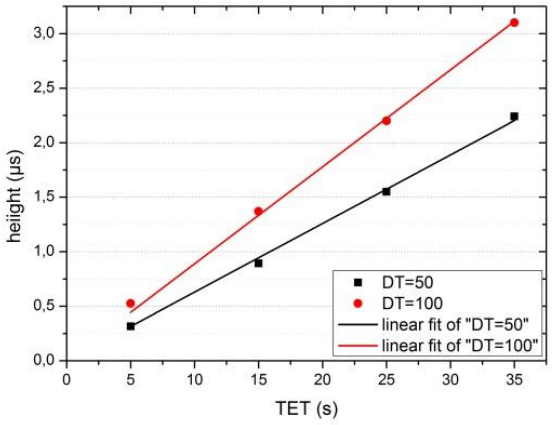

Figure 4-9: Height dependency of quasi-2D pads in dependency on the total exposure time TET for different dwell times as indicated.

4.1.4.3 Pad length

The height dependency of different pad lengths on the pad heights is shown in Figure 4-10 for a TET of 35 s, a PoP of 60 nm and a DT of 50 µs. Interestingly, there is kind of saturation behavior revealed which is caused by much higher refresh times leading to more constant coverage situation. In that case it can be concluded that at least the 1000 nm long quasi-2D pads are close to RRL conditions.

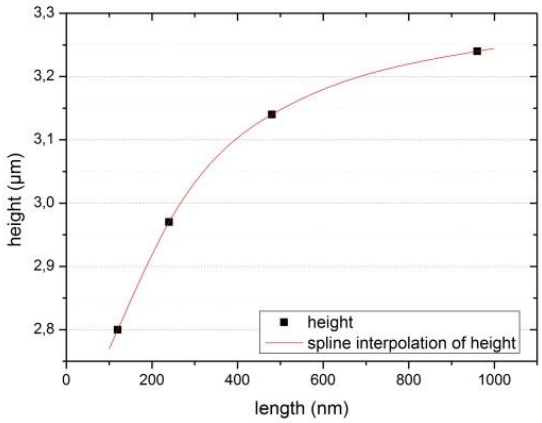

Figure 4-10: Height dependency of the pad length

4.2 Test geometries and pre-testing

Before the actual experiments could be started pre-tests has to be performed to prove if electrostatic deflection of the Pt-structures is even possible and to identify the best experimental conditions.

4.2.1 Omniprobe

4.2.1.1 First deflection tests

In a first experiment pillars with different parameters were deposited on a structured and grounded gold path. After tilting the stage to an angle of 52° which makes it possible to look at the pillars from the side, the Omniprobe tip was placed near the pillars and a voltage was applied. Like expected a bending of the pillars in direction of the tip occurred. The deformation of the pillar in dependence of the applied voltage and the distance ***d*** between the Omniprobe and the pillar was measured like shown in Figure 4-11. Placing the Omniprobe near a pillar was a bit trickier. At first the Omniprobe has to be inserted. Afterwards, the stage and thus the sample with the pillars has to be moved up manually using the manual Z-adjustment until the Omniprobe tip is close to the sample. A shadowing effect occurs just before the tip touches the surface. In the next step the stage has to be moved along the X/Y - plane until the desired pillar touches the Omniprobe tip. Then Y axis of the stage has to be adjusted until the desired distance between pillar and Omniprobe is achieved. The experiment demonstrated that the electrostatic deflection of the deposited structures was possible but the measured deflections were not reliably reproducible due to following problems:

- The images that were taken are just 2 dimensional projections. It cannot be identified if the Omniprobe tip is within one plane with the pillar or if it is slightly behind or in front of it. This leads to a bending of the pillars in different directions with an unknown angle.
- Just the front side of the Omniprobe tip can be seen in the image, no information about the rest of the geometry can be derived. The distance between Omniprobe and specimen surface differs from measurement to measurement.
- If the pillar tip touches the charged Omniprobe a current is flowing which leads to melting of the Pt-deposit. Parts of the deposit stick at the probe tip and contaminate it which leads to a change of the tip geometry and an associated change of the electrostatic force.
- The Omniprobe drifts slightly due to mechanical stress that acts on the external wires.
- There also is a superimposed stage drift.

To improve the reproducibility several changes were made to the measurement strategy:

- Instead of tilting the stage to 52°, the maximum deflection of the pillar can also be measured from top view. This allows better and easier aligning of the pillar plane with the Omniprobe tip.
- The Omniprobe should touch the isolating surface beneath the conductive gold path which improves the mechanical stability.

- Since distance between Omniprobe tip and substrate surface cannot be seen in the top view, the stage has to be moved up until the Omniprobe tip touches the surface. This is the case when a slightly bending of the Omniprobe can be noticed in the live image.
- The stage should not be moved anymore in x and y direction when the Omniprobe touches the sample, otherwise this can cause damage to the Omniprobe tip.

For further improvements the Omniprobe tip was shaped with the ion beam to achieve a well-defined geometry to eliminate unknown effects.

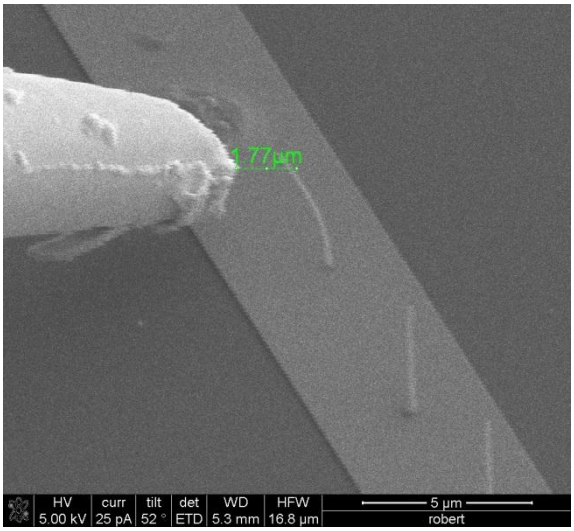

Figure 4-11: First deflection test with the Omniprobe micromanipulator.

4.2.1.2 Production of Omniprobe tip geometries

To produce the desired tip geometry the Omniprobe needle was extracted from the Omniprobe holder and mounted on the sample holder with adhesive carbon tape. The needle was aligned parallel to the stage. The goal was to produce a flat counter electrode for the deflection experiments like shown in Figure 4-12 a). Therefore the Omniprobe needle had to be shaped like shown in b).

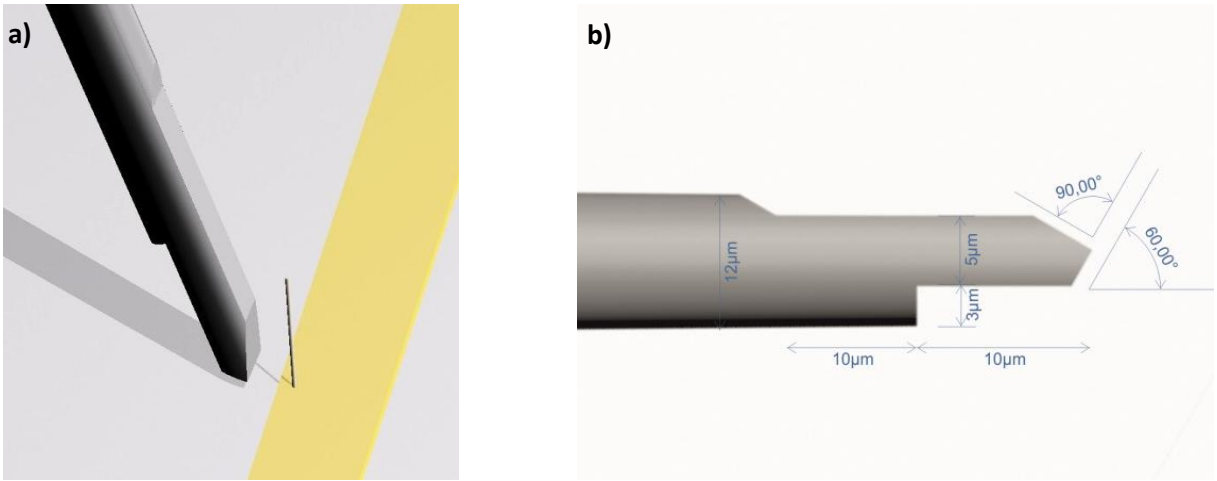

Figure 4-12: Measurement principle with shaped Omniprobe as counter electrode (left); shape of produced Omniprobe tip (right)

The Omniprobe tip was shaped with the ion beam in several steps. The rough profile was cut with the maximum ion current. Then the current was reduced step by step. Lower ion currents leads to sharp and clean surfaces but to an increase in production time. The images of the displacement measurements are shown below.

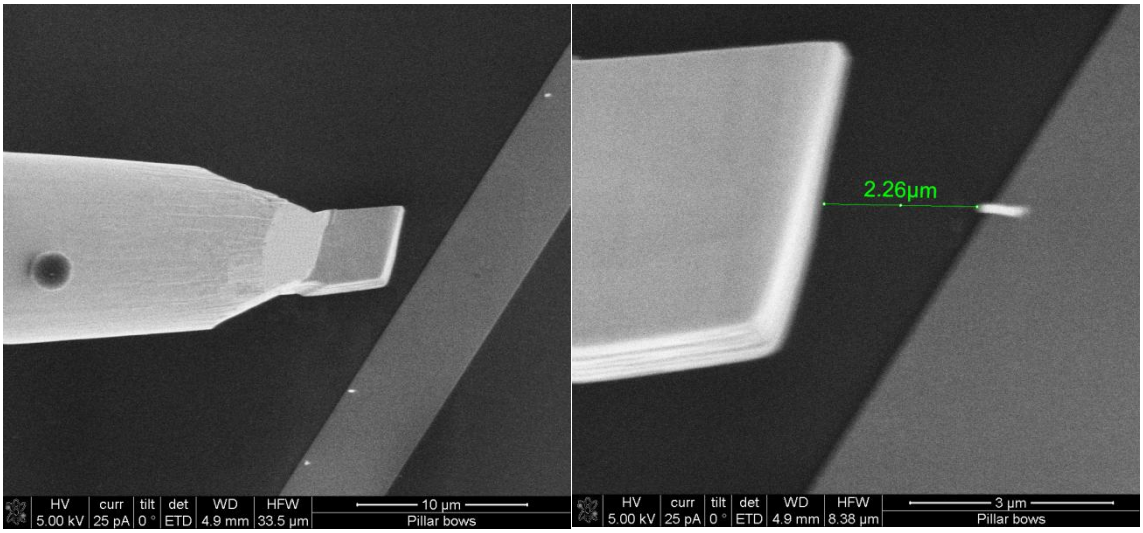

Figure 4-13: Deflection measurements with shaped Omniprobe

This measurement method provided much better results. Nevertheless, it was hard to achieve reproducible measurements. A problem of this method was that the angle of the pillar faced surface varied because the support pressure of the tip differed from measurement to measurement, which lead to a variable bending of the Omniprobe. Also the distance between pillar and Omniprobe was still varying due to forces acting on the external cables. Another essential problem was that the production of the Omniprobe tip takes quite a long time. Each time contamination occurred due to burn-out pillars occur the Omniprobe needle had to be extracted from the holder again and the above described procedure had to be repeated. Nevertheless, the shaped Omniprobe method was useful for some measurements, because the distance between structure and electrode can be varied during the measurement. It is also an advantage that several structures can be examined in succession by just displacing the tip to the desired place.

Finally, we decided to change the entire setup in order to minimize unwanted effects and eliminate unknown geometrical effects which will be discussed in the following chapter.

4.2.2 3D FIB structures

To omit the problems described above, a new type of test structures was developed that was produced by milling out test electrode geometries by FIB processing which then are conducted via the Omniprobe micromanipulator. In the following, the used layer sequences as well as the finally processed geometries are described in more detail.

4.2.2.1 Substrate preparation

The substrate material for the structuring was a Si waver with 500 nm SiO_2 on top. Then a 500 nm Cr layer was deposited followed by a 2500 nm Au layer as shown in Figure 4-14.

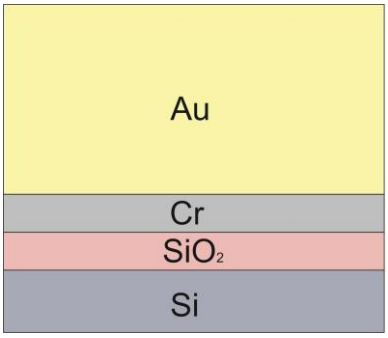

Figure 4-14: layer sequence of the finally used substrates further processed via FIB milling

The gold and chromium layers are conductive and form the counter electrode for the FEBID resonators. Au was chosen because it has a high sputter rate and thus the relatively thick layer of 2.5 µm can be produced in acceptable times. The Cr layer was introduced to improve the adhesion between gold and substrate. The Si waver material is weakly conductive and acts as base contact for the FEBID structures. The SiO_2 coating acts as isolation layer between electrode and base contact. The detailed sputter parameters are listed in the table below.

Table 4-1: Sputter parameters for the substrate production

Material	Cr	Au
Layer thickness	500	2500
Sputter rate	1.27Å/s	4 Å/s
Sputter time	20.8 min	125 min

4.2.2.2 FIB structuring

Like mentioned above the test electrode structures were produced via FIB processing. To define the shape of the test structures bitmap patterns were used. The optimal test structure for most of the experiments was determined in a series of pre-tests and is shown in Figure 4-15.

It consists of an electrode with a 10 x 10 µm square geometry and a rectangular feed through to the conductive Si bulk with the dimensions 10 x 2µm and a depth of approximately 1.5 µm. The structure was fabricated in two steps. At first, the test electrode is produced by sputtering the surrounding area down to the SiO_2 layer. It is important that the sputtering process is exactly stopped when reaching this layer, otherwise a short circuit between Si bulk and electrode can be caused by re-deposition of the conducting material. In the second step, the feed through to the conducting layer is produced by a rectangle pattern. The distance between the hole and the electrode should be at least 1 µm to omit short circuits between bulk and electrode. The sputter progress can be estimated either by using the iSPI mode from the microscopes user interface, which allows a life monitoring of the patterning progress, or by using the end-point monitor (**EPM**) which displays the current through the sample. The EPM signal and the associated SEM images are shown below. Every time a material

boundary is reached a kink occurs in the curve. By that, it can easily be detected when the SiO_2 layer is reached.

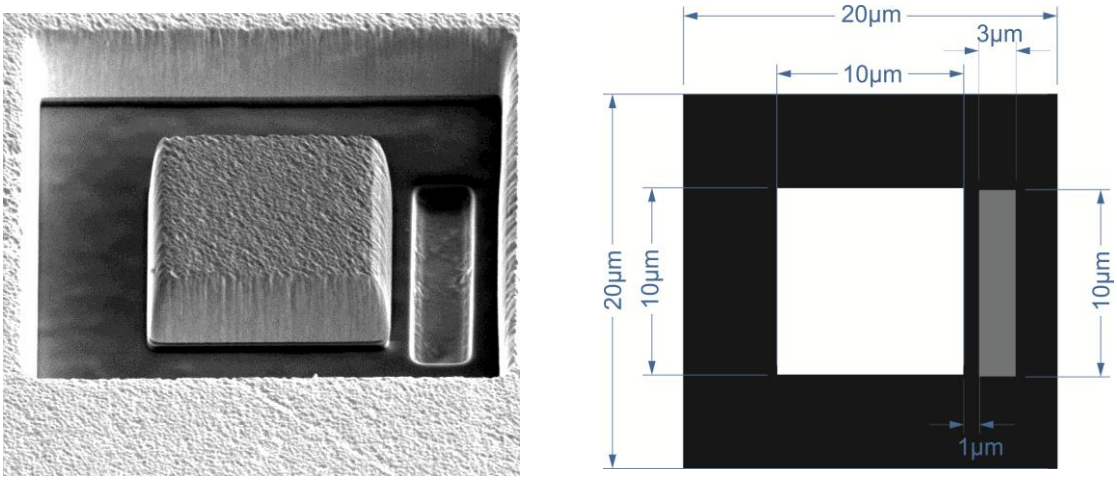

Figure 4-15: ideal test structure (left); used pattern including the finally used dimensions (right)

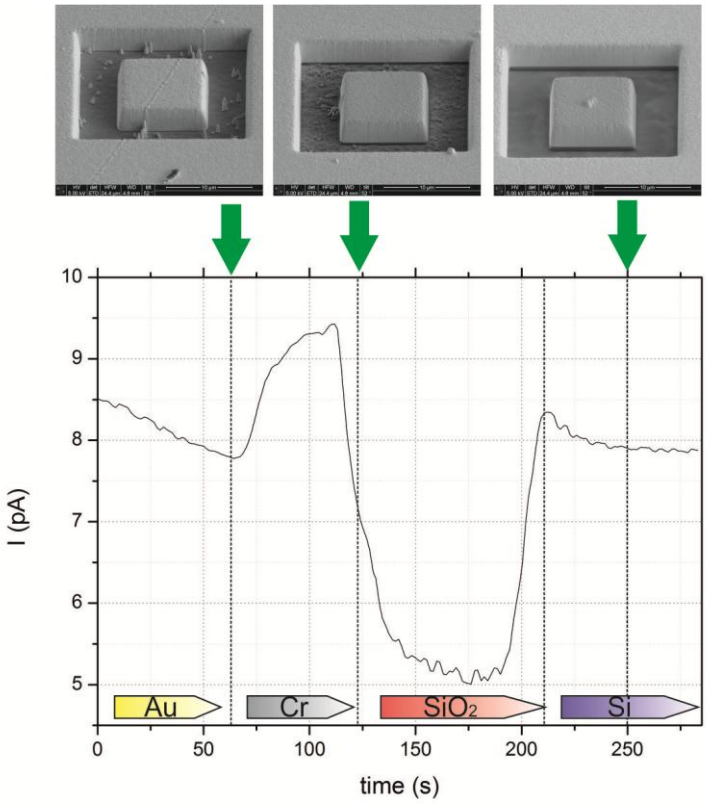

Figure 4-16: EPM signal during milling process and corresponding SEM images

The lateral electrode dimensions were chosen as small as possible to minimize the production time but also large enough to provide an easy way for the contacting with the Omniprobe. Too small electrode structures poorly adhere on the substrate and it may happen that they are displaced or detached from the substrate during the conduction with the Omniprobe. The production time of the test structure depends strongly on the used ion beam current. Typically, 5 nA have been used which

led to a production time of about 5 minutes per structure. Lower currents led to smoother surfaces and sharper edges which is highly desirable. To save time it was tried to reshape the just front electrode face in a second production step by sputtering with lower ion current, however this didn't work because the SiO_2 layer in the surrounding area was also damaged and a short circuit between the electrode and the Si substrate occurred. If a smoother electrode shape is required the whole structure has to be produced with a lower current at once. Arrays of test structures were produced like shown in Figure 4-17 which make it possible to perform several measurements consecutively. To perform the final experiments, the Si substrate has to be grounded while the electrode has to be conducted via the Omniprobe.

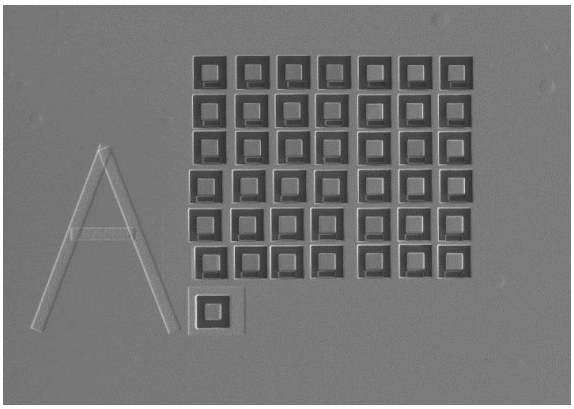

Figure 4-17: Array of test structures

4.2.3 Etched test structures

For further experiments with FEBID resonators professional test structures were produced by the Oak Ridge National Labs in Tennessee around Prof. Philip D. Rack. The substrate material consists of a highly doped, conducting Si with a 3 µm thick insulating layer and a 500nm thick metal layer on top. The test structures were produced by etching. To increase the height of the metal electrode the Si substrate was underetched on purpose. Due to the manufacturing process the amount of underetching varies from the middle of the sample to the corner. Again the Si-waver is used for contacting the FEBID structures. The metal layer acts as deflecting electrode. The layer setup and the etch steps are schematically shown in Figure 4-18 and can also be identified from the SEM image of the test structures which is shown in Figure 4-20.

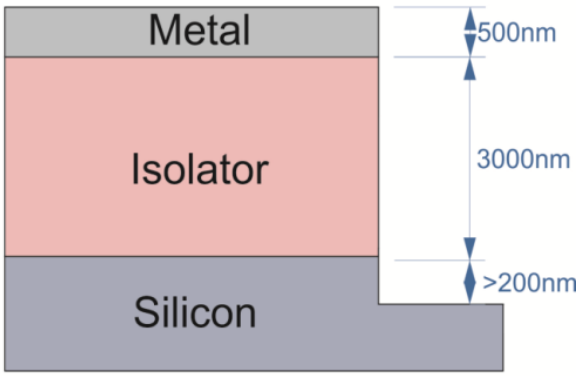

Figure 4-18: Layer composition of the test structures (left);

There are 4 different electrode layouts on the substrate like shown in Figure 4-19:

1. **Type A**: 4 electrodes (2x flat end, 2x sharp end)
2. **Type AR**: 4 electrodes but rotated 90 °
3. **Type B**: 2 electrodes with flat ends
4. **Type C**: 2 electrodes with sharp ends

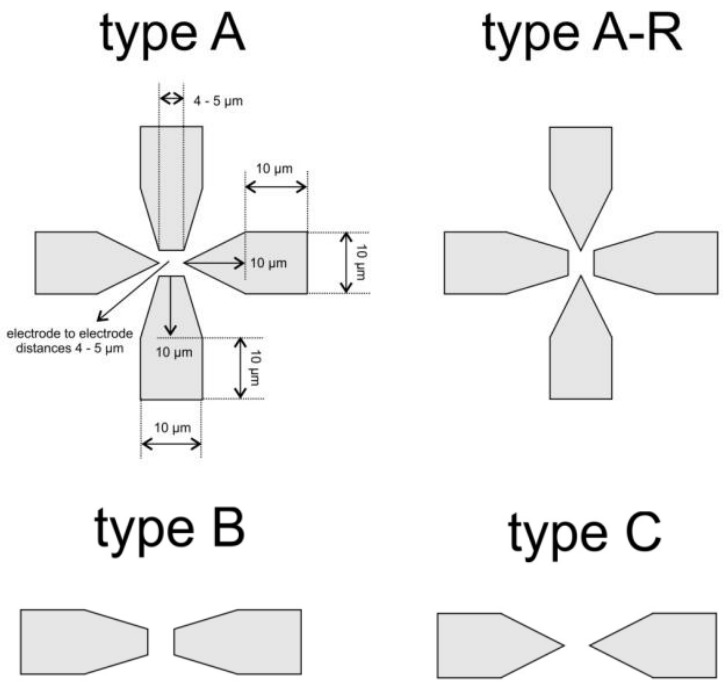

Figure 4-19: Electrode geometries on etched test structure including their lateral dimensions

The distance between the opposite electrodes is always 4 µm. The FEBID nanopillars are deposited in between. There are 10 x 10 µm sized contact pads at the back side of each electrode for easy conduction with the Omniprobe tip. The electrode patterns are arranged on the substrate like shown in Figure 4-21. The substrate size is 25 x 12 mm.

It is also possible to contact some of the structures directly without Omniprobe with the active stage holder as described in detail in references [17]. Therefore, some of the type **A** and type **AR** structures are connected to lines that lead to the large contact pads like shown in Figure 4-21. A SEM image of the conducted structures is shown in Figure 4-20. Type **A** gives contact to the triangles and type **AR** contacts the flat electrodes. There are located mixed arrays with patterns of type **A, B** and **C** between the lines.

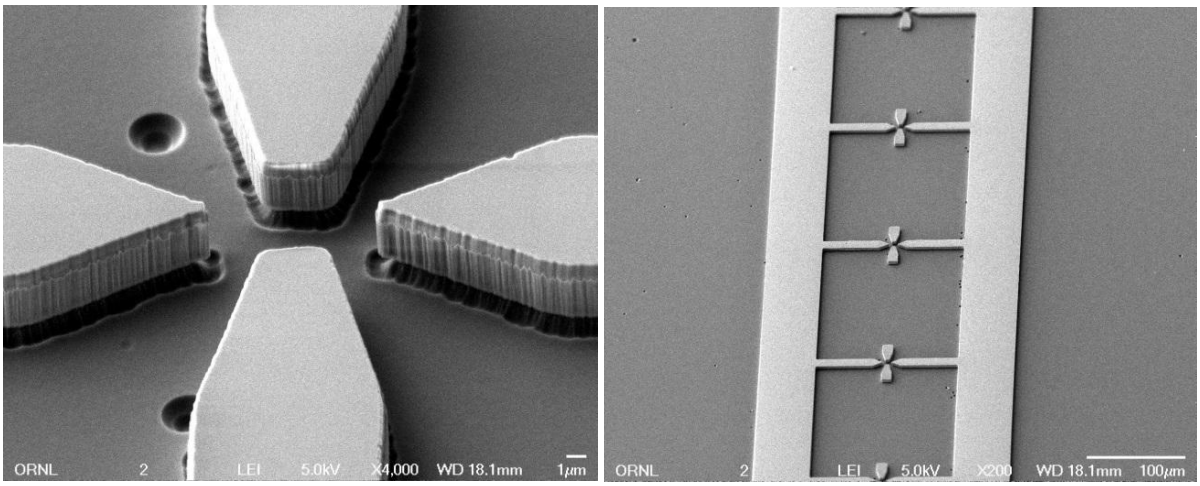

Figure 4-20: SEM images of a Type A test structure (left); Array of Type A structures (right). The two opposite electrodes are connected via metal lines to large pads which can be used to contact the test structure with the active stage holder

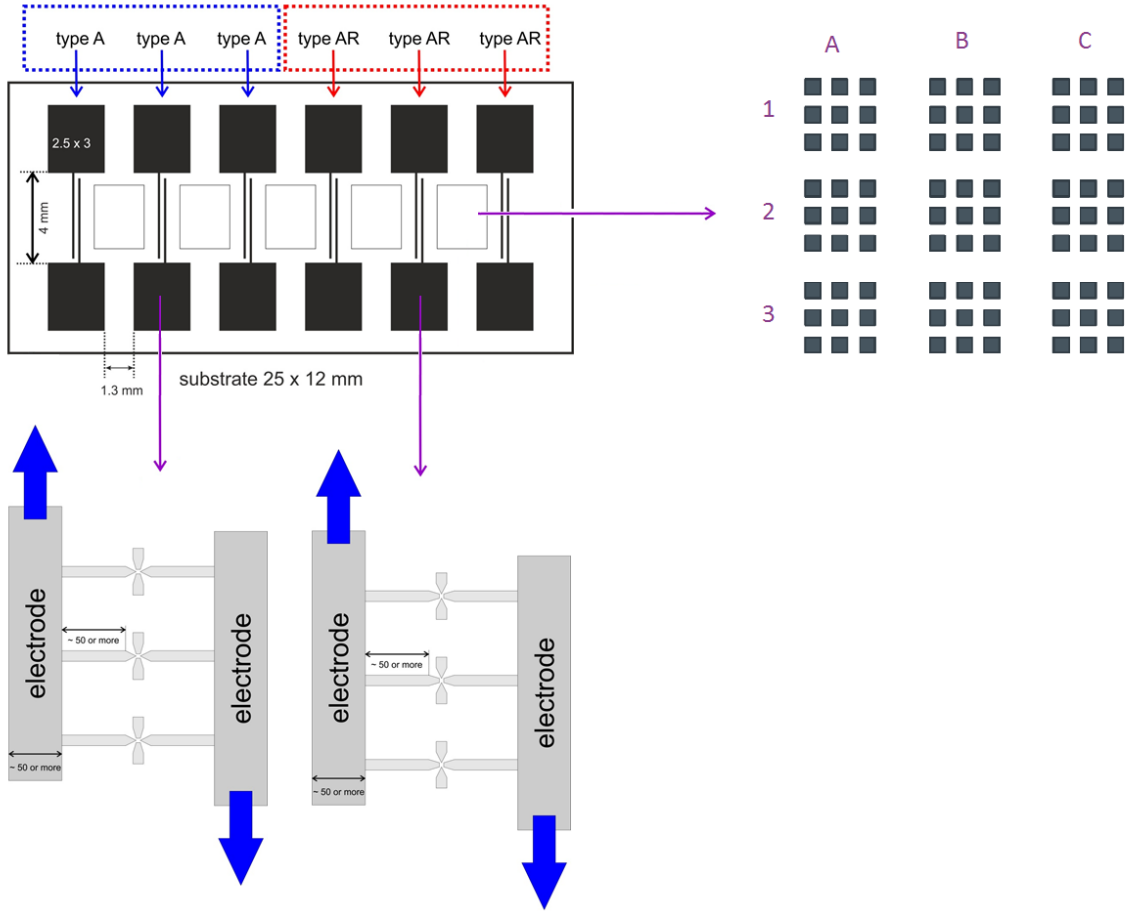

Figure 4-21: Sample Layout and electrode structures

4.2.4 Optimal SEM settings for in-situ characterization

Bending and resonance measurements were done by imaging the deflected structures with the SEM in normal and tilted arrangements depending on the intended purpose. The additional electric fields due to the potential on the electrode and Omniprobe lead to noise and distortion in the image. Another problem is that the electrons interact with the deposited material which leads to changes of the material properties due to modifications of the chemical structure. These effects can be minimized by choosing the correct observation parameters. A high acceleration voltage of 30 kV was chosen since high energy electrons are less deflected by the additional electric fields. High energy electrons also have the advantage of a smaller interaction cross section and don't cause very much damage to the FEBID material during observation. The measurements are furthermore most accurate when using low electron current. For the observation the TLD detector was used since it provided the best contrast. Further improvements of the image quality can be achieved by providing a ground connection between the voltage source and the microscope. This is especially important for the electrostatic deflection tests.

4.3 Electrostatic displacement experiments

4.3.1 Bending experiments

To observe which deflection voltages, deposit dimensions and distances to the deflection electrode are generally needed a set of bending experiments was performed. Figure 4-22 shows the maximum deflection for different pads in dependence of the applied deflection voltage at the electrodes. All quasi-2D pads used for this type of deflection experiments were deposited with a primary energy of 5 keV, 5 pA beam current, 60 nm point pitch PoP and a dwell time DT of 50 µs. It was tried to achieve a constant height of 4.6 µm for all pillars to provide comparability.

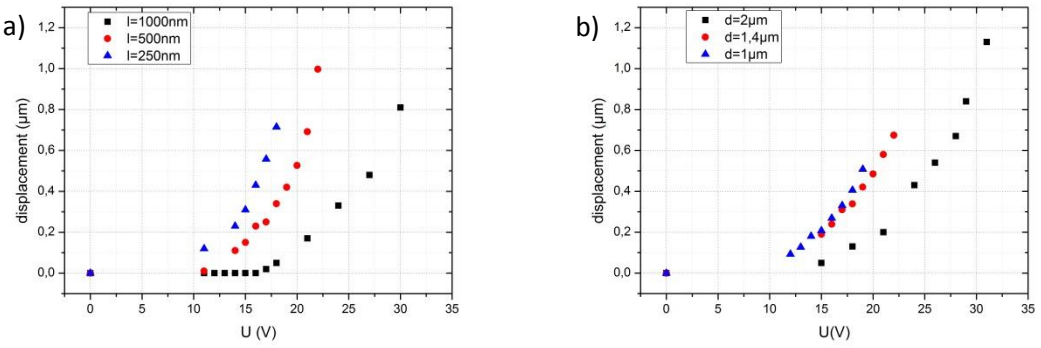

Figure 4-22: deflection in dependence of the electrode voltage for FEBID pads with different lengths (a) and for different distances from the deflection electrode (b)

Figure 4-22 (a) shows the deflection maximum of the quasi-2D pads with different lengths but with constant distance to the electrode (1,5 µm). In Figure 4-22 (b) the deflection for quasi-2D pads with different distances from the electrode but a constant lengths of 480 nm are shown. Since the deflections are dependent on a large number of parameters and also the force that acts on the pillar changes with changing deflections only qualitative statements can be made from the deflection measurements which are summarized below:

- For our experiments the *height for pillars and pads* should be *at least 4 µm*. Otherwise, the deflection is not large enough for appropriate measurements.
- The higher the FEBID structure the larger the deflection for a constant electrode voltage.
- The larger the distance to the electrode the smaller the deflection becomes which corresponds to the smaller electric force acting on the deposit. The *optimal distance to the electrodes* was determined to be in a range *between 1.5 µm and 3.5 µm*. If the structures are too far away, the required voltage for the desired deflection becomes too high, if they are too near, little changes in the voltage lead to a dramatically change in the deflection and it's hard to find the correct voltage level. For very high pillars the distance can be larger.
- An increase in the pad length leads to stiffer structures as expected. For large deflections short pads or pillars should be used.
- The maximum deflections are barely dependent on the refresh time and the dwell time which is an essential information as it reflects a widely constant chemical composition. By that the influence of process parameters is proven to be of minor relevance which simplifies the fabrication on the one hand and proves reliable analyses.
- For large deflections an elastic and a plastic behavior was observed which is discussed in the next chapter as it is also very important.

For a further deflection analysis simulations have to be performed as described in chapter 3.4.

4.3.2 Elastic and plastic behavior

It was observed that the deflection of the FEBID structures seems to be a not fully reversible process for extreme process parameters. By that, the structures remain slightly bended when the force is removed. To examine this in further detail, the pillar deflections were measured for several electrode voltages directly after applying the potential. After each measurement the voltage was again set to 0 V and the remaining deflection was measured to determine the plastic part. An example for a quasi-1D pillar deposited with 5 pA with a height of 4.88 µm and an electrode distance of 2 µm is shown Figure 4-23 (left). One can see that the plastic part increases with higher electrode voltages. It was further observed that the maximum deflection seems to increase when the pillars are post-irradiated during the observation which is shown in the right graph. This will play an essential role later in this thesis.

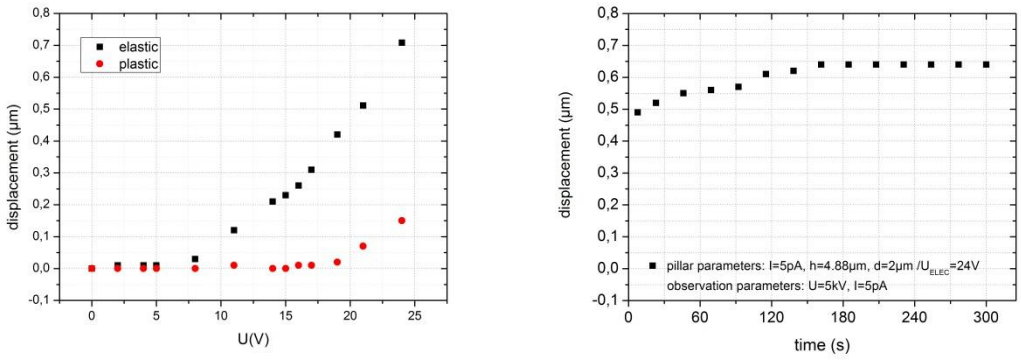

Figure 4-23: determination of plastic and elastic contributions during deflection experiments in dependence on the applied electrode voltage (left). The right image shows the varying deflection during post-growth treatment at 5 keV and 5pA primary energy and beam current, respectively.

In a following experiment some pillars were deflected for some time by applying a voltage to the electrode without observation of the maximal displacement with the e-beam. Then the voltage was switched off and the plastic bending was measured again. Surprisingly, the plastic part vanished completely! Therefore, it can be concluded that the plastic behavior just comes from the interaction with electrons during observation and not from the mechanical stress caused by deflection itself. This is an essential result as we can conclude that the pillars itself show ONLY elastic behavior. Furthermore, it defines a special characterization route where the pillars are imaged with minimum interaction via the small survey window in the SEM.

4.4 Resonance experiments

For performing the resonance experiments, the experimental setup described in chapter 4.2 was used. As a reminder, the initial prediction was that the deposited structures should go into mechanical resonance when the AC voltage approaches the intrinsic resonance frequency of the pillar. The according experimental setup is shown in Figure 4-24. The pillar is deposited in front of the deflecting electrode. The determination of the resonance can either be done in side view by tilting the stage or in top view. To minimize the damage caused by the electrons during observation (previous chapter) the examination from top view was used in all the following measurements.

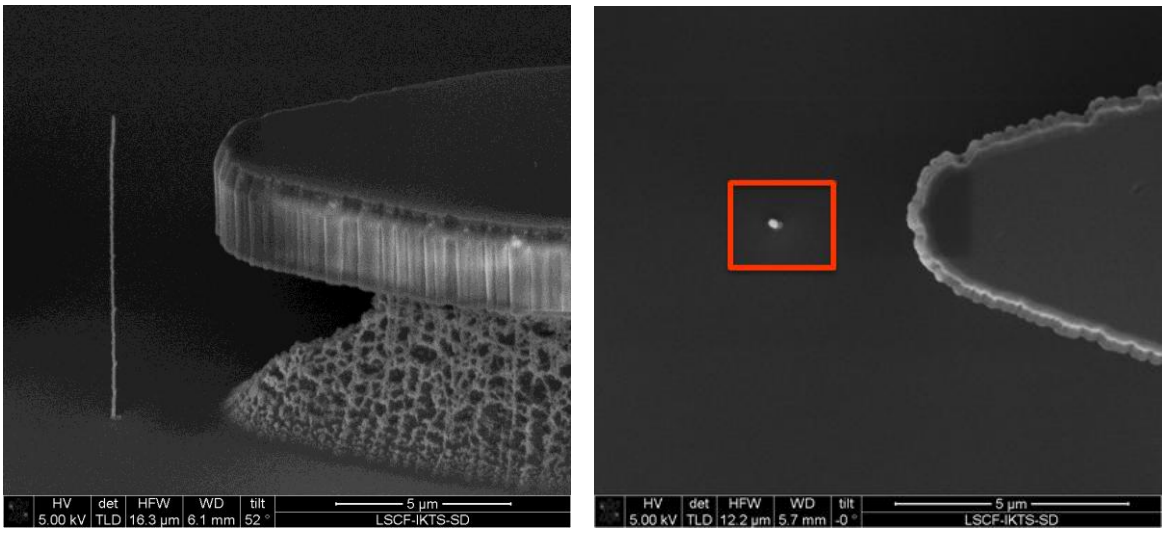

Figure 4-24: Resonance experiment for a pillar deposit in side view (left) and top view (right)

It could be shown that the structures actually could be brought into resonance by the alternating electric fields. To find the resonance frequency a frequency sweep was performed from 1 kHz up to 1MHz while the pillar was observed with the electron beam via the small survey window as schematically indicated in Figure 4-24 by the red frame. At the mechanical resonance a deflection of the FEBID structures could be seen which will be shown in the following.

Since the electron beam of the SEM is rasterized quite slow across the surface the deflection of the FEBID structures cannot be time-resolved but instead the mean of the signal for each pixel can be detected which corresponds to the residence probability. As an example a pillar deposit is shown in Figure 4-25. When no field is applied the pillar is represented as circle in top view like shown in (a). Near the resonance frequency a slight deflection towards the attracting electrode can be observed as shown in (b). When an electrical AC field is applied to the electrode it also interacts with the electron

beam and adds noise and distortion to the image. The image is slightly smeared out which can make it difficult to find the exact position of the maximal deflection. This leads to a small measurement error when searching for the exact value of the resonance frequency, but for most of the performed measurements it can be neglected. The resonance itself and by that the proof-of-concept can be seen in Figure 4-25 (c). As it is obvious the max. amplitude is around 1 µm which is significant.

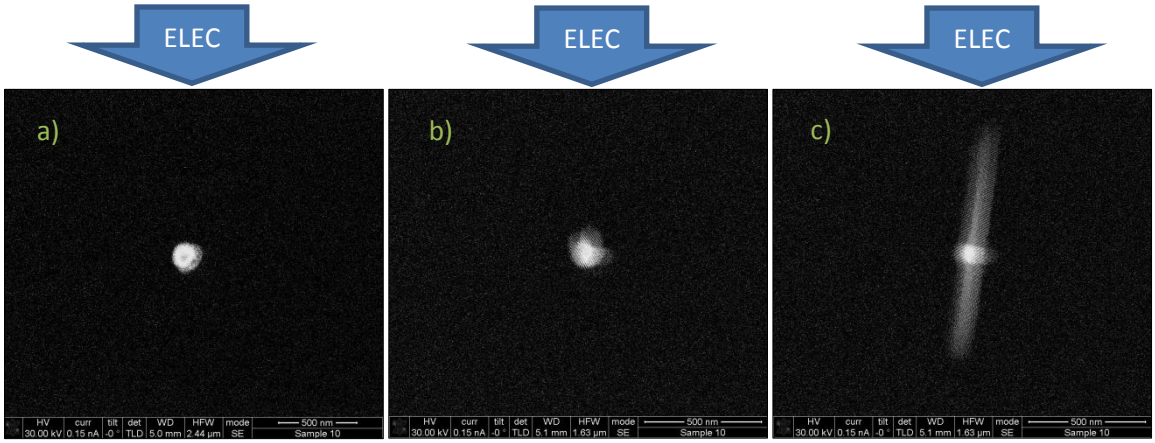

Figure 4-25: Pillar resonance experiment without electric field (a); with alternating field near the resonance frequency (b); and finally at the resonance frequency (c) where the quasi-1D pillar is resonating towards the electrodes (see indications). The exciting electrode was positioned above the pillars.

4.4.1 Quasi-1D resonators

Originally it was assumed that the pillars have one fundamental resonance frequency which is deflected exactly towards the exciting electrodes. The experiments, however, revealed another behavior: ***1)*** there are 2 fundamental resonance frequencies which are close together; ***2)*** the 2 resonance modes are nearly perpendicular as shown in Figure 4-28; ***3)*** the angles between the deflecting electrode and the resonance directions is seemingly random. As this is of essential importance and also quite surprising, further specific experiments have been performed. At first the influence of the gas flux direction during the growth process of the pillar deposits was observed. The gas flux direction is determined by the input angle of the gas injection system as shown in Figure 4-26. Several pillars were deposited, while the angle between the GIS nozzle and the deflecting electrode was systematically varied. Because the GIS direction cannot be changed, this can be achieved by rotating the whole sample with the stage. Focus and stigmator settings had to be adjusted after each rotation to achieve good focus conditions.

In Figure 4-26, η describes the angle between the deflecting electrode and the gas flux direction, $\vartheta 1$ describes the angle between gas flux direction and first resonance mode and $\vartheta 2$ the angle between gas flux direction and second resonance mode. It was observed that there is no relation between the gas flux direction and the resonance angle of the pillars like shown in the summary in Figure 4-26 (right). Since the only parameter that was changed during the experiment was the stigmator settings it can be concluded that slight variations of this setting could be responsible for the varying resonance directions. Since the determination of the optimal focus and stigmator conditions is subjective and very small misalignments cannot be realized a perfectly round beam shape is hard to establish. Wrong stigmator settings lead to a slightly elliptical beam which leads to the growth of

elliptical pillars. The elliptical shape explains the occurrence of the two perpendicular resonance modes, since there are two different radii which lead to different resonance frequencies. Both of the modes are excited, since there is a force component in both directions as shown in Figure 4-27.

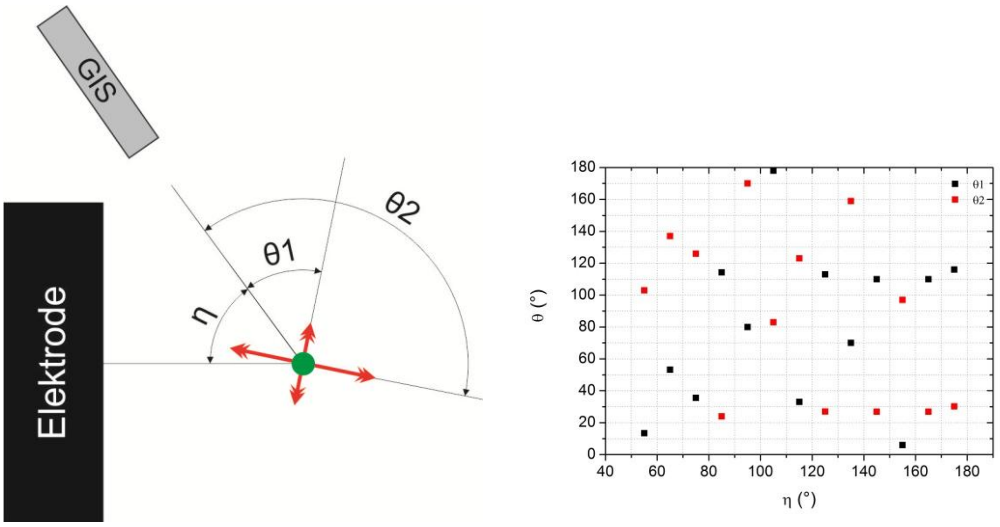

Figure 4-26: Schematic resonance experiment to find a correlation between gas flux direction and resonance angle (left); Resonance angles of different pillars in dependency of gas flux direction during deposition (right)

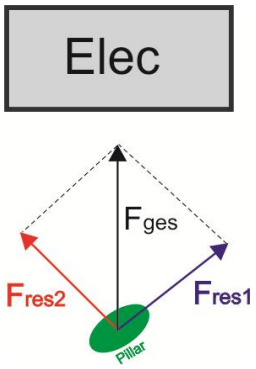

Figure 4-27: Force components acting on an elliptic pillar

Some examples for pillars in resonance are shown in Figure 4-28: A-E represents SEM images of different pillars at their fundamental resonance frequencies. The resonance mode with the lower frequency is shown at the top and resonance mode with the higher frequency is shown at the bottom. The deflecting electrode was positioned above each pillar. The maximum deflection is dependent on the applied voltage, the height and width of the pillars, the distance of the pillars to the electrode and also on intrinsic parameters like the Young's modulus which can differ from pillar to pillar due to subsequent e-beam radiation like explained later. This means that the deflecting electrode voltage had to be adjusted for the different pillars A-E to achieve comparable deflections. However, one can see that resonance mode in direction of the electrode is excited more than the perpendicular one. When the resonance angle between one of the two modes and the electrode is 0 degrees it is possible to excite just one of the resonance modes. This condition is nearly fulfilled for the pillars B and E. When the resonance angles of the two modes are about ±45° both modes are excited nearly equally like shown for the pillars A, C and D.

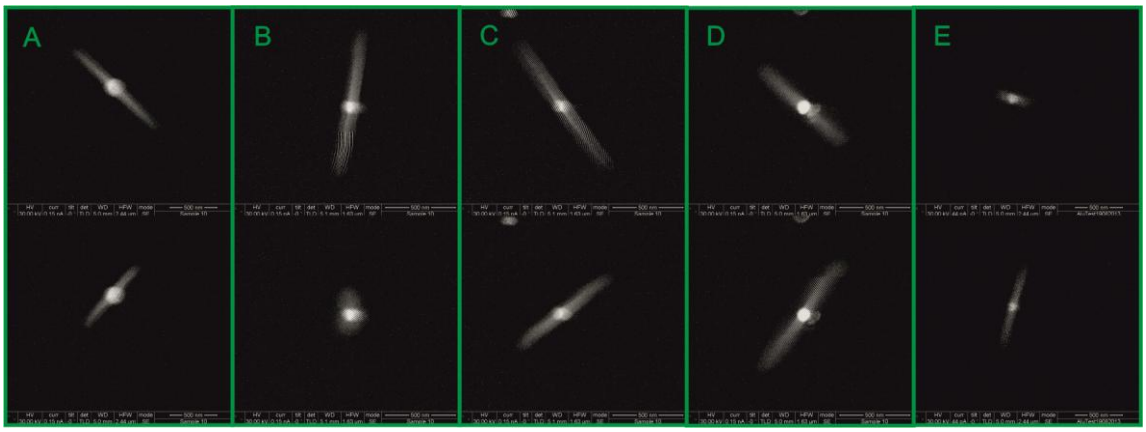

Figure 4-28: Resonance cases for different pillars. The exciting electrodes are located at the top side of the image

4.4.1.1 Resonance angle and deflection

Because of intrinsic damping effects due to the incorporated carbon matrix, the resonance peak is broadened. For further investigations resonance curves were determined like described in chapter 3.3.3. As example the resonance curves of two pillars and the resonance angle which describes the direction of the resonance are shown in Figure 4-29. An angle of 0 corresponds to a vibration in direction of the electrode.

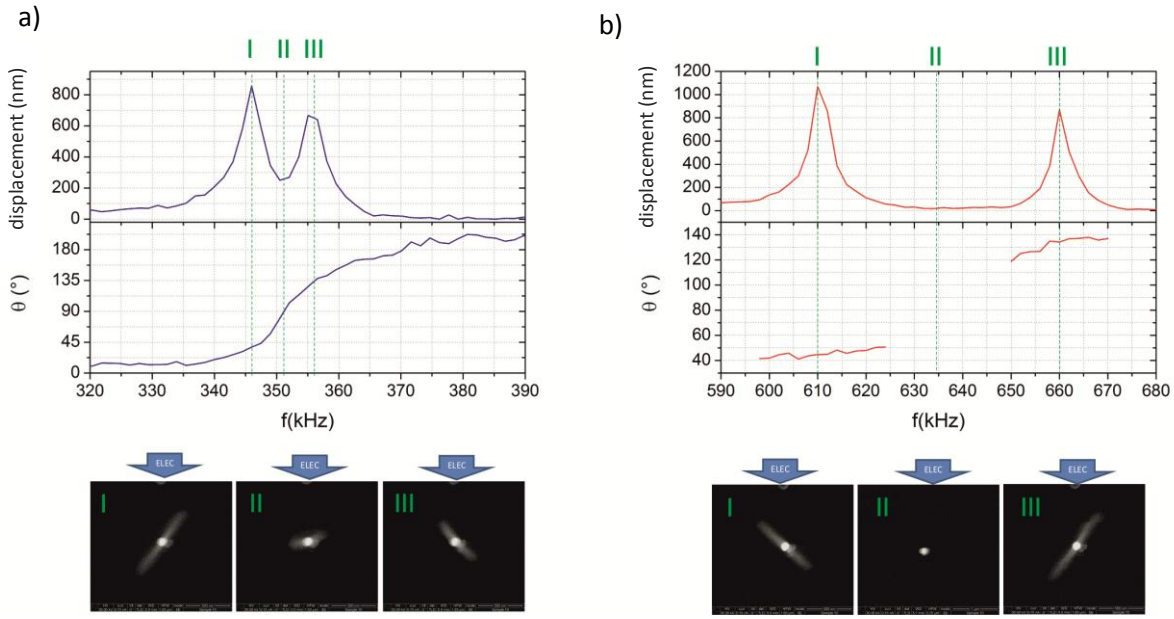

Figure 4-29: Resonance curves (upper panels) and deflection angles with respect to the electrodes (lower panels) for a pillar deposited with almost ideally aligned stigmator settings (a) and for a pillar deposited with slightly misaligned stigmator (b). The SEM images below show the resonance behavior at frequencies indicated above.

In the first case (Figure 4-29.a) the two perpendicular resonance frequencies are close together and their resonance curves overlaps. The stigmator settings have been aligned almost ideally. Since both resonance modes are excited simultaneously the pillar oscillates in an elliptic shape that becomes more and more circular when coming closer to the middle frequency (II). The resonance angle becomes larger with raising frequency and makes a rotation of 180° during the frequency sweep. The

angle between the resonance maxima is 90°. In the second case (Figure 4-29.b) the two resonance curves don't overlap. This corresponds to a more asymmetric pillar shape. When the frequency is swept upwards at first the lower frequency resonance mode is excited, then the pillar stops oscillating until the higher mode is excited. The phase in between cannot be measured. The angle between the resonance maxima is again 90°. One can see that circular or elliptic pillar oscillations are possible if the resonance curves of the two perpendicular resonance modes overlap or linear oscillations if they don't.

4.4.1.2 Suppression of the double frequencies

The excitation of both resonance modes at the same time is actually an unwanted side effect. One resonance can be suppressed by building asymmetric elliptic pillars on purpose, so that the larger axis is parallel to the exciting electrode. There is only one force component acting in direction of the deflecting electrode, the force component acting on the second pillar axis vanishes which means that the perpendicular mode cannot be excited. It is important to work with the TLD detector for the fine adjustments of the stigmator settings. The focusing strategy described in 4.1.2 with subsequent stigmator alignments can be used to achieve the elliptical beam shape. The resonance curve and phase angle of an on-purpose elliptical pillar is shown in Figure 4-30. To determine the asymmetry the width of the pillar was measured at several points along the height, parallel and also normal to the electrodes front face. In direction normal to the electrode the mean width revealed to be 69nm and in the perpendicular direction the width was determined to be 78 nm. This results in an asymmetry of 9 nm. As evident, only one resonance peak occurs. The deflection angle is zero (in direction of the electrode) and doesn't change for all frequencies. By that a simple procedure is found which gives only one resonance frequency further used throughout this thesis.

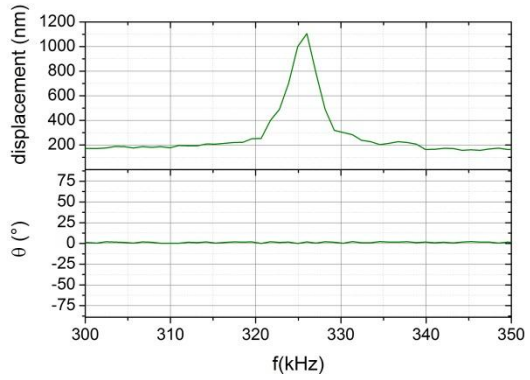

Figure 4-30: Resonance curve and deflection angle of double frequency suppressed pillar

4.4.2 Quasi-2D structures

In further experiments the resonance curves and deflection angles of quasi-2D pads and bridge arches were investigated. The pads were placed parallel to the electrode as shown in Figure 4-32. This also leads to a suppression of the second resonance frequency. At the resonance frequency the pads were vibrating directly in direction of the deflecting electrode which corresponds to a deflection angle of 0 °. Slightly above and below the resonance frequency the deflection angles slightly changes

like shown in Figure 4-31. This can be explained by the structure of the pads which consist of several slightly elliptic pillars that are distanced by the value of the point pitch and which touch each other.

The bow geometry is shown in Figure 4-32 (right). Also the bows are deposited parallel to the electrode. Just the resonance mode in direction of the electrode can be excited because there is negligible force component acting in the perpendicular direction. The resonance curve and resonance angle is shown in Figure 4-31 (right). As intended the resonance angle for bows is zero for all frequencies.

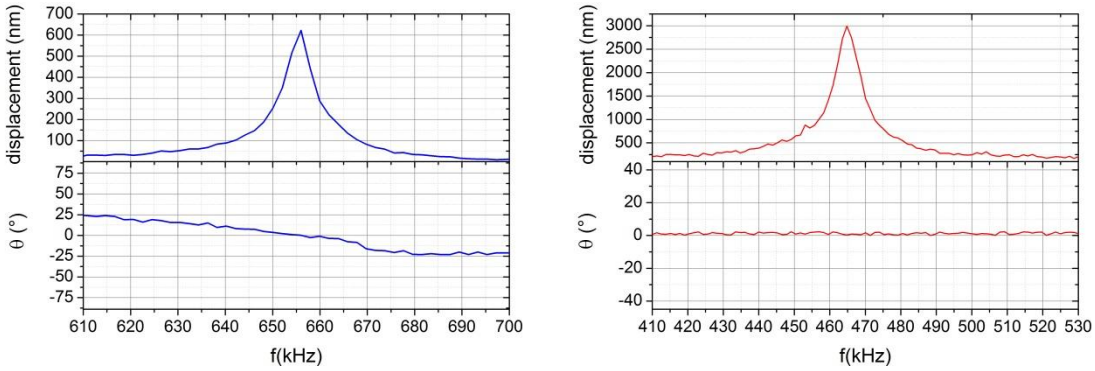

Figure 4-31: Resonance and resonance angle of pads (left) and bows (right)

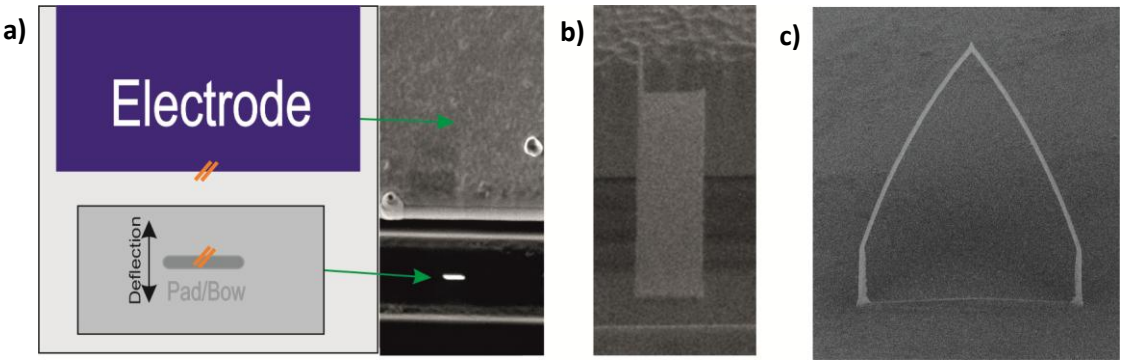

Figure 4-32: Arrangement of the pad and bow deposits (a), pad deposit (b) and bow deposit (c)

4.4.3 Resonance frequencies

In a set of experiments the resonance frequencies of different deposits were observed. To minimize the material variation during SEM inspection the microscope settings described in 4.2.4 were used. The detection of the resonance frequency was done in two steps. At first the excitation frequency was swept up quickly with a speed of 5 kHz/s until resonance occurred and a deflection could be clearly seen in the SEM. To find the exact position of the resonance maximum the frequency was manually adjusted in the second step. This can be done easily with the Labview program described in chapter 3.3.3.2. To prove that the resonance frequency behaves as predicted by theory a set of pillars were deposited in a first experiment and the resonance frequencies of the quasi-1D pillars were measured as described above. The pillar heights were systematically varied. This experiment

was done for pillars deposited with 5pA and 25pA electron current (5 keV). The result is summarized in Figure 4-33.

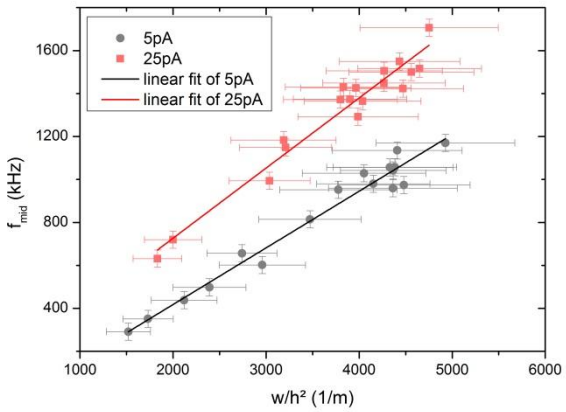

Figure 4-33: Resonance frequencies for quasi-1D pillars in dependency of w/h²

Like mentioned earlier every pillar has two closely spaced resonance frequencies due to the slightly elliptical shape. In the figure the average frequencies are shown which were calculated with the formula $f_{average} = (f1 + f2) / 2$ which approximates the resonance frequency of a perfectly round pillar. As a second approximation E and ρ (see equation (2.7)) are assumed to be constant which is justified by the widely similar resonance frequencies observed in chapter 4.4.1. As follows from equation (2.7), the resonance frequency f_{res} and w/h^2 follows a linear dependency:

$$f_{res} \propto \frac{w}{h^2} \tag{4.2}$$

Therefore, the resonance frequency is plotted as function of w/h^2 as shown in Figure 4-33. The data points of the 5 pA and the 25 pA pillars were fitted by linear functions going through the zero as needed. Please note, a relatively large error of ± 10 nm and ± 100 nm was assumed for widths and heights, respectively, to provide a realistic estimation of individual circumstances. The mean with of all the 5 pA deposits was determined with 63 nm and those of the 25 pA pillars with 65 nm. Due to the width variations along the pillar height axis the widths were measured at 5 positions along each pillar and the mean value was taken, which led to the error assumed. Nevertheless, the measurement error is relatively large since the variations are randomly distributed along the Z axis. The higher resonance frequencies of the 25 pA pillars (red) in comparison to that of the 5 pA pillars (black) can be described by a slightly higher Pt-content of the 25 pA deposits which was observed in previous works [4]. The higher Pt-content leads to an increased Young's modulus and thus to a higher resonance frequency like shown in equation (2.7). It also was observed that different values for dwell- and refresh-times have no significant influence on the resonance frequency (see also chapter 4.1.4.2). One can see that the error bars for higher pillars becomes smaller due to the smaller becoming influence of the width described by the relation (4.2). This can also be observed by looking at the frequency splitting (see chapter 4.4.1), which is determined by the frequency of higher resonance mode minus the frequency of lower resonance mode. As can be seen in Figure 4-34 the splitting becomes larger for shorter pillars like shown below since here the width differences of the

two pillar axes have stronger influence. Therefore, it can be concluded that the quasi-1D pillars indeed behave as predicted by theory discussed in 2.3. Furthermore, it can be seen that resonators fabricated at higher currents lead to higher resonance frequencies. Due to the fact that the diameters are very similar (63 nm and 65 nm for 5 pA and 25 pA, respectively) it can be concluded that high-current-pillars have a higher Young's modulus (stiffer properties). This is in agreement with the fact that higher currents lead to slightly higher Pt content of about 20 at.% compared to about 15 at.% for low current pillars. Therefore, the beam current can be used to control the basic stiffness of the pillars while the height can be used for further frequency adaption.

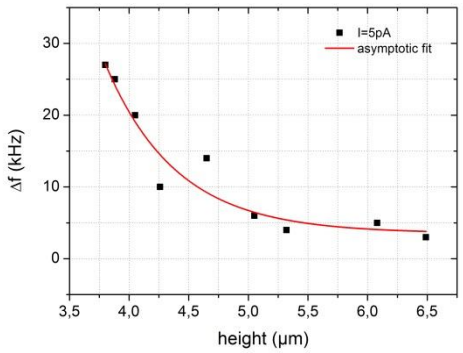

Figure 4-34: Frequency splitting in dependency on the height for 5pA pillars (right).

In order to compare the above discussed results, also quasi-2D pads are investigated as discussed in chapter 4.1.4 and chapter 4.4.2. Figure 4-35 shows the resonance frequencies of different pads with a length of 60 nm, 120 nm and 240 nm (see legend) fabricated at 5 keV, 25 pA, 60 nm PoP and 100 µs DT. The blue line is the linear fit curve through zero that was used for the 25 pA pillar deposits in Figure 4-33 (black).

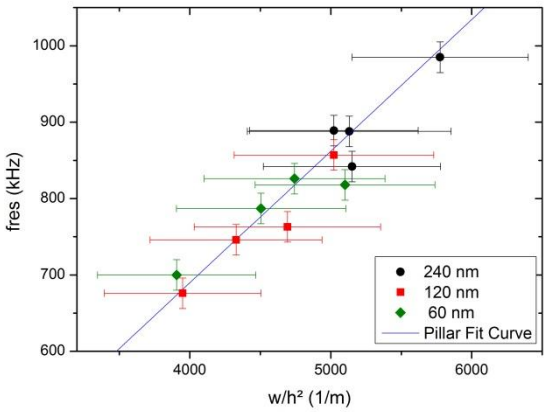

Figure 4-35: Resonance frequencies for pads with different lengths in dependency of w/h²

It seems that quasi-1D pillars and quasi-2D pads have the same resonance frequencies since all the data points are on the same line. This can also be proved theoretically: the resonance frequencies for cubic pads can be calculated by using Equation (2.5) using following relation for the area moment of inertia:

$$I_{zPlate} = w * l * \frac{w^2}{12} \tag{4.3}$$

$$f_{1Plate} = \frac{(\beta_1 h)^2}{2\pi h^2}\sqrt{\frac{E}{\rho}}\sqrt{\frac{w^3 l}{12}}\sqrt{\frac{1}{l * w}} = 0{,}1399\sqrt{\frac{E}{\rho}}\frac{w}{h^2} = f_{1Pillar} \tag{4.4}$$

where ***h*** is the height, ***w*** the width, ***I*** the area moment of inertia, ***E*** the Young's modulus determined from the bending experiments and ***ρ*** the density of the pillar. One can see that pillars and pads indeed should have the same resonance frequency as the length of the pad doesn't have any influence from theory. Hence, one can conclude that basically it does not make a difference whether 1D or 2D structures are used which opens new possibilities for finally used structures. After observing the resonance frequencies the focus was given to investigations of the pillar deflections which can be reached. To reveal the maximum deflection in dependence of the pillar heights a set of pillars was deposited with e-beam voltage of 5kV and a current of 5pA in a distance of 2.5µm from the exciting electrode.

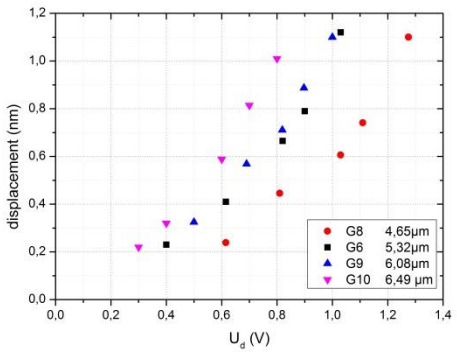

Figure 4-36: Maximal deflections of pillars in resonance with different heights

Like expected the displacement for higher pillars is larger than for shorter ones.

Another detail has to be considered for further discussion. All resonators were excited with a sine signal and it was observed that excitation is possible at two frequencies: ***1)*** exciting frequency corresponds exactly to the pillars resonance frequency and ***2)*** exciting frequency is exactly half of the pillars resonance frequency. This can be explained by looking at the equations for the force that acts on the pillar during excitation:

$$F = \frac{1}{2}\frac{\partial C}{\partial x}(V_{input})^2 \tag{4.5}$$

where $\frac{\partial C}{\partial x}$ is the change in capacity caused by the bending and V_{input} is the excitation voltage with a sinusoidal excitation voltage V_{input} can be described by :

$$V_{input} = V_{DC} + V_{AC}\sin(\omega t) \qquad (4.6)$$

where V_{AC} is the amplitude of the exciting alternating voltage, V_{DC} is on overlaid direct voltage and ω is the circular frequency of the exciting alternating sinus signal. Insertion into the force equation (equation (4.5)) yields:

$$F = \frac{1}{2}\frac{\partial C}{\partial x}\left[{V_{DC}}^2 + \frac{1}{2}V_{DC}V_{AC}\sin(\omega t) - \frac{1}{2}{V_{AC}}^2\cos(2\omega t)\right] \qquad (4.7)$$

Where F is the electrostatic force acting on the pillar, $\frac{\partial C}{\partial x}$ is the change in capacity caused by the bending, V_{AC} is the amplitude of the exciting alternating voltage, V_{DC} is on overlaid direct voltage and ω is the circular frequency of the exciting alternating sinus signal. Although the structures are excited with pure **AC** signal the **DC** term does not vanish as there is a potential difference between the exciting gold electrode and the PtC pillar due to the different working functions of the materials. Due to the ***sin(ωt)*** term, the exciting force matches the resonance case when the exciting frequency is equal to the resonance frequency. Because of the ***cos(2ωt)*** there is also a force component that has the double frequency of the exciting signal. That's why mechanical resonance occurs even if the excitation frequency is only half the pillars / pads frequency. In an experiment the maximal deflections of a pillar in resonance was observed when exciting with half of the resonance frequency or directly with the resonance frequency. The pillars were deposited with a primary energy of 5 keV and a current of 5pA in a distance of 2.5 µm from the exciting electrode. For the experiment the FIB test structures described in chapter 4.2.2.2 were used.

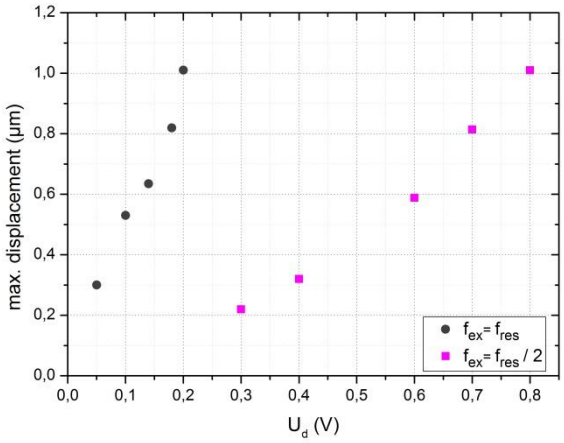

Figure 4-37: Maximal deflection of pillar excited to resonance by a sinusoidal signal in dependence of the signal amplitude. The black curve shows the deflections for excitation frequencies that correspond to the resonance frequencies; the violet curve shows the displacement for excitations with the half resonance frequency.

One can see that larger deflection can be achieved by using the resonance frequency for excitation. As total summary of chapter 4.4.3 we can state that DC deflection follows the expected behavior and is also independent on the length of quasi-2D pads. Furthermore, higher currents lead to stiffer

structures as consequence of slightly higher Pt contents. Finally, AC excitation lead to a resonance of FEBID structures as predicted. Essentially important is the fact that two resonance cases are found for AC excitation frequencies ω and $\omega/2$ which is important to keep in mind for final calculations. As a practical detail we can conclude that the length can also be used to control both: resonance frequencies and its final amplitude for a given electrode voltage.

4.4.4 Frequency shift

To determine if different environmental conditions or post growth treatments have influence on the stability or the location of the resonance frequency a series of experiments were performed that are described below.

4.4.4.1 Intrinsic variation

In a first measurement series it was determined whether there is an intrinsic frequency shift with time as initial aging has previously been observed [7,6,17]. For this a series of quasi1D pillars with different heights were deposited with 5 pA and 25 pA beam current. Directly after the deposition process the value of the fundamental resonance frequency was measured. To observe the long-time stability of the resonance frequency the pillars were left in the vacuum chamber of the dual beam microscope for 48 hours without any further treatment. Then the value was determined again. It was found that all pillars reveal identical resonance frequencies directly after fabrication and after 48h. These experiments were repeated for pillars which were removed from the vacuum chamber directly after fabrication and initial measurements. After 1 week storage in ambient conditions (18 °C, no direct UV exposure) the pillars were characterized a second time in the DBM also revealing practically identical resonance frequency. This excludes intrinsic resonance changes which are an essential detail for further processing.

4.4.4.2 Temperature treatment

In a next step, the influence of temperature on its resonance stability was investigated. Therefore, pillars were deposited on different substrates which afterwards have been placed into an oven at ambient atmospheres. The substrates were treated with temperatures between 40°C and 150°C, each of them for 45 minutes. It was observed that the geometry of the pillars stays stable up to a temperature of 65°C as can be seen in Figure 4-38 (a). For higher temperature deformation of the FEBID material takes place as shown in Figure 4-38 (b). The resonance frequencies before and after the treatment were compared for all the pillars. The experiments revealed that all undeformed pillars showed no resonance shift upon temperature treatment which means that the intrinsic structure up to 65°C doesn't change. For higher temperatures, the carbon is expected to reorganize leading to an unpredictable deformation which prevents any further use.

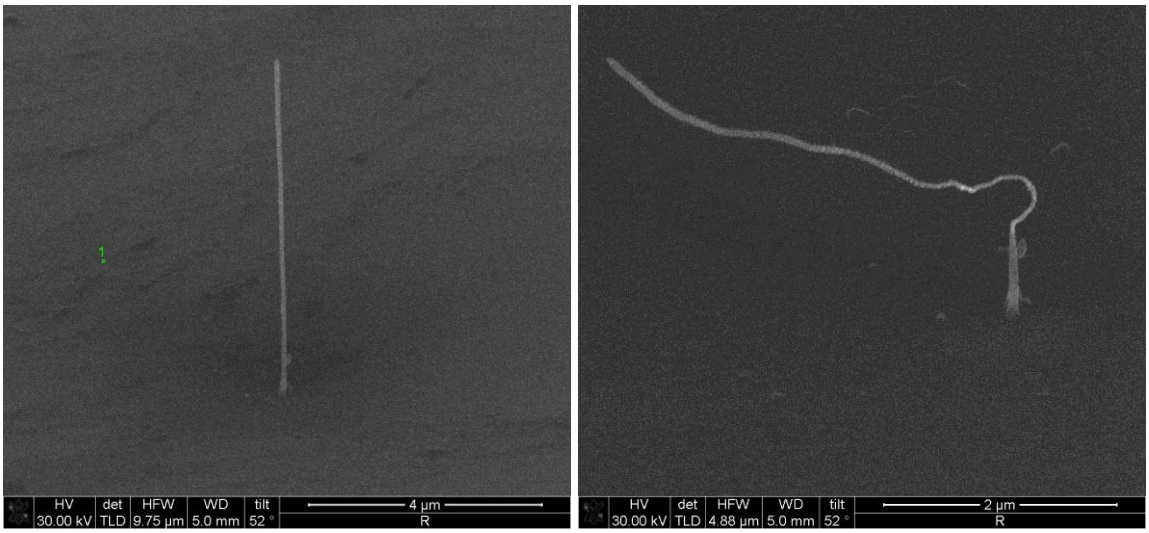

Figure 4-38: Pillar after 30 min treatment with a temperature of 60°C (a); same pillar after additional treatment with 90°C (b)

4.4.4.3 E-Beam treatment

As an essential part of this thesis, the post-growth-treatment (PGT) by means of additional e-beam exposure has been investigated. From previous work [6,7] it was known that FEBID deposits can be cured by post-growth e-beam treatment actually finalizing incomplete dissociation which is accompanied by a slight growth of Pt particles (1.7 nm → 2.2 nm in previous work). Therefore, a detailed investigation has been set up, described in the following.

Side view curing

To study the influence on the resonance frequencies different pillars were cured for a specific time from the side by tilting the stage and exposing the pillar to the e-beam with a primary energy of 30 keV at varying currents. It was found that e-beam current should not exceed 150 pA to prevent a charge induced deformation. The experimental setup is shown in Figure 4-39 by a tilted SEM image. The area of irradiation is determined by a square pattern which is scanned by the electron beam. All the pattern settings are summarized in Table 4-2.

Table 4-2: Settings used for the curing pattern

size_x	420	nm
size_y	7000	nm
Pitch	4	nm
DT	1	µs

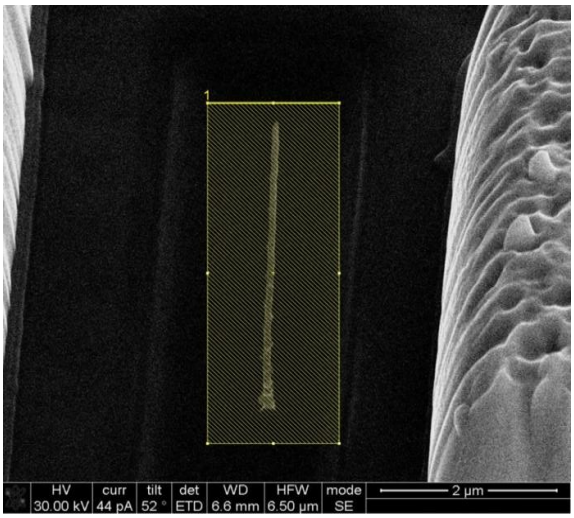

Figure 4-39: Electron post growth treatment (PGT) from the side

As expected a shift of resonance frequencies was found after PGT via the e-beam. To observe this in more detail the resonance frequency shift in dependence of the irradiation time was determined. For this purpose the stage had to be tilted back to 0° after each irradiation period to measure the resonance frequency from top view. The results for two different curing currents are shown in Figure 4-40 (a) for two pillars with fundamental frequency of 300 kHz in the uncured state. The frequency shift for pillars cured with 150 pA (red curve) is much larger than for 44 pA (black curve). It was determined, that the frequency shift can also be expressed as a function of irradiation dose which can be calculated by:

$$D = \frac{I_e * t}{A_{Pt}} \tag{4.8}$$

with the electron dose $\boldsymbol{D}$, the electron current $\boldsymbol{I_e}$, the patterning area $\boldsymbol{A_{Pt}}$ and the irradiation time $\boldsymbol{t}$. The dose dependent curves for both curing currents are shown in Figure 4-40 (b). As can be seen, both curves are practically identical which indicates that the change in the intrinsic structure is independent of the electron current and just the number of impinging electrons is responsible for the increased resonance frequency.

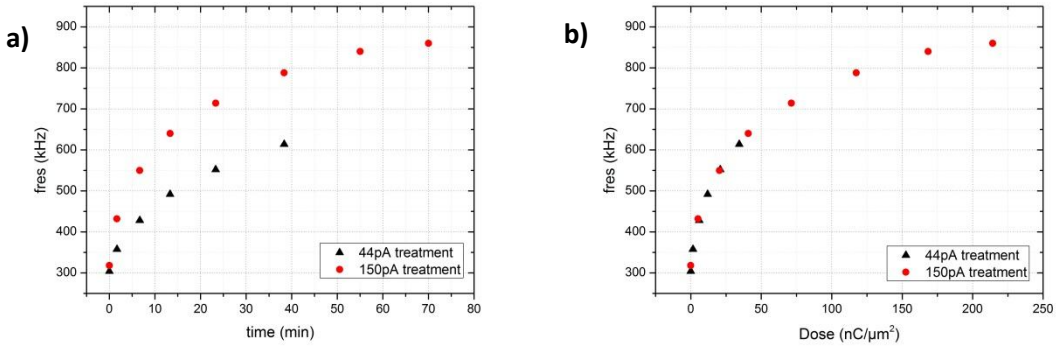

Figure 4-40: Resonance frequency of the pillars in dependence on irradiation time (a) and in dependence of the irradiation dose (b) for post growth treatment at 44 pA and 150 pA e-beam current (30 keV).

To further investigate the frequency shifts the experiments were repeated for pillars with different heights and deposition currents. The pillar parameters can be found in Table 4-3 and the results of the experiment are summarized in Figure 4-41.

Table 4-3: Essential pillar parameters for the curing experiment with I the deposition current, h the height and w the width of the pillar

	P1	P2	P3	P4	P5	
I	5	25	25	25	25	**pA**
h	3,93	4,25	4,16	4,06	3,73	**µm**
w	68	69	70	67	68	**nm**

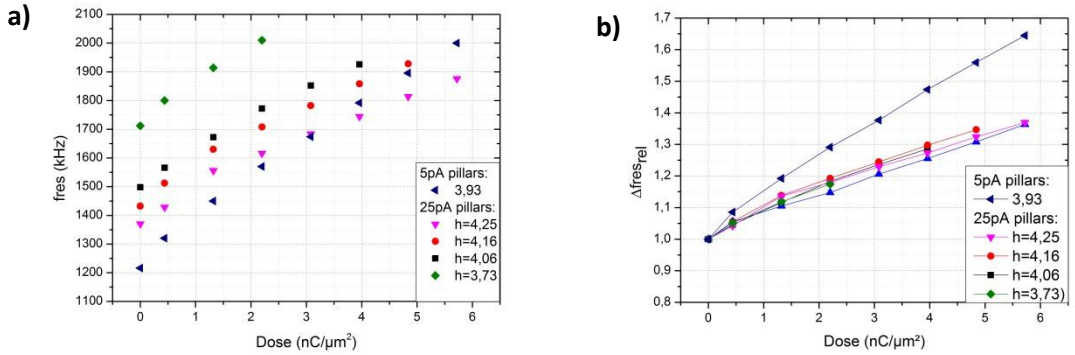

Figure 4-41: Frequency in dependence of the irradiation (a) and relative frequency change in dependence of the irradiation dose (b) for pillars with different deposition currents and heights

As evident, the increase in frequency for pillars deposited with 5 pA is stronger which can be seen in the relative variation plot in Figure 4-41. This is an essential finding as it is known from previous work that lower current tend to incorporate incompletely dissociated precursor molecules which are then finalized during PGT via the e-beam. The height dependency, on the other hand, is found to be similar with respect to relative variation which is consistent with the assumption of constant chemistry for heights > 2 µm as observed before [4]. Another crucial detail is that the widths are practically identical as shown in Table 4-3.

These observations confirm the assumption that a change in the intrinsic parameters (E or ρ) has to be responsible the change in frequency (see equation (2.7)), since the geometrical parameters barely change during the curing process. In chapter 4.4.6 this is explained in more detail.

Top view curing

The curing can also be done from top while the pillar is kept in resonance. This can be achieved by readjusting the exciting frequency. It was simulated via CASINO that 30 keV electrons have a penetration depth of 3 – 5 µm in typical FEBID material consisting of 15 – 20 at.% Pt. The requirement for the resonance situation ensures that the pillar can be uniformly curried even for very long pillars. Due to the deflections in resonance the electron beam reaches deeper lying parts of the pillar. Since also the area around the pillar is irradiated it comes to the production of backscattered electrons which can also cure its bottom area as shown in Figure 4-42 (c). Furthermore

the pillars are deflected alternately to the left and the right side when they are brought to resonance, which enables symmetrical curing of both sides. The resonance frequency in dependence of the irradiation time for a pillar deposited with 5pA is shown in Figure 4-42 (a). Curing was performed at 30 keV / 44 pA using a square pattern with a size of 326 x 354 nm as shown by Figure 4-42 (b). Dwell times were 1 µs and a point pitch of 4 nm was used.

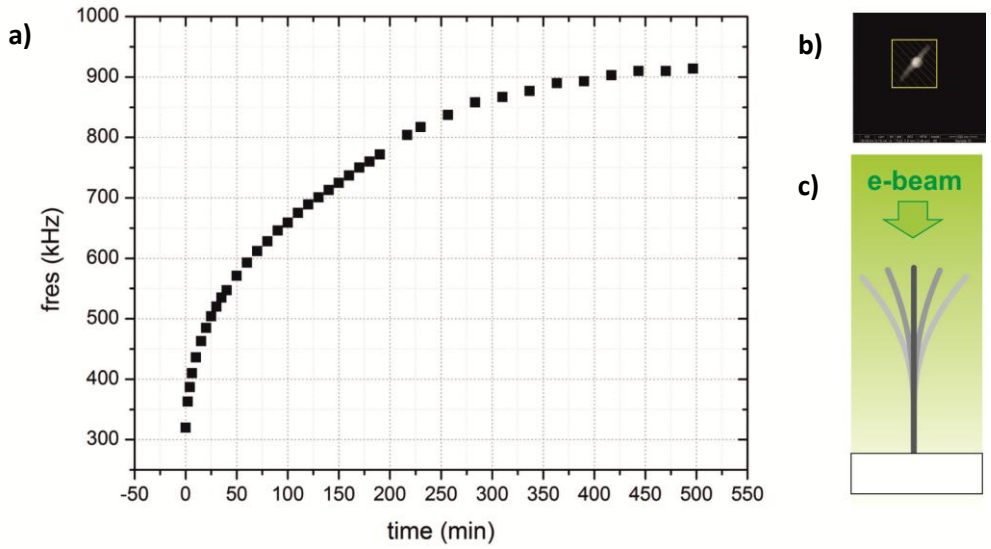

Figure 4-42: (a) resonance frequency in dependence of irradiation time for top view curing from top (b). (c) shows the concept of resonance curing via top view which ensures entire curing of the pillar.

As can be seen in Figure 4-42 (a) the resonance frequency saturates after about 500 minutes with resonance values about three times higher than the starting frequency. This again is consistent with previous studies were electrical conductivity was investigated in dependency on the exposure dose revealing the same saturating behavior [6,7]. Hence, it can be concluded that this top view curing has several advantages:

1. The *resonance frequencies* can be *measured in-situ during curing*, which means that the FEBID-structures can be *fine-tuned to any desired resonance frequency*.
2. The FEBID structures behave more stable because they are cured symmetrically, which lead to a minimization of bending during the curing process.
3. The curing can be performed with higher current which leads to a shorter process time. Up to 630nA curing current are possible without destroying the structure geometry.

It was found that for an optimal and fast frequency tuning the curing should be started with lower e-beam currents. When the frequency shift becomes smaller the current can be increased up to 630 nA. Above this value a geometrical deformation takes place which should be prevented.

4.4.4.4 Mechanical stress

As the resonators are in fast motion and the deposit consist of a nanogranular Pt grains embedded in a soft carbon matrix, a series of experiments have been performed to investigate possible mechanical influences during resonance. Therefore, the initial resonance frequency of the pillars was

determined after fabrication. After a first short e-beam curing period, the curing e-beam was switched off to minimize influences of the electron beam, while the pillar was hold in resonance for some time. In a next step the e-beam was switched on again to determine whether the resonance frequency has been shifted or not. A slightly increase in the resonance frequency was observed which differs from pillar to pillar. It is supposed that this shift comes from the observation with the electron beam itself and not form the mechanical treatment. Figure 4-43 shows the frequency shifts of comparable pillars which were kept in resonance. One pillar was illuminated permanently while the other one only was illuminated minutely for approximately 3 seconds to determine and readjust the actual resonance frequency. After 48 minutes, which corresponds to an effective illumination time of 4 minutes (48 * 3 s), the frequency shift of the resonance-only pillar (black curve) was determined which amounts 78kHz. The frequency shift of the permanently illuminated pillar after 4 minutes was found to be 76kHz. As the frequency values are comparable we can conclude, that the observed frequency shift comes from the e-beam observation ONLY and an influence of the mechanical oscillation is of minor relevance!

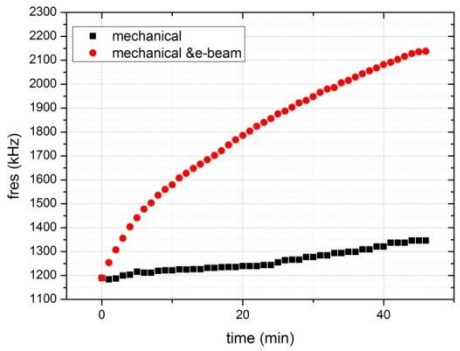

Figure 4-43: Comparison of the resonance frequency courses of two comparable pillars which were permanently hold in mechanical resonance plotted over time. One pillar (red curve) was permanently irradiated by electrons while the other pillar (black) curve was only irradiated minutely to readjust the excitation frequency.

4.4.4.5 Overlaid direct voltage

In further experiments the impact of an additional overlaid DC voltage on the AC resonance frequency was considered. Therefore, the voltage supply was connected in series to the frequency generator and the resonance frequency was measured for different DC voltages. The AC voltage was kept at $4V_{pp}$. The frequency in dependence of the applied DC voltage and also the associated resonance curves are shown in Figure 4-44. The fundamental resonance frequency is decreasing with rising DC signal. This downward resonance frequency shifting comes from a lowering in the spring constant of the material due to the electromechanical interaction. This effect is called *spring softening effect* and was observed by Hunt (1982) [18].

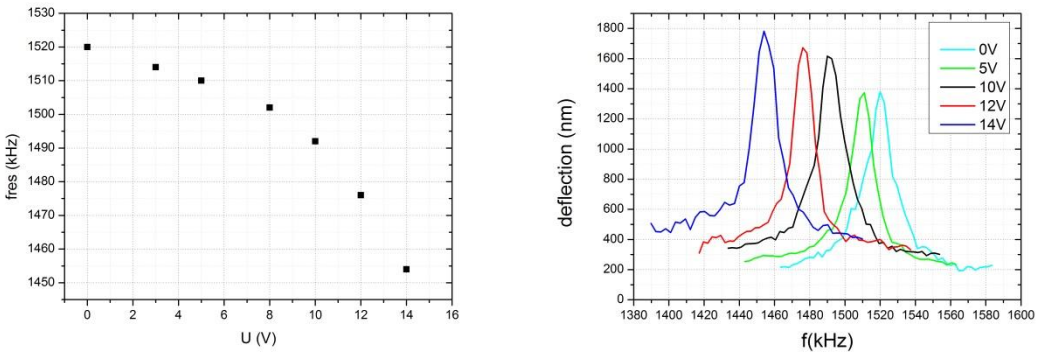

Figure 4-44: Frequency shift in dependence of the applied voltage (left) and associated resonance curves (right)

4.4.4.6 Resonance shift summary

In conclusion we can state that post-growth treatment by means of e-beam curing can be used to tune the pillars to higher frequencies by a factor of about 3. Depending on the chemical state of the incorporated carbon, tuning takes place faster (low current deposits). A closer look on structural effects during curing is given later. On the other hand, temperature, mechanical oscillation, and intrinsic aging does NOT influence the resonance frequency which makes it much easier to access the effects during e-beam curing. Before this is done a quick look is given on the resonance curves by means of full width half max values. This is of relevance for the sensitivity during final sensing applications.

4.4.5 Resonance Curves

In the following experiments the resonance curves were examined more closely. The determination of the curves is described in detail in chapter 3.3.3. The resonance curves for a set of different pillars were determined and observed closely. All the important pillar parameters are summarized in Table 4-4. The main difference between the pillars denoted by A and B is the different fabrication current of 25 pA (A) and 5pA (B). An overview of the resonance curves of the fundamental modes is given in Figure 4-45.

Table 4-4: Summary of all the important parameters for the examined pillars, with I the deposition current, U the deposition voltage, h the height of the pillars, w the average width of the pillars and fres1 and fres2 the value of the 2 perpendicular fundamental resonance frequencies

	A1	A2	A3	A4	B1	B2	B3	B4	B5	B6	B7	B8	
I	25	25	25	25	5	5	5	5	5	5	5	5	***pA***
U	5	5	5	5	5	5	5	5	5	5	5	5	***kV***
h	3,97	4,2	5,7	6,18	3,92	4,65	5,05	5,32	6,08	6,49	6,63	7,5	***µm***
w	70	70	65	70	71	64	61	60	64	64	64	64	***nm***
fres1	730	729	353	305	460	294	246	217	173	144	163	145	***kHz***
fres2	752	753	367	326	495	308	252	221	178	147		153	***kHz***

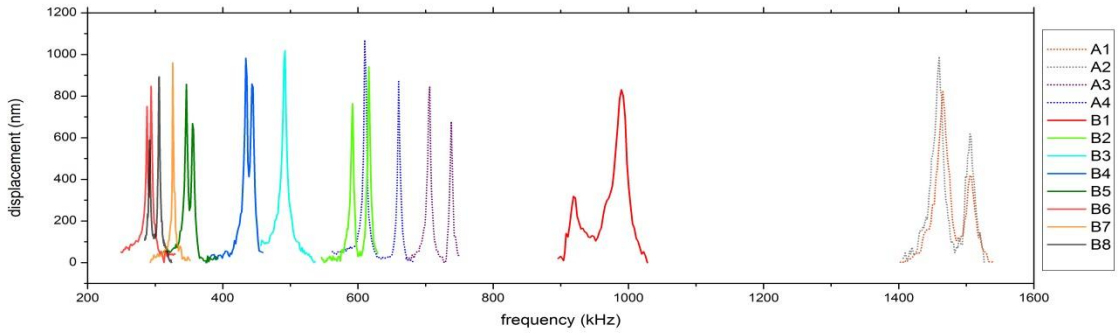

Figure 4-45: Overview of the resonance curves for the observed pillars

The resonance curve through each peak can be fitted by a Lorenz function:

$$d = d0 + \frac{2A}{\pi}\left(\frac{w}{4(f - f_c)^2 + w^2}\right) \tag{4.9}$$

with ***w*** the full width at half maximum (**FWHM**), ***A*** the height, ***d0*** the offset in deflection and f_c the resonance frequency. The function is illustrated in figure Figure 4-46.

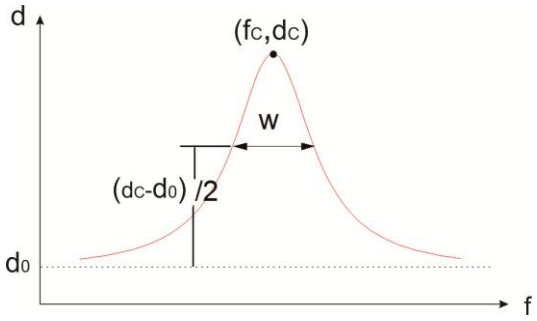

Figure 4-46: Lorenz function.

The resonance curves and the corresponding Lorenz fits of the fundamental modes of all observed pillars in untreated state are summarized in Figure 4-47.

4.4.5.1 Full width at half maximum

The FWHM is an important quantity which describes the sharpness of a peak. Especially, if one is interested in the investigation of small frequency shifts like it is required for sensing applications of the resonator the FWHM should be as high as possible. Like described above, the FWHM can be determined from the Lorenz fit. Because of the occurrence of two perpendicular resonance modes for some structures, two values for the FWHM can be observed for those which lie close to each other. For reason of clarity the mean value is represented in the graphs. In Figure 4-48.a the FWHM's of the observed pillars are shown. The data points for the 5pA pillars and the 25pA pillars are illustrated in black and blue, those for the 5pA pads in red.

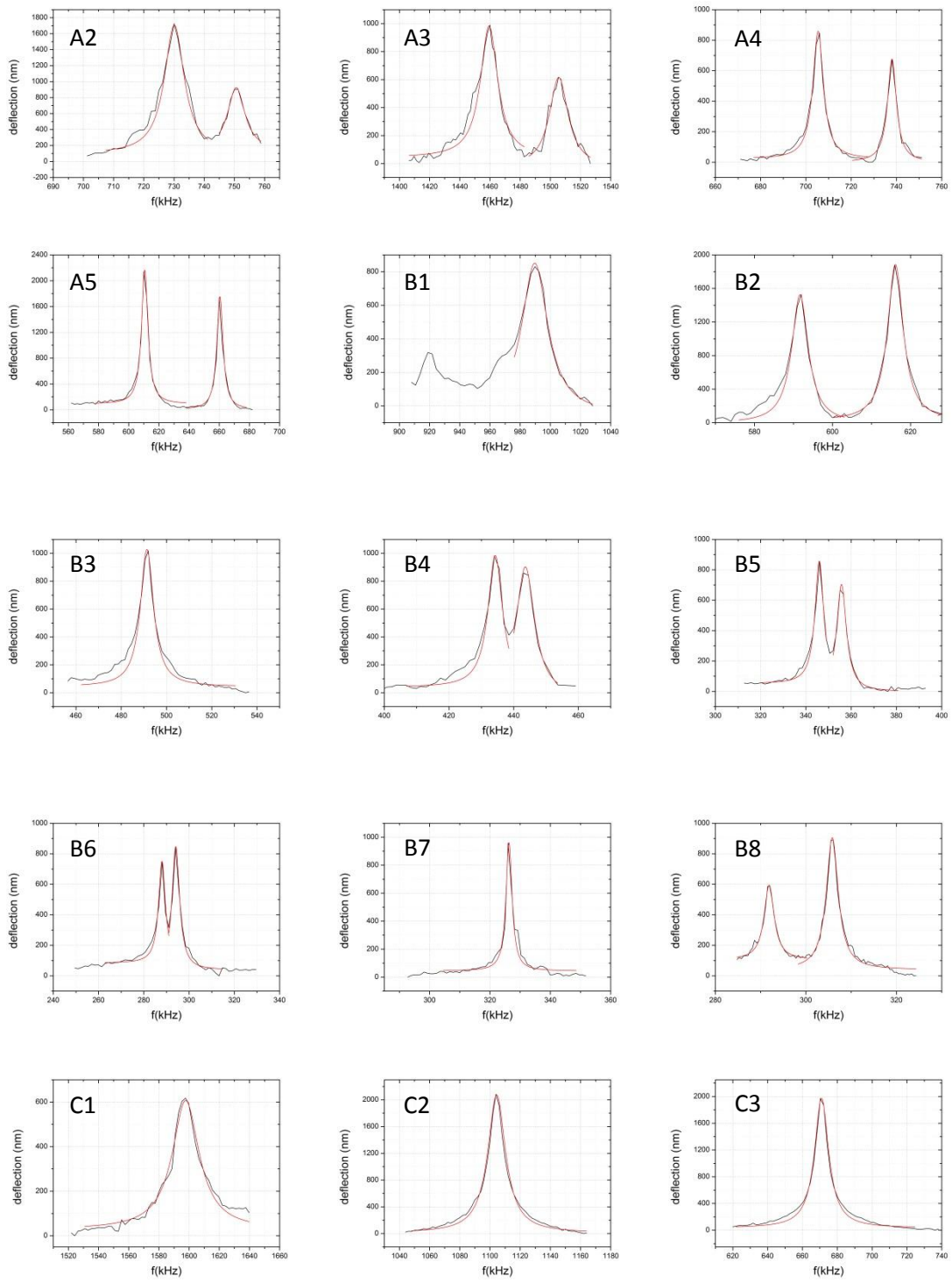

Figure 4-47: Resonance curves and Lorenz fits for the observed pillars as summarized in Table 4-4.

One can see that the FWHM can be reduced by choosing structures with lower resonance frequencies which can be achieved by increasing their height. Closer examinations the data points were divided into 2 groups: the pillars B3-B6, B8 and the pads C1-C3 (**group A**) show a linear dependency of the FWHM from the resonance frequency, and also the pillars A1-A5, B1,B2 and B7 (**group B**) like shown in Figure 4-48 (right). It can be derived that:

- **Group A** contains a number of 5pA pillars and also the 5pA pads which means, that their fundamental frequency is principally equal and in case of pillars and pads not dependent on the geometry
- **Group B** contains 5pA pillars and 25pA pillars which shows that the FWHM is barely dependent on the deposition current
- When comparing the two groups with the resonance curves illustrated in Figure 4-47 it becomes clearer that those structures where the resonance curves of the two perpendicular modes strongly overlay belong to group A, while the others belong to group B.

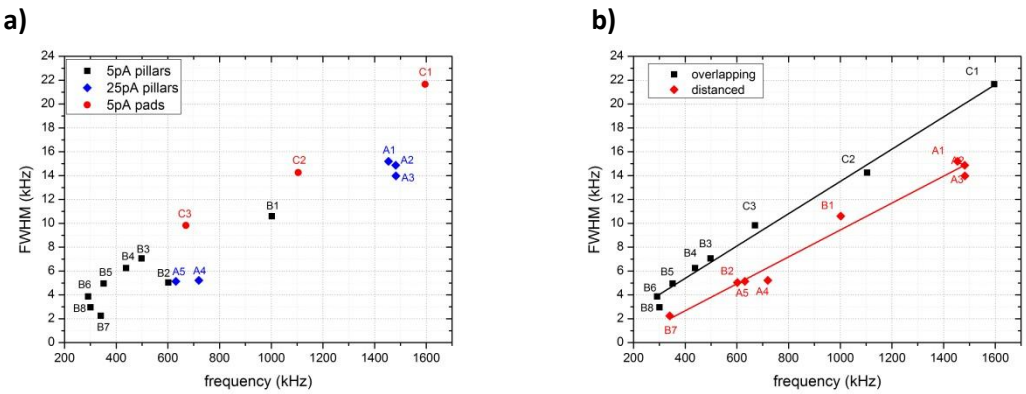

Figure 4-48: FWHM in dependency of the resonance frequency for the observed FEBID structures. The different deposit types (5pA pillars, 25pA pillars and 5pA pads) are highlighted in (a) and the two identified regimes in (b)

Hence, it can be concluded that the FWHM is dependent of the distance between the two resonance curves. A small FWHM for pillars can actually be reached by producing elliptical pillars where the resonance peaks are further apart, which also applies for the special case of the double frequency suppressed pillars described in chapter 4.4.1.2. This should also be possible for pads produced with an e-beam of slightly elliptic shape, where the larger axis has to be parallel to the exciting electrode. In some further investigations the influence of curing on the FWHM was observed. The result is shown in Figure 4-49. It can be seen that the FWHM decreases for all pre-cured pillars although the resonance frequency rises. Hence curing can be used to decrease the FWHM which is essential in terms of high sensitivity for potential applications. A first interpretation might be that the soft carbon matrix is getting less contributing after e-beam PGT leading to sharper curves. As we will see later this is indeed true. Before a closer look on this detail is given, the Q factor is investigated which is also important as a measure of relative broadening based on the carbon matrix.

4.4.5.2 Quality factor

The quantity factor characterizes the bandwidth of a resonator in comparison to its center frequency. The quality factor is inversely proportional to the damping of a system and describes the rate of energy loss in dependence of the stored energy in the system. Since the measurements were done in the vacuum chamber of the microscope the damping arises directly in the oscillating FEBID structures. Primary responsible for the quite high damping and the low quality factor in our resonators is the carbon matrix where the Pt-grains are embedded. The Q-factor can be calculated by

$$Q = \frac{f_{res}}{FWHM} \tag{4.10}$$

where f_{res} is the resonance frequency and ***FWHM*** is the full width at half maximum. The quality factors Q for the observed structures are shown in Figure 4-50. One can see that also the quality factor can be improved by increasing the distance of the resonance curves for the two perpendicular modes. Quality factors between 69 for close lying curves and 139 for far distanced resonance curves were observed.

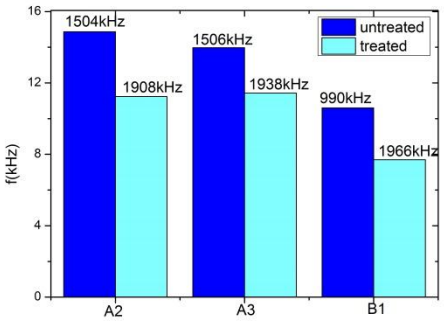

Figure 4-49: Influence of post growth electron treatment on the FWHM. The corresponding resonance frequencies are indicated above the bars

Further the quality factor can be increased significantly through e-beam curing which is illustrated in Figure 4-51 (a). Based on these result one can state that e-beam PGT is definitely a method to increase the sensitivity. Together with the previous section in which we demonstrated that the final frequency can accurately be tuned, this gives the required tools for ideal setup with respect to highly sensitive quasi-1D / -2D sensing resonators.

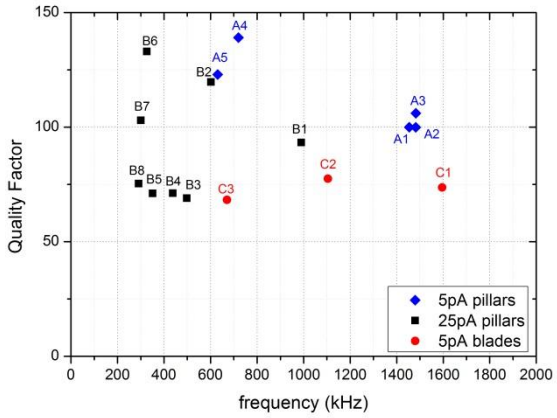

Figure 4-50: Quality factor in dependency of the resonance frequency for the observed FEBID structures.

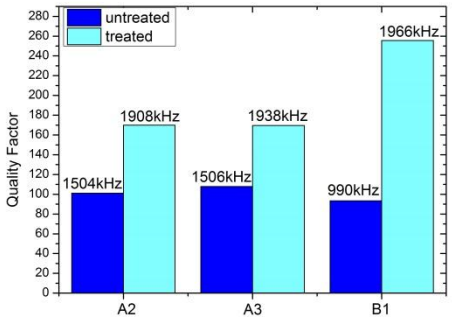

Figure 4-51: Influence of post growth electron treatment on the quality factor. The corresponding resonance frequencies are indicated above the bars.

4.4.6 Structural investigations

So far we experimentally observed a stiffening of the FEBID resonators during e-beam PGT which gives ideal possibilities to tune the resonators towards desired properties. However, from a fundamental point of view it is interesting to investigate these mechanisms in more detail. In the following we start with a brief introduction about the nanogranular system and describe then by a multi-technique approach how mechanical parameters can be extracted leading to a model about the processes during e-beam PGT.

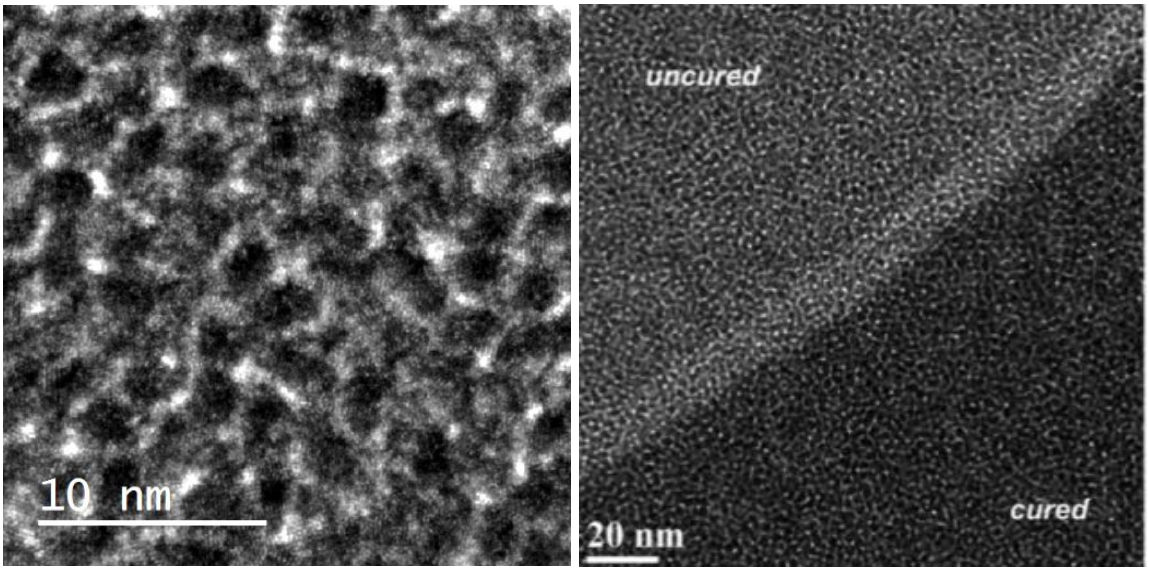

Figure 4-52: TEM bright field image of a typical Pt-deposit revealing the Pt nanograins (dark) embedded in a carbon (bright) matrix (left). The right image shows a TEM bright field image of a thin Pt-deposit layer which was partly cured with the electron beam, revealing slightly increased Pt grains which gives the darker contrast.

4.4.6.1 The nanogranular metal-matrix structure

To observe the intrinsic parameters of the material in more detail a closer look at the materials composition has to be taken: from previous studies at the FELMI it is known that the pillars consist of Pt grains which are embedded in a hydro-carbonaceous matrix resulting from either incompletely

dissociated and / or polymerized precursor fragments [4,6,7,10,11]. The Pt content of the FEBID structures was determined with EDX and STEM EELS and lies typically between 10 at.% and 20at.% in general and between 13 at.% and 17 at.% for 5 keV low current deposits. The Pt nanoparticles have a typical size of 2 - 3nm and are separated from each other by less than a nanometer. A TEM bright field image of a typical Pt deposit is shown in Figure 4-52 (left). It is also known from previous work that post-growth e-beam curing leads to a slightly increase in the grain size (just a few atom layers). This can be seen in Figure 4-52 (right) were a TEM image of a thin Pt-deposit layer is shown which was partly pre-cured with electrons. One can see that the cured area seems to be darker due to the increased grain sizes while agglomeration does not occur. This situation is very pronounced for low current deposits which are known to incorporate many incompoletely dissociated precursor molecules. This regime is called reaction rate limited where a lack of dissociating electron leads to the described effect. During post-growth e-beam curing these fragments are entirely dissociated releasing a small amount of Pt atoms which attach on already available Pt grains, explaining the slight grain growth. If e-beam exposure is performed for a longer time and most of the incorporated fragments are dissociated, the high electron flux is known to lead to a graphitization of the C-H matrix in between the Pt-grains [4,6,7,10,11]. Another important detail is the fact that the Pt grains are not physically contacting each other, neither after deposition nor after full curing. Hence, it is obvious that the overall Young's modulus has to be a combination of both: Pt as well as C. The density and Young's moduli of the materials from witch the FEBID deposits are composed of are summarized in Table 4-5. As it can be seen, if the carbon matrix dominates a Young's modulus ***E*** around 8 – 15 GPa should be found. On the other hand, if Pt dominates, a value of about 168 GPa is expected. In the following we try to extract the real value from a combined approach between simulations and static deflection experiments.

Table 4-5: Density and Young's moduli of the materials

	Pt	Camorph	Cgraphite	
rho	21.45	1.8–2.1	2.267	**g/cm³**
E	168		8-15	**GPa**

4.4.6.2 Parameter extraction from simulation

As explained in chapter 3.4 in detail, ***E*** can also be determined by performing electrostatic deflection experiments in combination with deflection simulations. In an experiment pillars were deposited in front of a deflecting electrode and deflection and resonance experiments were performed consecutively. Single resonance pillars with slightly elliptical shape were used on purpose (see chapter 4.4.1.2) since here the direction of the electrostatic deflection and also the resonance direction are equal.

Overall determination of Young's modulus via COMSOL simulations

At first the Young's modulus ***E*** for three different pillars deposited at 5 keV / 5 pA was investigated via simulation without any post-growth e-beam curing. All geometrical input parameters necessary for computation are listed in Table 4-6.

Table 4-6: Geometrical parameters for the simulation and calculated Young's modulus for three pillars (Y1 – Y3) in uncured state.

	Y1	Y2	Y3	
Elec Width	2756	2254	2254	**nm**
Elec Length	10000	10000	10000	**nm**
Elec Height	3000	3000	3000	**nm**
Side Radius	8000	8000	8000	**nm**
Square Size	10000	10000	10000	**nm**
Gap Size	1000	1000	1000	**nm**
Hole_depth	846	596	564	**nm**
D Pillar Vdd	2950	2930	2500	**nm**
D Pillar Ground	7050	7070	7500	**nm**
D Hole Vdd	2000	871	871	**nm**
D Hole GND	6000	6000	6000	**nm**
Pillar Height	7,43	7,87	7,75	**µm**
Pillar Width (Radius)	69 (34,5)	74 (37)	72,6 (36,3)	**nm**

Special emphasis was put on determination of pillar widths, since derivations of this value can affect the calculated Young's modulus ***E***. That's why 20 measurements were taken along the length-axis of every pillar and then the mean value was calculated. To finally calculate the Young's modulus the maximum deflections for different electrode voltages were measured for every pillar (see chapter 3.3.3.1) which were then used as input values for the COMSOL simulation (see chapter 3.4). Both voltages and final distances are listed in Table 4-7 together with COMSOL based E modulus values.

Table 4-7: Input parameters (voltage U and distance d) for COMSOL simulation together with calculated Young's modulus values for pillars Y1 - Y3 in uncured state.

Y1			Y2			Y3		
U (V)	**d (nm)**	**E (GPa)**	**U (V)**	**d (nm)**	**E (GPa)**	**U (V)**	**d (nm)**	**E (GPa)**
10	759	11,63	6	277	8,16	7	319	11,39
			8	441	10,13	9	572	12,11
			9	560	9,285	11	890	11,76
			10	688	9,99	12,5	1520	10,71
			11	883	9,01			
			12	1080	9,736			
			12,5	1140	9,72			
			13	1340	9,7845			
			13,5	1500	9,733			

As can be see the Young's modulus ***E*** seem NOT to be a function of the maximum deflection and thus independent on the investigated range of curvature. The variations for E that can be found for the three pillars when using different deflection voltages come from inaccuracies in the measurement of

the corresponding deflection. To improve the quality of the results the mean value of the calculated Young's moduli E for the different pillars were determined:

Y1	Y2	Y3
11.63±3 GPa	9.5±3 GPa	11.49± 3GPa

The relatively large variance was calculated by error estimations which were done by varying simulation input parameters (also the geometrical ones) by the amount of the maximum measurement error and redoing the simulation again. The highest impacts have inaccuracies in the pillar width and in the distance between pillar and electrode. By that two major conclusion can be drawn: 1) for the investigated bending range of 1200 nm (top), the Young's modulus ***E*** does not change suggesting no dynamic influences from the internal structure; 2) the found value is the range of carbon (see Table 4-5) suggesting that carbon modulus as determining parts. The latter is also in agreement with the typical internal structure of Pt based deposits as discussed in chapter 4.4.6.1.

Calculation of the overall density via COMSOL simulations

After determining the Young's modulus the total density of the FEBID material can be calculated by rearranging the equation for the resonance frequency:

$$\rho_{tot} = \frac{E_{sim}}{\left(7{,}147 * \frac{h^2}{w} * f_{res}\right)^2} \qquad (4.11)$$

where $\boldsymbol{\rho}$ is the density, $\boldsymbol{E_{sim}}$ is the Young's modulus determined by the simulation, $\boldsymbol{f_{res}}$ is the resonance frequency, ***h*** is the height and ***w*** is the width of the pillar.

This reveals overall density values $\boldsymbol{\rho_{cal}}$ of 4.73 g/cm^3 – 5.3 g/cm^3 as listed in Table 4-8. To cross check the found values, SEM based EDX spectroscopy was done revealing a Pt content of 17±3 at.%. Taking the density values of Pt and amorphous carbon (including its variation) into account (see Table 4-5) a density range of 4.55 g/cm^3 – 5.9 g/cm^3 follows (see equation (4.12)) which is in excellent agreement with the calculated values. Therefore, it can be concluded that the underlying theory, the experimental setup as well as the COMSOL simulations are suitable to describe the mechanical properties of the quasi-1D single pillars. In the following we double cross check the situation starting from the EDX based density values.

Table 4-8: Determined resonance frequency f_{res} and calculated matrix density ρ_{cal} for the pillars Y1-Y3 compared to the densities of Pt-FEBID deposits containing 15 at% Pt determined by EDX ($\rho_{EDX,15at.\%.Pt}$)

	Y1	Y2	Y3
$\mathbf{f_{res}}$	260 kHz	237 kHz	242kHz
$\mathbf{\rho_{cal}}$	5.26 g/cm³	4.73 g/cm³	5.3 g/cm³
$\mathbf{\rho_{EDX.15at.\%Pt}}$	4.55 g/cm³ – 5.9 g/cm³		

4.4.6.3 Verifying E and ρ through material concentrations

Since the total density of the FEBID deposit is given by the densities of the individual components of the deposit it can be calculated by

$$\rho_{tot} = C_{Pt}\rho_{pt} + C_M\rho_M \tag{4.12}$$

where C_{Pt} and C_M are the concentrations of Platinum and the matrix material and ρ_{Pt} and ρ_M are the densities. Inserting the values for ρ which are given in Table 4-6 and a Pt-content of 17 at.% and by taking into account the maximum variations gives the average result of 5.11 ± 0.6 g/cm³ for the total density. When the resonance frequencies of the pillars are known E can be calculated by rearranging (2.7) into:

$$E = \rho_{tot}\left(7{,}147 * \frac{h^2}{w} * f_{res}\right)^2 \tag{4.13}$$

where ρ_{tot} is the total density of the, f_{res} is the resonance frequency, h is the height and w is the width of the pillar. Applying this expression with the above mentioned EDX based densities reveals vice-versa elastic moduli for pillars Y1-Y3 listed in Table 4-9 for uncured states.

Table 4-9: Determined resonance frequency f_{res} and calculated Young's modulus E determined by the material concentrations method compared to the Young's modulus determined by the simulation through COMSOL

	Y1	Y2	Y3
fres	260 kHz	237 kHz	242kHz
E	10.86±1.4 GPa	9.95±1.3 GPa	10.13±1.3 GPa
E_{COMSOL}	11.63±3 GPa	9.5±3 GPa	11.49± 3GPa

As can be seen also this alternative approach gives excellent agreement again proofing the applicability of the entire approach for accessing the mechanical parameters of quasi-1D single pillars. In the following we expand our calculations to post-growth e-beam cured pillars to access variations which finally allow to derive a structural model explaining the frequency shifts.

Effect of pre-curing on the Young's modulus

Experiments revealed that for cured pillars higher electrode voltages and thus a higher force acting on the pillar is needed to achieve the same amount of deflection. According to equation (3.2) this suggest that the e-beam treatment leads to an increase of the stiffness and thus also the Young's modulus. This change of the Young's modulus is also responsible for the shift of the resonance frequency explained in 4.4.4.3. To investigate this assumption in more detail, the dependence of the Young's modulus on the irradiation time was investigated by measuring the deflection after finite

curing intervals and subsequently calculating the corresponding value of ***E*** via COMSOL. Since also the resonance frequency f_{res} is influenced by the curing process, it was also measured simultaneously. For all measurements the "curing from the top"-method was used with same treatment settings as those described in chapter 4.4.4.3. In Figure 4-53 the Young's modulus of pillar Y1 is plotted in dependency on curing time (left) and corresponding fundamental resonance frequency (right). As can be seen, the time dependent Young's modulus increase as the resonance does, shown in Figure 4-40 in Chapter 4.4.4.3. The dependency on the resonance frequency (right graph) proves further the direct correlation via linear dependency. In the experiment the pillar was cured for 50 minutes which corresponds to a frequency shift of about the double of the start frequency. Like shown in Figure 4-42 in chapter 4.4.4.3 the maximal frequency for fully cured pillars roughly corresponds to the triple of the frequency of the uncured pillars. With this knowledge the Young's modulus for pillar Y1 in fully cured state (E_{fc}) can be estimated from the linear fit in Figure 4-53 (right) with a value of 85GPa which is also indicated in the figure. These estimations reveal an increase of E by a factor of three and more which proves a direct link to the resonance frequency.

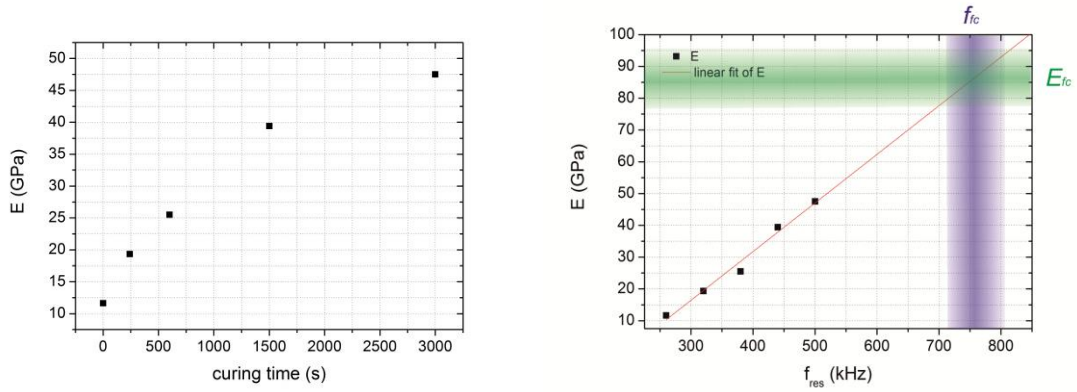

Figure 4-53: Young's modulus in dependence of the irradiation time (left) and in dependence of the resonance frequency (right)

4.4.6.4 Introduction of the PS factor

Like already described above the PtC structures contain about 17 at.% Pt. The matrix consists of a widely amorphous C-H matrix. If these components were distributed totally homogenous the Young's modulus could be calculated by:

$$E_{hom} = c_{Pt} * E_{Pt} + c_c * E_c \qquad (4.14)$$

with E_{hom} the Young's modulus of the homogenous material and c_i and E_i the concentrations and Young's moduli of the components. By using the values E_{Pt} = 168 GPa and E_C = 8 GPa from Table 4-5 E_{hom} can be estimated with a value of 32 GPa in contrast to COMSOL calculated values of about 9.95 GPa – 10.68 GPa summarized in Table 4-9. To illustrate this deviation more clear, the theoretical deflection of pillar Y2 is calculated assuming a homogenous composition with E_{hom}. Figure 4-54 shows the according result by the blue triangles. As comparison, the real deflection values are shown by the black squares, which clearly show that the pillar is easier to deflect than a homogeneously calculated material.

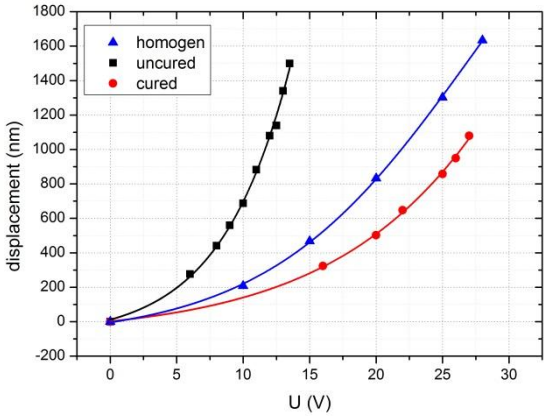

Figure 4-54: Theoretical deflection of a homogenous pillar (blue) and measured deflections of the cured (red) and uncured pillar (black) in dependence of the deflecting electrode voltage

To account for this deviation, the nano-granular structure of the FEBID material has to be taken into account. The Pt nanograins, embedded in the C-H matrix, are separated from each other by just a few Å as discussed in chapter 4.4.6.1. A simplified scheme is shown in Figure 4-56 (left) and reveals that the carbon matrix is mainly determining the mechanical properties. This is in agreement with the COMSOL calculated ***E*** values of 9.95 GPa – 10.68 GPa which are very close to those for carbon (8 – 15 GPa) and far away from $\boldsymbol{E_{HOM}}$ values of ~32 GPa calculated for homogeneous materials.

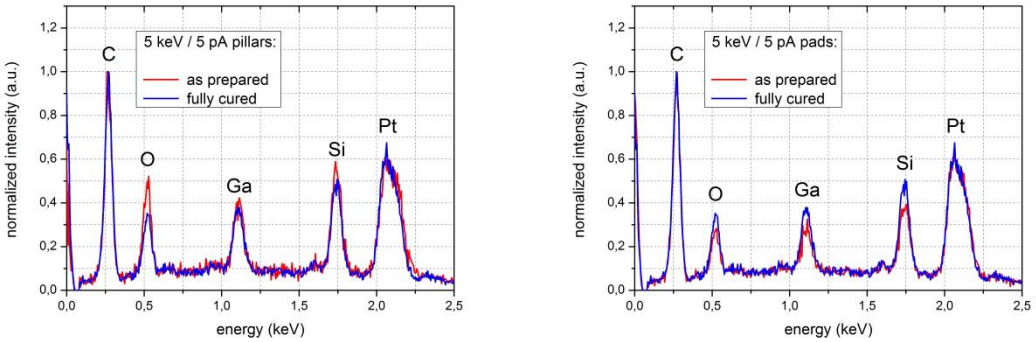

Figure 4-55: EDX analysis of quasi-1D single pillars (left) and quasi-2D pads (right) as-preparation (red) and after full e-beam curing (blue) normalized to the carbon peak. It can be seen that relative Pt / C peak ratios stay the same. Quantitative analyses suggest a Pt content of 17±3 at.%.

For pillars treated by post-growth e-beam curing, the situation change. As explained in chapter 4.4.6.1, the used curing process slightly increases the Pt grains. Before a reliable statement can be given, a closer look on the pillar diameter and its inner structure has to be given. Comparison between as-prepared and fully cured pillars revealed small variations of ±3 nm after e-beam PGT, even for very long exposure times of 3000 sec. As a second step, TEM has been performed before and after curing as summarized in Figure 4-57. A direct comparison of an edge area (a, b) shows a thin carbon layer of about 3 nm which does not change during curing (compare a with b). By that, a densification of the Pt grains can be excluded as explanation for the increasing Youngs modulus during curing. Furthermore, as important information, graphitic structures have been found (c) for fully cured structures but never for pristine pillars. The graphite identification has been verified via

data bases and indicate the material variation during long time exposure as already observed by previous studies [6,7].

As a first step for long time cured pillars, static deflection experiments has been performed as shown in Figure 4-54 by the red circles. As it can be seen, the deflection is less than estimated for a homogeny material, indicating stiffer properties of the pillar as expected. COMSOL simulations yield an overall modulus E of 9.5 – 11.63 (±3) GPa. The correlated EDX spectra on the other hand are shown in Figure 4-55 and suggest a constant chemical composition which is in agreement with TEM observations. The found value, however, is much higher than pure carbon would suggest even for fully graphitized properties. Hence, an internal effect has to be responsible for this change which can be found in the nanogranular structure. Taking the above described effects of grain growth at constant outer pillars diameters into account, it is possible to derive a structural model as schematically shown in Figure 4-56 on the right. The slightly increasing Pt nanograins lead to stronger contact between adjacent Pt grains. Hence, the stiffness increases although pure Pt conditions are not reached: $\boldsymbol{E_{fully\ cured}}$ = 85±10 GPa compared to $\boldsymbol{E_{Pt}}$ = 168 GPa.

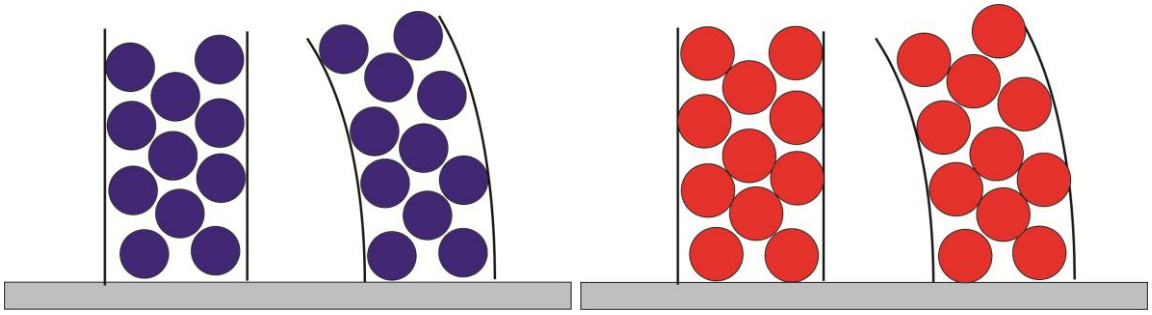

Figure 4-56: Influence of the particle size on the stiffness of the material.

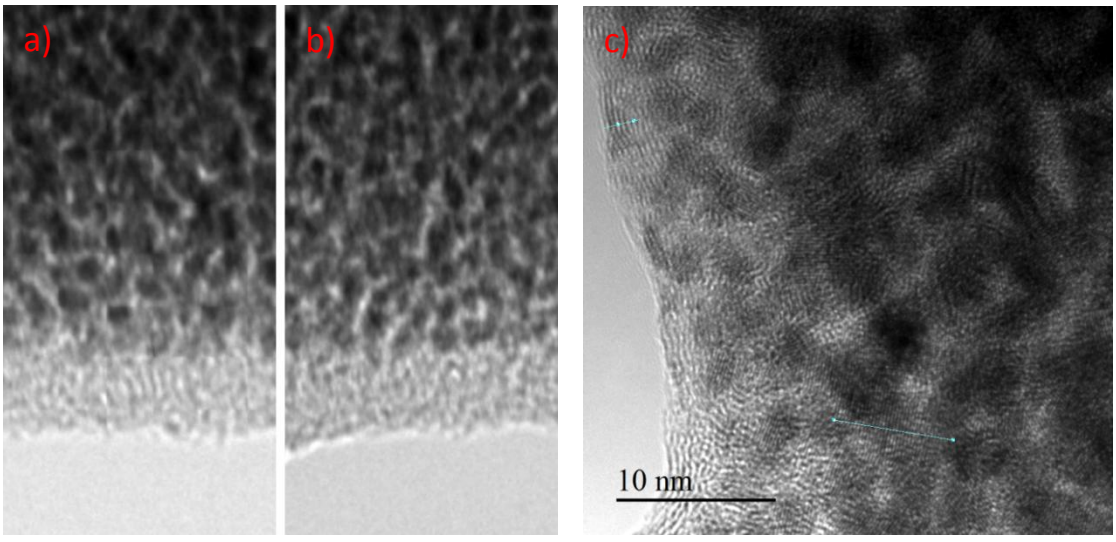

Figure 4-57: TEM bright field images of a pillar side wall before curing (a) and after long time curing for 50 min (b) revealing no changes of the thin outer carbon layer (bright material). (c) shows a high resolution image of a fully cured single pillar revealing graphitic crystal structure.

Considering equation (2.7) together with the above explanations it is obvious that his relation does not hold as it assumes a homogeneous material. Therefore, an additional factor is introduced which takes the nanogranular properties into account. The above mentioned expression is suggested to be rewritten as:

$$f_{cylinder} = 0{,}1399 \sqrt{\frac{E_{hom} * \boldsymbol{p_S}}{\rho}} \frac{w}{h^2} \qquad (4.15)$$

The new factor $\boldsymbol{p_s}$ (pillar structure – or Plank-Stermitz) takes account for the structural changes during e-beam post-growth curing and becomes <1 for uncured structures and >1 for long time cured structures. In detail, values of 2.75 and 0.67 are found for pristine and long-time cured values which were determined for pillar Y1. The $\boldsymbol{p_s}$-factor in dependence of the curing time and the resonance frequency for pillar Y1 is shown in Figure 4-58. The ps-factor shows a linear dependency on the resonance frequency. Like described in 4.4.6.3 for the Young's modulus also the ps-factor for fully cured pillars was estimated with a value of 2.7.

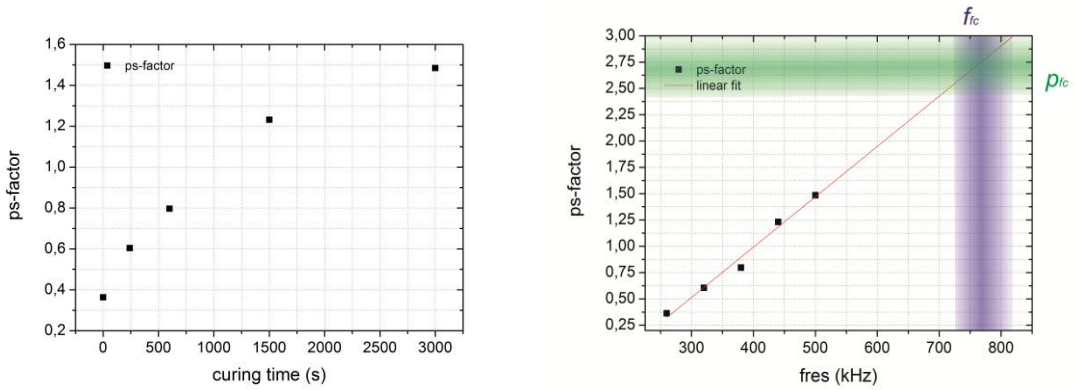

Figure 4-58: p_s-factor in dependence of the curing time (left) and in dependence of the resonance frequency (right) determined for pillar Y1.

4.4.6.5 Summary structural investigations

Considering all data it can be concluded that post-growth e-beam curing leads to a slight grain growth at constant outer diameter and total chemistry. The nanogranular structure leads to a stiffening of the pillar starting from pure carbon mechanics towards a combined value where partial percolation takes place. This leads to a frequency change and explains the situation from a structural point of view. Mathematically, the situation can be described by the introduction of an additional structure factor $\boldsymbol{p_s}$ which takes the nanogranular structure into account.

Besides that, we could successfully extract several parameters, namely the overall density of the pillars with 4.73-5.3 g/cm³ and also the matrix density with 1.8-2.1 g/cm³, the Young's modulus for the uncured with 9.95- 10.68GPa and the Young's modulus of the fully cured pillars with 85±10GPa. Furthermore we introduced a $\boldsymbol{p_s}$ factor which takes account for the structural changes during e-beam

post-growth curing which was determined with a value of 2.75 for uncured pillars and 0.67 for long time cured pillars. After understanding the fundamental processes which causes and changes the resonance frequencies including tuning possibilities, we have to answer the question whether the proposed sensing effect can be achieved which will be discussed in the following chapter.

4.5 Electrical Readout

One vision of this thesis is the development of a gas sensor like described in chapter 2.5. To prove the gas-sensing concept it is necessary to find a way to measure the resonance frequency outside the DBM vacuum chamber under different gas atmospheres. One way to do this is the electrical read out which uses the resonance feedback of the pillar with respect to the exciting signal. Accordingly electrical read out experiments were done in collaboration with NTC Weiz by Dr. Stefan Sax, DI Sebastian Nau and Prof. Dr. Emil J. W. List Kratochvil. The measurements were performed inside an N_2 glove box via electrical nanoprobes and LCR meters as described below. Since entire experiments were performed outside of the SEM, type A and AR test structures were used (see chapter 4.2.3) which are connected via gold lines to the large contact pads, enabling the contact with the microprobe needles. The FEBID resonators were placed between the electrodes of the test structures as shown in Figure 4-59.

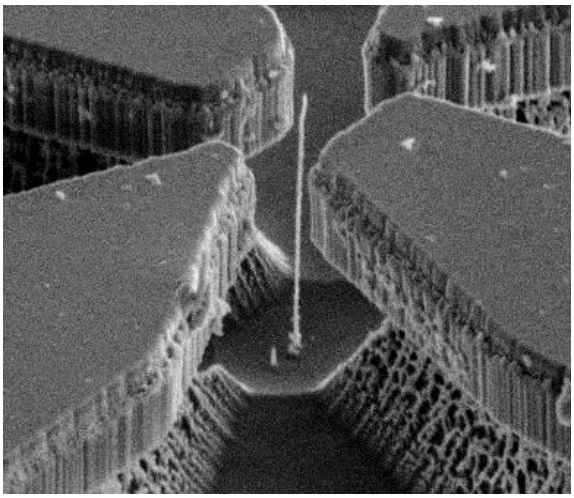

Figure 4-59: quasi-1D FEBID single pillars placed between type A electrodes on the test structures.

4.5.1 Sensing concept

The electrical behavior of the Pt-FEBID resonators investigated in this work is comparable to the electrical behavior of crystal oscillators, where a piezoelectric crystal (instead of the Pt-C pillar) is brought into resonance via an electric AC field. The Pt-FEBID resonator can be described by the same equivalent circuit than the crystal oscillator which is shown in Figure 4-61 (left). It is buildup of a resonant series circuit which consists of a dynamic inductivity L_1, capacity C_1 and of a motional resistance R_1. Thereby, L_1 corresponds to the oscillating mass of the resonator, C_1 corresponds to the Young's modulus and R_1 corresponds to the dynamic friction and other losses in the resonator. The capacity C_0, which is connected in parallel, describes the capacity of the electrode structure itself. The resonance frequency of such a circuit can be found by determining the impedance in

dependence of the excitation frequency. Therefore, the effective voltage U_{eff} and the effective current I_{eff} in combination with the phase φ between them has to be measured. Then the impedance can be determined by the equation

$$Z = \frac{U_{eff}}{I_{eff}} e^{i\varphi} \tag{4.16}$$

The imaginary part of the impedance is called reactance and can be determined by

$$Im(Z) = |Z| \sin(\varphi) \tag{4.17}$$

In our experiments the determination of the impedance curves was done with an Agilent E4980A precision LCR meter (see Figure 4-60) which measures the impedance and phase automatically for several frequencies like explained above.

Figure 4-60: Agilent E4980A Precision LCR meter

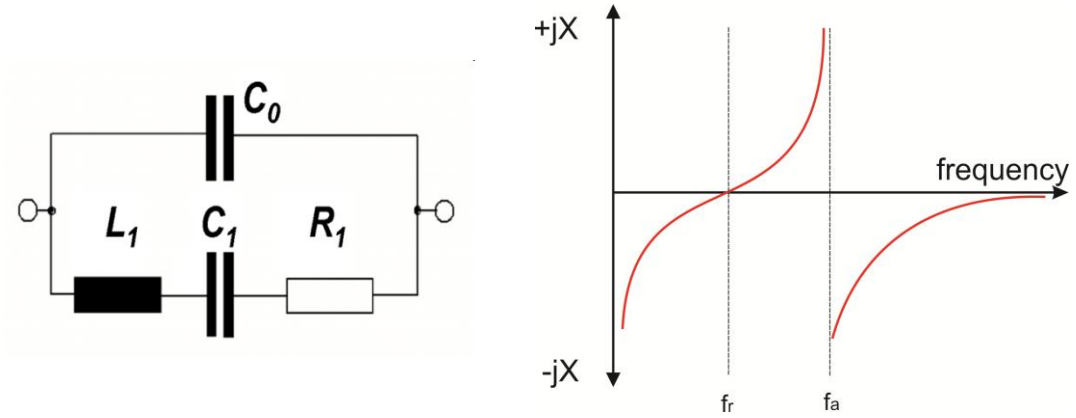

Figure 4-61: Equivalent circuit diagram of the FEBID resonator circuit (left) and typical reactance in dependence of the frequency for such a circuit (right)

The theoretical *reactance* of the equivalent circuit in dependence of the frequency is shown in Figure 4-61 (right). The frequency (abscise) is plotted logarithmically. The circuit shows resonance behavior at two frequencies, the resonance frequency f_r and the anti-resonance frequency f_a. At these frequencies the phase between current and voltage become zero which also leads to a zero crossing point in the reactance curve. Up to the frequency f_r and above the anti-resonance frequency f_a the circuit shows capacitive behavior, between the two frequencies it becomes inductive. Due to the parallel capacity C_0 the resonance frequency f_r of the overall system is not exactly equal to the serial resonance frequency of the dynamic components which describes the FEBID oscillator itself.

4.5.2 Preliminary results

Like already described in 4.5.1 the impedance and phase curves were determined with the LCR-meter. For every curve 200 measurements were performed by sweeping the excitation frequency between 1 kHz and 2 MHz in logarithmic steps and measuring the corresponding impedance and phase values. From this curves the corresponding reactance curves were calculated by equation (4.17). In a first experiment the impedance and phase curves for an empty test structure (structure without FEBID resonator) was determined. The output voltage of the LCR meter was set to 0.5 V_{RMS}. The results are shown in Figure 4-62. Like expected the structure showed pure capacitive behavior since the phase never become positive.

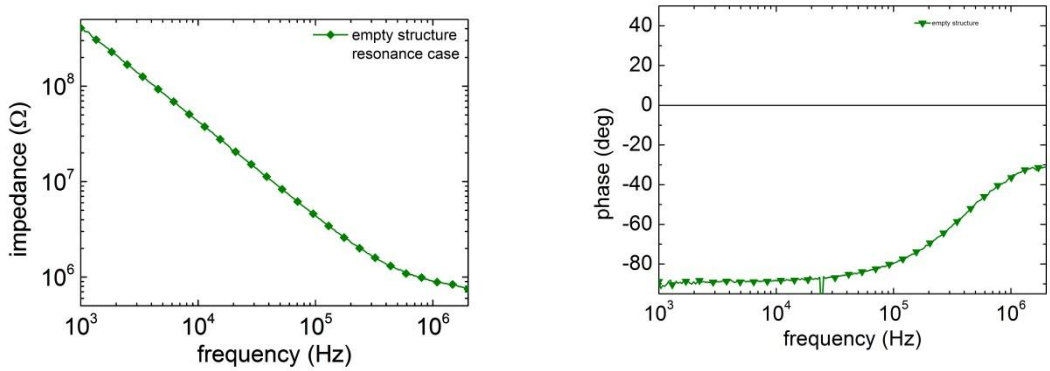

Figure 4-62: Impedance (left) and phase curve (right) in dependency of the frequency for empty test structures.

In all measurements described in the following PtC-pillar structures were used as resonators which were deposited in a distance of 3 µm from the exciting electrodes. It was observed that most of the pillars don't show resonant behavior right at the beginning. The resonators need a kind of pre-treatment procedure in order to work properly. It was found that this can be achieved by performing several frequency sweeps (from 1kHz to 2MHz) or / and by applying a DC voltage (we used 4V) between electrode and pillar for some seconds before performing the measurement. It is assumed that this activation is needed to establish a conductive path within the pillars. This activation was not necessary inside the electron microscope since this activation was done by the injected high energy primary electrons of the electron beam. The impedance and phase curves before and after activation measured in the Ar glove box is shown in Figure 4-63 for an LCR meter output voltage of 0.5 V_{RMS}. The black curve shows the first measurement of a non-activated pillar and resembles the open path behavior in Figure 4-62. After performing 23 frequency sweeps, the pillar suddenly goes into the activated state and shows then a stable behavior as shown by the red curve. Furthermore, it also was observed that the resonance curves seem to shift up a bit after performing several measurement cycles. This is shown in Figure 4-64 by directly overlaid resonance curves. It is assumed that long time operation changes a bit the internal structure similar to the activation process which proved slight changes in the internal pillar situation. It also has to be kept in mind that the pillars were exposed to ambient conditions during FELMI – NTCW transfer, followed by a vacuum step during the glove box transfer and finally the pillars were brought into Ar conditions. Hence, several processes can ultimately contribute to the finally observed observations of varying resonance frequencies. The

circumstances of these variations will be investigated in a follow-up thesis at the FELMI in 2014 and comprise a complete measurement setup at the DBM in order to exclude atmospheric effects.

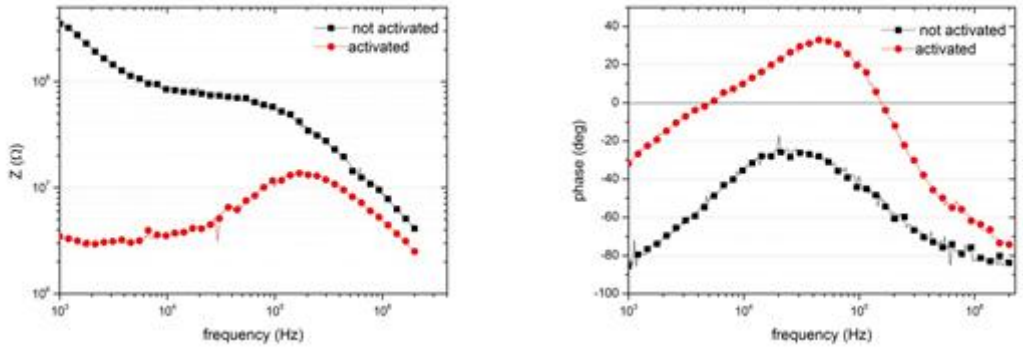

Figure 4-63: Impedance curve (left) and phase curve (right) of non-activated (black squares) resonator and activated (red circles) resonators in dependence on the frequency.

Nevertheless, first experiments reveal clearly that the resonators, though extremely small, can be read out electrically which is the key for further development of this sensor concept towards gas sensing applications.

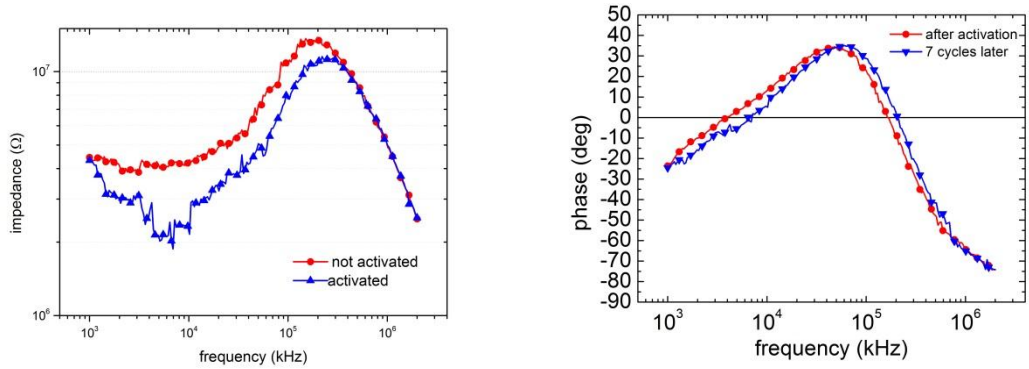

Figure 4-64: Impedance curve (left) and phase curve (right) of a pillar directly after the activation and 7 measurement cycles later

5 Conclusions and Outlook

In this thesis focused electron beam induced deposition (FEBID) has been used to fabricate freestanding quasi-1D nanopillars with diameters down to 50 nm and lengths up to 15 µm. The pillars have then been excited via electrical AC fields which cause resonance oscillations at their mechanical resonance frequencies. Systematic post-growth treatments via the electron beam allowed the tuning to higher resonance frequencies by a factor > 3 starting in the range of 50 kHz – 100 kHz. Closer investigations revealed the internal nanogranular structure of Pt grains embedded in a hydrocarbon matrix to be responsible for the frequency variation due to slightly growing Pt grains which ultimately changes the Young's modulus of the pillars while diameters and chemical composition stays the same. By that a comprehensive insight could be achieved to understand its dynamic behavior as well as their tunability with respect to resonance behavior and mechanical properties which represents the first step for further developments towards sensing applications.

In more detail, the study started with detailed investigations concerning growth behavior and the achievement of radially symmetrical pillars at lowest beam currents possible. As a second path, appropriate test structures have been developed which allow electric field experiments to deflect and excite the freestanding FEBID deposits. Finally, complex test structures have been introduced which allow application of electric fields in different geometries including active sample stage arrangements in the DBM (see Figure 5-1a). First electrostatic deflection experiments revealed the expected behavior which was complemented by finite element simulation via COMSOL in very good agreement. Dynamic experiments confirmed then the concept of electrodynamic pillar excitation and acted as proof-of-concept. However, instead of one amplitude two different deflection orientations in resonance have been found for most pillars. Closer examination revealed that slightest radial asymmetries in the pillar diameters are responsible for this behavior. In order to suppress this double deflection a procedure has been developed which use an on-purpose astigmatism which successfully lead to a highly oriented single deflection towards the excitation electrodes (see Figure 5-1b). Such optimized pillars were then used for the successful characterization of scaling laws with respect to pillar dimensions as well as their internal composition due to slightly different mechanical properties. Additionally, experiments with very thin, freestanding pads have been performed, also revealing excellent agreement with the underlying theory and simulation results via COMSOL. The comparison with complementary theory revealed excellent behavior and prove that such pillars and pads can be considered as quasi-1D and quasi-2D resonators in an electric AC field.

In a second step pillars and pads have been subjected to post-growth treatment via the electron beam. It has been found that the FEBID structures gradually increase their resonance frequencies by a factor larger than 3. Systematic investigations revealed that the pillars do neither significantly change their dimensions nor their chemical overall composition. Further investigations via transmission electron microscopy confirmed also that the internal material distribution does not change. From previous studies at the FELMI it is known that e-beam post-growth treatment lead to slight growth of the Pt particles while the overall distribution remains identical. With this knowledge additional static and dynamic experiments have been performed and complemented by theory and COMSOL simulations. By that a comprehensive model could be derived explaining the resonance tunability from a fundamental point of view. After preparation the individual Pt grains are barely in physical contact to each other but separated by the carbon matrix in between stemming from incompletely dissociated precursor molecules and detached hydrocarbon fragments (see Figure 5-1c). A combined approach of simulations, theory and experiments allowed estimating the Young's

modulus in the range of 9.5 GPa – 11.7 GPa which is in the range of classical carbon. This means that the mechanical properties are mainly determined by the carbon matrix for the investigated deflection radii. After e-beam post-growth treatment the Pt grains are getting closer together and partly start to touch each other. The combined approach for fully cured pillars revealed a Young's modulus increase by a factor of more than 5 which definitely exceeds the value for carbon but clearly stays below the module for Pt which is 168 GPa. This allows the conclusion that the pillar gets increasingly dominated by the Pt grains which explains both the higher resonance frequency due to the stiffer character and the sharper resonance curve due to reduced internal damping. Beside the detailed insight in structural peculiarities during post-growth treatments and the mechanical consequences, these findings provide a perfect tool to tune the resonators towards frequency and resonance sensitivity which is essential for further applications. Based on these results it was clear to get a step further and test such resonating pillars on their ex-situ applicability as they need to work outside the DBM. Therefore, electrical experiments have been performed which successfully revealed the expected behavior of a resonance circuit even for such small resonator dimensions. By that it is demonstrated that the developed concept of freestanding, quasi-1D resonators can be used for electrical applications in an easy and straightforward manner.

In subsequent studies it is planned to implement the full electrical resonance characterization at the DBM which excludes atmospheric effects in a first step followed by the systematic exposure to different conditions such as pressure, temperature and finally specific gas environments. In order to tune both, resonance frequencies and sharpness of resonance curves further towards its intrinsic limits purification experiments will be conducted at the FELMI. Also fully FEBID based resonator electrode geometries have already been demonstrated in pre-experiments (see Figure 5-1d) which demonstrates the enormous potential of this technique for the direct-write fabrication on almost any surface.

All together it can be stated that FEBID provides an excellent tool for the fabrication of freestanding nanostructures in a straightforward manner. The key property, however, lies in the nanogranular metal-matrix structure of the material which, in case of the resonators, provides internal damping which can gradually be adapted by post-growth treatment procedures. And it again demonstrates - although unwanted for some applications - the high carbon content in FEBID deposits can be used for novel application concepts and their tunability.

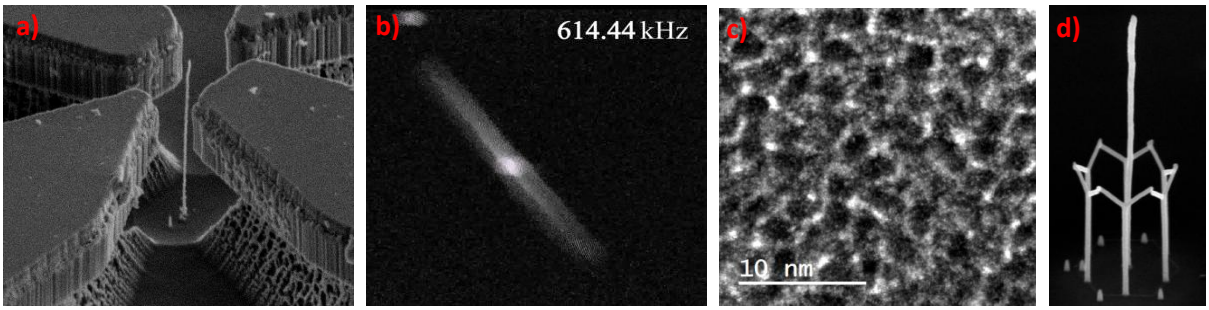

Figure 5-1: (a) quasi-1D Pt-C resonator (Ø ~ 60 nm) in between excitation electrodes; (b) electrically excited Pt-C resonator at its mechanical resonance frequency; (c) active electrode pillar structure in resonance, b) pillar resonator between test electrodes, c) nano-granular metal-matrix structure of a Pt-C FEBID deposit; (d) demonstration of fully FEBID processed resonator – electrode geometry.

References

[1] Utke, I.; Russell, P. E. *Nanofabrication using focused ion and electron beams: principles and applications* Oxford University Press New York, 2012

[2] Courtesy of Harald Plank, Steyrergasse 17, 8010 Graz, Austria: Institute for Electron Microscopy (FELMI-ZfE), Graz University of Technology, www.felmi-zfe.at

[3] Botman, A.; Mulders, J. J. L.; Hagen, C. W. *Nanotechnology* 2009, **20** (1), 372001.

[4] Plank, H.; Haber, T.; Gspan, C.; Kothleitner, G.; Hofer, F. *Nanotechnology* 2013, **24**, 1753605.

[5] Plank, H.; Noh, J. H.; Fowlkes, J. D.; Lewis, B.; Rack, P. D. *ACS Appl. Mater. Interfaces* 2014, **6** (2), 1018.

[6] Huth, M.; Porrati, F.; Schwalb, C.; Winhold, M.; Sachser, R.; Dukic, M.; Adams, J.; Fantner, G. *Beilstein. J. Nanotechn.* 2012, **3**, 597.

[7] Plank, H.; Michelitsch, S. G.; Gspan, C.; Hohenau, A.; Krenn, J.; Kothleitner, G.; Hofer, F. *J. Vac. Sci. Technol. B* 2011, **29** (5), 051801.

[8] Friedli, V.; Utke, I. *J. Phys. D: Appl. Phys.* 2009, **42**, 125305.

[9] Winkler, R.; Fowlkes, J.D.; Szkudlarek, A.; Utke, I.; Rack, P.D.; Plank, H. *ACS Appl. Mat. and Interfaces*, 2014, in print

[10] Plank, H.; Gspan, C.; Dienstleder, M.; Kothleitner, G.; Hofer, F. *Nanotechnology* 2008, **19**, 485302.

[11] Plank, H.; Smith, D. A.; Haber, T.; Rack, P. D.; Hofer, F. *ACS Nano* 2012, **6**, 286.

[12] Private communication with Ivo Utke, EMPA, Thun, 2013

[13] ***i)*** Goldstein, J.; Newbury, D.; Joy D.C. et al. *"Scanning electron microscopy and X-ray microanalysis"*. 3rd Edition ed. New York: Springer Scienes+Business Media, Inc.; 2003. and ***ii)*** Reimer, L. *Scanning electron microscopy: Physics of image formation and microanalysis*. Vol 45. 2 completely rev. update, ed. Berlin ; New York: Springer; 1998:527

[14]Mayer, J.; Giannuzzi, L.A.; Kamino, T.; Michael, J. *MRS Bull*, 2007, **32**, 400.

[15]Orloff, J.; Utlaut, M.; Swanson, L. *High Resolution Focused Ion Beams* Springer, New York, USA 2003

[16]Giannuzzi, L.A.; Stevie, F.A. *Introduction to focused ion beams: instrumentation, theory, techniques, and practice* Springer, New York, 2005.

[17] ***i)*** Michelitsch, S.G *Master Thesis*, 2010, FELMI (TU Graz); ***ii)*** Kolb, F. *Master Thesis*, 2013, FELMI (TU Graz)

[18] Hunt, F.V. *Electroacoutics: The Analysis of Transduction, and Its Historical Background* Cambridge, MA: Harvard Univ. Press, 1954